INTERNATIONAL DOCTORAL SCHOOL OF THE USC

David
Travieso Mayo

PhD Thesis

Studies in dynamical AdS/CFT with modified boundary conditions

Santiago de Compostela, 2025

Doctoral Programme in Nuclear and Particle Physics

ESCOLA DE DOUTORAMENTO
INTERNACIONAL DA USC

TESE DE DOUTORAMENTO

STUDIES IN DYNAMICAL ADS/CFT WITH MODIFIED BOUNDARY CONDITIONS

Autor

David Travieso Mayo

Director: Javier Mas Solé

Titor: Javier Mas Solé

PROGRAMA DE DOUTORAMENTO EN FÍSICA NUCLEAR E DE PARTÍCULAS

SANTIAGO DE COMPOSTELA

Contents

List of reproduced publications

[1] J. Mas[1] and D. Travieso Mayo,[1] *Resonant drivings in global AdS*, JHEP 11 (2023) 230 [arXiv:2307.16884].

[1] Departamento de Física de Partículas, Universidade de Santiago de Compostela and Instituto Galego de Física de Altas Enerxías (IGFAE), E-15782 Santiago de Compostela, Spain

Included at chapter 3.

PhD student contribution: Numerical simulations. Participation in analysis, discussions and writing.

Journal: Journal of High Energy Physics

Publisher: Springer

ISSN: 1029-8479

Year of publication: 2023

DOI: https://doi.org/10.1007/JHEP11(2023)230

Impact factor in 2023: 5 (JCR data)

Rank in Physics, Particles and Fields in 2023: 6/31 (JCR data)

[2] A. Serantes,[1] D. Travieso Mayo[2] and J. Mas,[2] *Multitrace deformations and the nonlinear stability of Anti-de Sitter space*, Phys. Rev. D 111 (2025) 024044 [arXiv:2411.03297].

[1] Department of Physics and Astronomy, Ghent University, 9000 Ghent, Belgium

[2] Departamento de Física de Partículas, Universidade de Santiago de Compostela and Instituto Galego de Física de Altas Enerxías (IGFAE), E-15782 Santiago de Compostela, Spain

Included at chapter 4.

PhD student contribution: Numerical simulations. Participation in analysis, discussions and writing.

Journal: Physical Review D

Publisher: American Physical Society (APS)

ISSN: 2470-0010 (print), 2470-0029 (online), 1538-4500 (CD-ROM)

Year of publication: 2025

DOI: https://doi.org/10.1103/PhysRevD.111.024044

Impact factor in 2023: 4.6 (JCR data)

Rank in Physics, Particles and Fields in 2023: 7/31 (JCR data)

Resumo en galego

Esta tese investiga a dinámica da gravidade de Einstein acoplada a un campo escalar nun espazotempo asintoticamente anti-de Sitter (AdS), centrando a atención nas implicacións de diferentes condicións de fronteira. O traballo baséase na correspondencia AdS/CFT e explora como a dinámica do campo escalar con condicións de fronteira dependentes do tempo e deformacións na fronteira da teoría de campos conforme dual afectan á estabilidade do espazo AdS.

Nas últimas décadas, a correspondencia anti-de Sitter/CFT (AdS/CFT), tamén chamada holografía, consolidouse como unha peza fundamental da física teórica, proporcionando unha profunda comprensión da interacción entre a gravidade e as teorías cuánticas de campos. Proposta por Juan Maldacena en 1997 [3], esta dualidade abriu novos camiños para explorar teorías de campos cuánticos fortemente acopladas e a dinámica non perturbativa na teoría de cordas. A correspondencia propón unha equivalencia entre unha teoría gravitacional nun espazo AdS en $d+1$ dimensións e unha teoría de campos conforme (CFT) definida na súa fronteira en d dimensións.

O traballo de P. Bizoń e A. Rostworowski sobre a inestabilidade de AdS en 2011 [4] destacou o comportamento único de AdS como sistema gravitacional. A diferenza dos espazotempos de Minkowski ou de Sitter, descubriuse que AdS é non linealmente inestable. Máis especificamente, atoparon que datos iniciais con forma gaussiana dun campo escalar sempre levan á formación dun burato negro, independentemente do pequena que sexa a súa amplitude ε. O tempo que transcorre desde o inicio ata que se produce o colapso escala coa amplitude como ε^{-2}, algo característico desta inestabilidade. O mecanismo que permite esta inestabilidade é unha cascada turbulenta de enerxía a través dos modos normais do sistema deica frecuencias máis altas, o cal eventualmente conduce ao colapso gravitacional. Esta cascada de enerxía desencadéase pola estrutura resoante de AdS. Nesta tese, referirémonos a este tipo de inestabilidade non lineal como a *inestabilidade de Bizoń-Rostworowski (BR)*.

Traballos posteriores demostraron que existen outros tipos de solucións, como oscilóns [5, 6], estrelas bosónicas [7, 8] ou xeometrías estáticas como os solitóns na teoría de Einstein-Maxwell cun escalar [9], que son non linealmente estables. Máis recentemente, o traballo en [10] ampliou as solucións oscilatorias a solucións periódicas no tempo, onde o campo escalar na fronteira é distinto de cero. Isto introduce outro ingrediente: as condicións de fronteira periódicas no tempo.

A maioría dos traballos no contexto da correspondencia AdS/CFT tratan xeometrías estáticas, que son duais a estados de sistemas fortemente acoplados en equilibrio. O feito de que a holografía se estenda a situacións dependentes do tempo é un tema que, sen dúbida, merece unha atención detida.

Parte desta tese está motivada pola busca dunha comprensión máis profunda do comportamento das mencionadas solucións periódicas no tempo preto das resonancias do sistema, non só cunha soa frecuencia, senón tamén coa complexa interacción entre múltiples frecuencias nun sistema completamente non lineal.

Outra parte desta tese segue unha motivación diferente. Os oscilóns, as estrelas bosónicas e os solitóns mencionados anteriormente rompen o espectro exactamente resoante de AdS, interrompendo a inestabilidade non lineal. Actúan como atractores, creando *illas de estabilidade non lineal* para datos iniciais. Nesta tese, seguimos un enfoque diferente para este problema. Aplicamos algunhas condicións de fronteira, duais a unha teoría de campos conforme deformada, onde a estrutura resoante de AdS está explicitamente rota desde o principio.

Traballaremos cun sistema AdS_4-Einstein-escalar no que o cadrado da masa do campo escalar está na chamada xanela de dobre cuantización. Despois impoñemos condicións de fronteira mixtas, tamén coñecidas na literatura como gravidade deseñada (*designer gravity*). Este enfoque pode considerarse como o análogo natural do problema no espazo plano discutido en Refs. [8, 11, 12], onde considerouse unha xeometría esfericamente simétrica cun campo escalar sen masa encerrado nunha caixa. Neste caso de espazo plano, a elección entre condicións de fronteira de Dirichlet ou Neumann para o campo escalar está nunha correspondencia un a un coa natureza resoante ou non resoante do espectro e coa presenza ou ausencia da inestabilidade BR.

No contexto da holografía, as condicións de fronteira da gravidade deseñada corresponden a deformacións multitraza da teoría de campos conforme que vive na fronteira [13, 14]. No pasado, as deformacións multitraza utilizáronse para deseñar potenciais efectivos ilimitados na teoría de campos que soportan cosmologías de *big crunch* no espazo interior [15, 16], *quench* cuánticos [17] ou transicións de fase [18–20]. Os nosos resultados sobre a estabilidade non lineal de AdS_4 con condicións de fronteira de gravidade deseñada poden considerarse como unha exploración do efecto das deformacións multitraza na termalización de estados espacialmente homoxéneos na teoría ABJM [21] situada nunha 2-esfera.

A estrutura desta tese é a seguinte. O capítulo 1 proporciona o marco teórico, introducindo as propiedades do espazotempo AdS e a correspondencia AdS/CFT, ademais de revisar as características da mencionada inestabilidade non lineal atopada por Bizoń e Rostworowski.

O espazotempo de anti-de Sitter (AdS) trátase dun espazo maximamente simétrico que é solución das ecuacións do campo de Einstein con curvatura negativa constante. Existen varios sistemas de coordenadas para o espazotempo AdS. Nesta tese utilizaremos as coordenadas de AdS global, as cales abranguen a totalidade do espazotempo.

O espazo AdS é conforme ao universo estático de Einstein. Aínda que a fronteira conforme de AdS está definida salvo unha transformación conforme, ten unha estrutura causal ben definida. A fronteira localizada no infinito espacial é unha superficie tipo tempo. Esta característica ten implicacións significativas no comportamento das xeodésicas e na estrutura causal do espazo AdS. Os raios de luz e as partículas poden chegar á fronteira nun tempo finito.

Ademais, dadas unhas condicións iniciais nunha superficie tipo espazo, o dominio de dependencia futuro non inclúe a totalidade do espazotempo, e estas condicións iniciais non son suficientes para determinar a solución en todo o espazotempo. En AdS é necesario establecer unhas condicións de fronteira na fronteira localizada no infinito espacial.

Pola súa parte, a correspondencia AdS/CFT é unha ferramenta que, como indicamos anteriormente, relaciona unha teoría gravitacional nun espazo AdS cunha teoría de campos conforme definida na súa fronteira nunha dimensión menos. Isto permítenos obter observables nunha das dúas teorías realizando cálculos na outra teoría. A relación entre cantidades aos dous lados da correspondencia coñécese habitualmente como *dicionario holográfico*.

O capítulo 2 desenvolve o modelo empregado nesta tese, consistente en gravidade de Einstein acoplada a un campo escalar en espazotempo AdS_4. Presentamos diferentes tipos de condicións de fronteira que poden ser aplicadas. Ao longo desta tese tratamos dous modelos distintos: un cun campo escalar sen masa, e outro cun campo escalar con $m^2 = -2$.

Ao calcular os modos normais linealizados, obtense que o primeiro modelo presenta uns modos linealizados que son solucións das ecuacións con condicións de fronteira de Dirichlet; e outros modos con condicións de fronteira correspondentes a un valor esperado do operador da teoría dual que se anula. Os primeiros modos son normalizables, pero os segundos non. Os modos normalizables pódense xeneralizar para obter solucións non lineais. Posteriormente, en [10], estas solucións foron xeralizadas a solucións periódicas no tempo onde o valor do campo escalar na fronteira non se anula.

O modelo co campo escalar masivo atópase na chamada xanela de dobre cuantización. Neste modelo, o campo escalar compórtase preto da fronteira como $\phi = \alpha r^{-1} + \beta r^{-2}$. Neste caso, tanto os modos correspondentes a condicións de fronteira $\alpha = 0$ (dual á cuantización estándar na teoría cuántica conforme), como os modos con $\beta = 0$ (dual á cuantización alternativa) son normalizables. Non só son posibles estas condicións de fronteira, senón que o sistema admite condicións de fronteira mixtas da forma $\beta = \beta(\alpha)$. Estas condicións son duais a unha deformación multitraza da teoría de campos conforme dual.

Por outra banda, estudamos as simetrías asintóticas de AdS, e vemos que entre as condicións de fronteira mixta, as únicas que preservan estas simetrías son as deformacións marxinais.

Neste capítulo tamén se tratan as *condicións de esquina* que deben cumprirse ao establecer un problema de valores iniciais e de fronteira. Este requirimento débese a que as ecuacións do movemento relacionan as derivadas espaciais coas derivadas temporais. Isto tamén é válido na intersección entre a superficie tipo espazo coas condicións iniciais e a superficie tipo tempo da fronteira. Como consecuencia disto, as derivadas espaciais das condicións iniciais avaliadas na fronteira están relacionadas coas derivadas temporais no mesmo punto, as cales correspóndense coas derivadas das condicións de fronteira que impoñemos.

O capítulo 3 explora a resposta dun campo escalar real e sen masa sometido a un forzamento periódico no espazo-tempo AdS. Comezando no espazo baleiro de AdS, introducimos a condición de fronteira dependente do tempo de maneira adiabática e mediante unha modulación en amplitude cunha función non analítica, de maneira que todas as derivadas temporais no momento inicial anúlense. Este requirimento débese ás condicións de esquina explicadas anteriormente. O feito de que empecemos a evolución desde o espazo baleiro, onde todas as derivadas espaciais son nulas, implica que as derivadas temporais tamén teñen que anularse. Definimos como β o tempo que dura este *quench* no que se introduce o forzamento.

Nun primeiro paso, aplicamos un forzamento composto por unha soa frecuencia, a cal coincide cunha frecuencia resoante do sistema. Isto produce unha amplificación significativa das oscilacións do campo escalar. Mentres o forzamento está activo, existe un patrón de interferencia

formado por dúas frecuencias. Unha destas frecuencias é a do forzamento, e a outra é lixeiramente inferior e máis faise máis pequena conforme aumenta a amplitude do forzamento. Cando o forzamento se desactiva, permanecen solucións periódicas no tempo. Denominamos estas solucións oscilantes sen forzamento como *oscilóns*, as cales están caracterizadas por un espectro da forma $\omega_{\text{osc}}(2k+1)$ con $k \geq 0$. A frecuencia e a masa do oscilón final dependen da amplitude alcanzada pola excitación, da rapidez da extracción e do momento no que comeza a extracción. A masa final máxima que pode quedar diminúe a medida que a extracción se fai máis lenta. No límite $\beta \to \infty$, o sistema retorna ao baleiro de AdS, do mesmo modo que sucede en xeral cando a excitación se inxecta lonxe da resonancia.

Como seguinte paso, introducimos protocolos nos que despois de introducir o forzamento periódico ata unha certa amplitude, comezamos a modular a frecuencia. Na implementación desta modulación tamén debemos ser coidadosos de cumprir coas condicións de esquina. Mediante este proceso podemos cruzar unha das frecuencias resoantes en sentido ascendente ou descendente. En sentido ascendente, conforme a frecuencia achégase á resonancia $\omega \approx 3$, xorde un forte efecto sobre a métrica, incrementando a masa do sistema. Isto produce un patrón de interferencia entre a frecuencia do forzamento e a frecuencia dun novo oscilón que acaba de producirse. Cando o forzamento se apaga, queda un oscilón.

Se pola contra a frecuencia modúlase no sentido descendente, a evolución é moito máis suave, a masa increméntase pouco a pouco mentres o sistema aproxímase á liña de oscilóns. Podemos deter a modulación nunha frecuencia determinada, e apagar o forzamento, deixando ao final un oscilón cunha masa e frecuencia moi similar á da solución periódica na que nos encontrabamos.

É interesante notar que se a modulación non atravesa ningunha frecuencia resoante, aínda pode suceder que un harmónico superior si cruce unha resonancia, producindo un gas linealizado de oscilóns, mentres a métrica regresa ao baleiro de AdS cando se desactiva o forzamento.

O seguinte que estudamos é a posibilidade de que existan solucións non lineais con valor esperado no baleiro do operador dual sexa nulo. É dicir que xurdan dos modos lineais pares $\omega_{\text{n}} = 2n+2 = 2, 4, \ldots$ Encontramos que se ben este valor esperado faise moi pequeno, non chega a anularse completamente. A nosa interpretación é que estas solucións deberían contar cun forzamento con múltiples frecuencias. A construción destas solucións segue sendo un problema aberto. Para poder resolvelo debemos descubrir como tratar cos modos non normalizables, os cales definen un produto interno diverxente.

Un resultado sorprendente é que para frecuencias baixas do forzamento $\omega_{\text{b}} \leq 1{,}25$ existen solucións periódicas no tempo con masa negativa.

O seguinte paso no estudo deste modelo é excitar o sistema cun forzamento composto por dúas frecuencias. Este introdúcese de distintas formas: de maneira secuencial, realizando unha modulación que atravesa dúas frecuencias, ou introducindo as dúas frecuencias de maneira simultánea. Estes estudos revelaron comportamentos complexos, con espectros da forma: $\omega_k = 2k+1$ con $k \geq 0$, onde a frecuencia dominante pode cambiar co tempo. As solucións obtidas son compatibles coas construcións propostas en [22]. De forma destacable, algúns protocolos de forzamento con múltiples frecuencias son capaces de suprimir a cascada de enerxía mentres o forzamento está activo. Mentres que a cascada reactívase cando se quita o forzamento.

Por último, podemos introducir un forzamento con múltiples modos que simule un ruído térmico como un ruído de Johnson-Nyquist. Neste caso semella que existe un valor do parámetro

T, o cal actúa a modo de temperatura, para o que aparece un limiar que separa evolucións que colapsan para T maiores doutras que non colapsan para temperaturas máis pequenas.

No Capítulo 4 abordamos o impacto das condicións de contorno mixtas na inestabilidade non lineal identificada inicialmente por Bizoń e Rostworowski (inestabilidade BR). Estas condicións de contorno son duais ás deformacións multitraza da Lagranxiana da teoría de campos conforme dual.

Os resultados achados poden resumirse no seguinte. Por unha banda, para deformacións marxinais e irrelevantes, a inestabilidade BR persiste, co tempo de colapso escalando como ε^{-2} para amplitudes dos datos iniciais pequenas. Estas deformacións non alteran a estrutura resoante de AdS. Ademais, realízase unha análise da forma na que escala Π^2 (observable que se encontra relacionado coa curvatura escalar) coa amplitude dos datos iniciais. Compróbase que $\varepsilon^{-2}\Pi^2(\varepsilon^2 t)$ converxe a unha curva universal para amplitudes pequenas, con varias fases de crecemento distinguidas. Esta forma é característica da inestabilidade BR.

Pola contra, as deformacións relevantes, que se corresponden con condicións de fronteira da forma $\beta = c_2\alpha$, rompen o espectro de resonancia de AdS. De forma destacable, o resultado é substancialmente diferente dependendo do signo da deformación. Para $c_2 > 0$ a evolución faise non linealmente estable. Para unha deformación moi grande, $c_2 \gg 1$, o sistema retorna a un comportamento de inestabilidade non lineal, xa que a condición de contorno achégase á condición $\alpha = 0$, correspondente á cuantización estándar na teoría de campos dual.

Para $c_2 < 0$, pola contra, a curva de tempos de colapso apenas difire do caso sen deformación. Unha análise máis profunda do escalado de Π^2 coa amplitude dos datos iniciais revela que o sistema non se comporta como na inestabilidade BR. A mesma análise cunha gaussiana inicial máis ampla amosa unha desviación da curva de tempos de colapso respecto ao caso sen deformación, suxerindo que para amplitudes máis baixas das alcanzadas nas nosas simulacións, veríamos unha desviación da curva de tempo de colapso.

Cremos que a diferenza entre o comportamento para ambos signos de c_2 podería estar relacionada coa interacción entre a descomposición espectral da gaussiana inicial e os modos normais do sistema, os cales dependen do valor de c_2. Para $c_2 < 0$ a descomposición espectral da gaussiana ten un dominio moi forte do modo fundamental. Isto suxire que, mentres para valores positivos moderados de c_2 os datos iniciais poderían caer na illa de estabilidade creada por algúns multiosciloń análogos aos construídos en Ref. [23]. Pola contra, a inestabilidade non lineal para $c_2 < 0$ podería ser unha consecuencia da inexistencia dun multiosciloń dominado polo modo fundamental.

Un apunte a realizar aquí é que tamén realizamos simulacións con deformacións irrelevantes ($\beta = c_4\alpha^3$) con valores de c_4 relativamente grandes de ata $c_4 = 100$. Neste caso para valores positivos, observamos que a curva de tempos de colapso difire do caso sen deformación, volvendo o sistema linealmente estable. Isto fai xurdir unha importante reflexión. Por unha parte, temos que estas deformacións son dunha orde subdominante na análise dos modos linealizados, polo que o espectro resoante non se ve alterado. Por outra banda, as deformacións irrelevantes rompen as simetrías asintóticas de AdS. Aquí é posible preguntarse se este segundo factor ten unha implicación na inestabilidade non lineal do sistema.

Non obstante, a análise dos modos linealizados implica supoñer que $c_n = O(1)$ e $\alpha = O(\gamma)$, onde γ é o parámetro no que se realiza a expansión. Esta suposición non se cumpre para valores

tan altos de c, polo que sería posible que dita deformación si rompese a estrutura resoante do espectro. Entón, poderiamos preguntarnos se ao baixar a amplitude dos datos iniciais e reducir o valor de αc_n, o tempo de colapso volvería a aproximarse ao caso sen deformación. Sexa así ou non, a posible implicación do feito de que estas deformacións rompan a simetría asintótica de AdS na inestabilidade non lineal do sistema segue sendo un problema a estudar.

Ambos estudos subliñan a importancia das resonancias na determinación da dinámica de AdS. O forzamento periódico a frecuencias resoantes amplificou a transferencia de enerxía entre modos, mentres que as desviacións da resonancia en deformacións relevantes romperon esta cascada. Estas observacións destacan a resonancia como un mecanismo clave que impulsa a cascada de enerxía e potenciais inestabilidades.

A presenza de condicións de contorno mixtas introduciu un espazo de parámetros máis amplo para a análise de estabilidade. As deformacións relevantes romperon de maneira efectiva a condición de resonancia exacta, creando illas de estabilidade. Este mecanismo alíñase coa expectativa de que a característica resoante do espectro de AdS é a principal responsable da turbulencia e do colapso.

Concluímos este resumo da tese citando as posibles cuestións que quedan abertas. Aínda que os estudos demostraron unha converxencia de cuarta orde na maioría das simulacións numéricas, as simulacións con múltiples frecuencias no capítulo 3 resultan especialmente esixentes. Unha simulación que manteña a converxencia durante un período máis longo podería detectar o colapso e, quizais, proporcionar máis información sobre como estes impulsos poden deter a cascada de enerxía.

Tal e como se expón na sección 3.8, pensamos que as solucións con valor esperado nulo requiren un forzamento de múltiples frecuencias. A construción numérica destas solucións segue sendo un problema aberto. Obter estas solucións mediante os métodos desenvolvidos en Refs. [5, 24] require tratar con modos non normalizables.

A razón para un comportamento tan diferente en ambos signos de c_2 nas deformacións $\beta = c_2\alpha$ segue sendo unha cuestión por resolver. Para comprobar a nosa hipótese, deberiamos obter os multioscilóns que actuarían como atractores para estabilizar datos iniciais cun c_2 positivo moderado, pero que non logran interactuar con datos cun modo fundamental fortemente dominante.

O feito de que só as deformacións marxinais preserven as simetrías asintóticas de AdS, como se explica en 2.2.3.4, da lugar a preguntarse que sucede coas deformacións irrelevantes, segundo se explicou anteriormente.

Ademais destes modelos específicos, a correspondencia AdS/CFT (con condicións de contorno dependentes do tempo) segue sendo unha área fascinante de exploración, ofrecendo ricas oportunidades para ampliar o noso coñecemento sobre a correspondencia.

Overview

Motivation and objectives

This thesis investigates the dynamics of Einstein gravity coupled to a scalar field in asymptotically anti-de Sitter (AdS) spacetime, focusing on the implications of different boundary conditions. The work builds upon the AdS/CFT correspondence, exploring how scalar field dynamics with time-dependent boundary conditions and boundary deformations of the dual CFT at the boundary affect the stability of AdS space.

In recent decades, the anti-de Sitter/Conformal Field Theory (AdS/CFT) correspondence has emerged as a cornerstone of theoretical physics, providing profound insights into the interplay between gravity and quantum field theories. Proposed by Juan Maldacena in 1997 [3], this duality has opened new paths for exploring strongly coupled quantum field theories and non-perturbative dynamics in string theory. The correspondence proposes a remarkable equivalence between a gravitational theory in a $(d+1)$-dimensional AdS spacetime and a conformal field theory defined on its d-dimensional boundary.

The work of P. Bizoń and A. Rostworowski on AdS instability in 2011 [4] highlighted the unique behaviour of AdS as a gravitational system. Unlike Minkowski or de Sitter spacetimes, AdS was found to be non-linearly unstable. More specifically, they considered spherically symmetric, asymptotically global AdS_4 geometries and found that Gaussian-like initial data of a massless scalar field with Dirichlet boundary conditions always lead to the formation of a black hole, regardless of how small their amplitude ε is. The time until collapse follows a characteristic scaling with the amplitude as ε^{-2}. The mechanism that enables this instability is a turbulent cascade of energy through the normal modes of the system to higher frequencies [4, 22, 25–27]. This process produces an energy concentration on smaller and smaller spatial scales, eventually leading to gravitational collapse. This energy cascade is triggered by the resonant structure of AdS. In this thesis, we will refer to this type of non-linear instability as the *Bizoń-Rostworowski (BR) instability*.

Later works showed that there are some other types of solutions, like oscillons [5, 6], boson stars [7, 8], or static geometries such as solitons in Einstein-Maxwell-scalar theory [9], that are non-linear stable. More recently, work in [10] extended the oscillatory solutions to Time-Periodic Solutions where the scalar field at the boundary does not vanish. This introduces another ingredient, time-periodic boundary conditions.

Most of the works in the context of the AdS/CFT correspondence focus on static geometries which are dual to states of strongly coupled systems at equilibrium. The fact that holography

extends into time-dependent situations is a subject that undoubtedly deserves close attention. Some works, as [10, 28], address dynamical open systems in global AdS, while others explore driven systems in the deconfined phase [29, 30]. In the latter case, the bulk geometry contains a horizon that makes all the energy entering the system to end up heating it, avoiding the formation of a stationary state. This is in agreement with the $\mathrm{O}(N^2)$ imbalance in the degrees of freedom between the quantum theory and the driving bath, which results in the bulk acting as a refrigerator that absorbs all the injected energy [29, 30]. In contrast, in the confined phase, dual to global AdS, there are opportunities for long-lived driven solutions [10, 28].

Part of this thesis is motivated by the search for a deeper understanding of the behaviour of previously mentioned Time-Periodic Solutions near the resonances of the system, not only with a single frequency, but also with the intricate interplay of multiple frequencies in a non-linear system.

Another part of this thesis is motivated by the following idea. The oscillons, boson stars and solitons mentioned earlier break the exactly resonant spectrum of AdS, disrupting the non-linear instability. They act as attractors, creating *islands of non-linear stability* [5,6,31] for initial data. In this thesis, we follow a different approach to this problem. We apply boundary conditions, corresponding to a deformed CFT, where the resonant structure of AdS is explicitly broken from the beginning.

We will work with a top-down AdS_4-Einstein-scalar system where the scalar field mass squared lies within the so-called double-quantization window. In this scenario, the system allows for mixed boundary conditions, also known in the literature as designer gravity (see Refs. [23, 32, 33] for recent studies of AdS-Einstein-scalar systems with a particular kind (Robin) of designer gravity boundary conditions). This approach can be thought of as the natural analogue of the flat space problem discussed in Refs. [8, 11, 12], where a spherically symmetric geometry supported by a massless scalar field enclosed in a box was considered. In this flat space case, the choice between Dirichlet or Neumann boundary conditions for the scalar field is in one-to-one correspondence with the resonant or non-resonant nature of the spectrum and the presence or absence of the BR instability.

In the context of holography, designer gravity boundary conditions correspond to multi-trace deformations of the boundary CFT [13, 14]. In the past, multi-trace deformations have been employed to engineer unbounded effective field theory potentials supporting big crunch cosmologies in the bulk [15, 16], quantum quenches [17] or phase transitions [18–20]. Our results on the non-linear stability of AdS_4 with designer gravity boundary conditions can be regarded as exploring the effect of multi-trace deformations on the thermalization of spatially homogeneous states in ABJM theory [21] placed on a two-sphere.

Outline

The structure of this thesis is as follows. Chapter 1 provides the theoretical framework, introducing the AdS spacetime properties and the AdS/CFT correspondence. It also reviews the characteristic features of the previously mentioned non-linear instability discovered by Bizoń and Rostworowski.

Chapter 2 develops the model employed in this thesis, consisting of Einstein gravity coupled to a scalar field in Ad_4 spacetime. We present different types of boundary conditions that can be applied. Key features such as the linearized theory and the normal modes of the system, the *corner conditions* that must be satisfied for a well-posed initial-boundary value problem, and the time-periodic boundary solutions are analysed. This chapter also discusses the mathematical formulation of mixed boundary conditions and their interpretation as multi-trace deformations of the dual CFT. Finally, it introduces the concept of AdS asymptotic symmetries.

In chapter 3, we explore the dynamics of AdS spacetime with a massless scalar field under a time-periodic driving. We study single-frequency, double-frequency, and multi-frequency driving scenarios, with special attention to the regions near the resonant frequencies of the system. Several protocols of driving injection and frequency modulation are implemented to gain insight into the behaviour of the system near the resonances, such as the formation of oscillons and the role of resonant drivings in the formation of energy cascades and instability. We also explore solutions with vanishing v.e.v., and identify configurations with a low-frequency driving that lead to negative mass solutions.

In chapter 4, we turn to a system with a massive scalar field in the double-quantization window to address the aforementioned approach based on mixed boundary conditions (interpreted as multi-trace deformations of the dual CFT), which allow us to explicitly break the resonant structure of the AdS spectrum from the start. With this approach, we explore the non-linear instability of AdS from a different perspective.

Finally, chapter 5 summarizes the results of this work, highlighting the key insights gained regarding the interplay between the different boundary conditions implemented and the non-linear dynamics of the AdS spacetime.

Methodology

The methodology used can be divided into two parts: analytical work and numerical work.

The treatment of highly non-linear solutions often requires the use of numerical simulations. Codes have been developed to simulate different boundary conditions in asymptotically AdS spaces. This is technically delicate and resource-intensive. For this purpose, codes have been generated in various programming languages. A large part has been implemented in Python using the JIT compiler Numba [34], although parallelized codes in Fortran (using MPI [35]) and C (using CUDA [36]) have also been used. The parallelized programs were executed using the resources provided by CESGA (Centro de Supercomputación de Galicia).

Regarding the analytical work, most of the necessary symbolic computation has been performed using Wolfram Mathematica software [37].

Chapter 1

Introduction

In this chapter, some general concepts for the comprehension of this thesis are presented. Firstly, there is a brief introduction to the anti-de Sitter spacetime, its possible coordinate systems and its conformal boundary and causal structure. This last concept is a key feature of the AdS/CFT correspondence and has important implications when applying boundary conditions, which is the main issue treated in this thesis. Then, some general concepts of the mentioned AdS/CFT correspondence are introduced. Finally, we introduce the AdS instability problem, a concept that will be present throughout the whole thesis every time we perform time evolutions with some boundary conditions.

1.1. Anti-de Sitter spacetime

Anti-de Sitter (AdS) spacetime arises as a maximally symmetric solution to Einstein's vacuum field equations. It serves as a cornerstone in diverse areas of study, from string theory and the AdS/CFT correspondence to black hole thermodynamics and quantum gravity. This chapter provides an introduction to AdS spacetime.

A maximally symmetric spacetime is one that possesses the largest possible number of Killing vectors. In D dimensions, such a spacetime has $D(D+1)/2$ Killing vectors.[1] AdS is a maximally symmetric spacetime with constant negative curvature, and its isometry group in $d+1$ dimensions is $\mathrm{SO}(2,d)$.[2]

Formally, an AdS space can be seen as a Lorentzian manifold that solves Einstein's vacuum field equations with a negative cosmological constant $\Lambda < 0$:

$$R_{\mu\nu} - \frac{1}{2} R g_{\mu\nu} + \Lambda g_{\mu\nu} = 0. \tag{1.1}$$

[1] For AdS_4, Appendix A shows the 10 corresponding Killing vectors. We will use them in 2.2.3 when exploring the AdS asymptotic symmetries.

[2] See, for example, [38] for a detailed discussion on this and other aspects of the anti-de Sitter spacetime.

The curvature radius l of AdS$_{d+1}$ space is related to the cosmological constant by

$$\Lambda = -\frac{d(d-1)}{2l^2}. \tag{1.2}$$

1.1.1. Coordinate systems

The AdS$_{d+1}$ metric can be written in several coordinate systems, the most common being global coordinates:

$$ds^2 = -\left(1+\frac{r^2}{l^2}\right)dt^2 + \frac{dr^2}{1+\frac{r^2}{l^2}} + r^2 d\Omega_{d-1}^2, \tag{1.3}$$

where $t \in (-\infty, +\infty)$, $r \in [0, \infty)$ and $d\Omega_{d-1}^2$ represents the metric on the $(d-1)$-dimensional sphere ($\theta \in [0, \pi]$ and $\phi \in [0, 2\pi)$). In these coordinates, the conformal boundary is located at $r \to \infty$.

The radial coordinate r can also be compactified by the transformation $r = l \tan x$ and $t = l\tau$, giving:

$$ds^2 = \frac{l^2}{\cos^2 x}\left(-d\tau^2 + dx^2 + \sin^2 x d\Omega_{d-1}^2\right), \tag{1.4}$$

where $\tau \in (-\infty, +\infty)$ and $x \in [0, \pi/2)$. The conformal boundary is now located at $x = \pi/2$. These will be the coordinates mainly used throughout this thesis.

Another interesting coordinate system is the so-called Poincaré patch. This can be obtained starting with the metric in global coordinates (1.3) and considering the following rescaling:

$$r \to \lambda r\ ,\ \ t \to t/\lambda. \tag{1.5}$$

After taking the limit $\lambda \to \infty$, the metric (1.3) becomes

$$ds^2 = -\frac{r^2}{l^2}dt^2 + \frac{l^2}{r^2}dr^2 + \lambda^2 r^2 d\Omega_{d-1}^2. \tag{1.6}$$

Observe in the last term that the radius of S^{d-1} diverges for $\lambda \to \infty$. In this limit, S^{d-1} becomes flat and looks locally as $\mathbb{R}^{d-1}$. Then, we can define coordinates near a point $P \in S^{d-1}$ such that $\lambda^2 r^2 d\Omega_{d-1}^2 = d\vec{x}^2$. Finally, the metric becomes

$$ds^2 = -\frac{r^2}{l^2}dt^2 + \frac{r^2}{l^2}d\vec{x}^2 + \frac{l^2}{r^2}dr^2. \tag{1.7}$$

or, alternatively, after the change $r = l^2/z$:

$$ds^2 = \frac{l^2}{z^2}(-dt^2 + d\vec{x}^2 + dz^2). \tag{1.8}$$

Now the radial coordinate is $z > 0$, and the conformal boundary of the AdS space is located at $z = 0$. It is worth noting that since $z > 0$, the Poincaré patch covers only half of the complete space.

As mentioned before, AdS$_{d+1}$ isometry group is SO$(2, d)$. It turns out that AdS$_{d+1}$ can also

be obtained as a space embedded in a higher-dimensional flat space with signature $(2, d)$. This $(d+2)$-dimensional space is described by the metric

$$ds^2 = -dX_0^2 - dX_{d+1}^2 + dX^i dX_i \tag{1.9}$$

with $i = 1, ..., d$, and AdS_{d+1} can be visualized as a hyperboloid embedded in this $(d+2)$-dimensional space:

$$-X_0^2 - X_{d+1}^2 + \sum_{i=1}^{d} X_i^2 = -l^2. \tag{1.10}$$

This embedding provides an intuitive way to understand the negative curvature and global structure of AdS. By introducing suitable coordinates, the induced metric on the hyperboloid can take the form of (1.3) or (1.4). However, the time coordinate obtained through this embedding is periodic, returning to the same point after completing a full revolution around the hyperboloid. Since this periodicity is not explicit in (1.3) or (1.4), one can unwrap the S^1 circle and take $t \in (-\infty, +\infty)$, thereby avoiding closed time curves. This procedure leads to the so-called *universal covering space* of AdS (see, for example, [38]).

1.1.2. Conformal boundary and causal structure

We now explore the conformal structure of the AdS spacetime at the boundary, which is a key feature of the AdS/CFT correspondence and essential for the implementation of boundary conditions. Firstly, we start by defining the following space, known as the Einstein Static Universe:

$$ds^2 = R^2 \left(-d\tau^2 + dx^2 + \sin^2 x d\Omega_{d-1}^2\right), \tag{1.11}$$

where R is a constant, and the coordinate range is $\tau \in (-\infty, \infty)$, $x \in (0, \pi)$. From global coordinates in the form of (1.4), it can be observed that AdS is conformal to the Einstein Static Universe for the region $x \in [0, \pi/2)$,

$$ds_{\text{ESU}}^2 = \Omega(x) ds_{\text{AdS}}^2, \tag{1.12}$$

with a conformal factor $\Omega = \cos^2 x$ and $R = l$. The conformal boundary of AdS is located at $\Omega(x) = 0$ ($x = \pi/2$).

Although the conformal boundary is defined up to a conformal transformation, it has a well-defined causal structure. This boundary located at spatial infinity is a timelike surface. This feature has significant implications for the behaviour of geodesics and the causal structure of AdS space. Massless particles can reach the boundary in finite time, a feature that is central to the holographic principles underlying the AdS/CFT correspondence.

Moreover, given initial data on a certain spacelike surface S, the future domain of dependence[3] (or Cauchy development) does not cover the entire spacetime, meaning that the initial data alone are insufficient to determine the evolution in the complete space. In AdS, boundary conditions

[3] The future domain of dependence $D^+(S)$ includes all the points for which every causal curve that reaches those points has passed through S. This implies that all the information necessary to find a solution in $D^+(S)$ is contained in S.

at spatial infinity must also be specified. Throughout this thesis, we will deal with Cauchy evolution in AdS and explore various types of boundary conditions that can be imposed.

1.2. AdS/CFT correspondence

The Anti-de Sitter/Conformal Field Theory (AdS/CFT) correspondence, also known as holography, is one of the most groundbreaking discoveries in theoretical physics, providing a precise framework for understanding the interplay between gravity and quantum field theory. Introduced by Juan Maldacena in 1997 [3], this duality has transformed our approach to quantum gravity, strongly coupled quantum field theories, and various aspects of string theory. Some comprehensive reviews on these topics include [39, 40].

The *holographic principle*, proposed by 't Hooft [41] and Susskind [42], states that the number of degrees of freedom in a quantum gravity theory is not proportional to the volume of a region, but instead scales with the area of its boundary.

As a concrete realization of this principle, the AdS/CFT correspondence proposes a duality between a $(d+1)$-dimensional gravitational theory in an AdS spacetime and a d-dimensional conformal field theory (CFT) defined on its boundary. This correspondence is holographic in nature, implying that the bulk physics of AdS can be entirely encoded in the lower-dimensional boundary theory. The AdS/CFT duality emerged from insights in string theory, particularly the study of D-branes. Maldacena's original conjecture involved type IIB string theory on $AdS_5 \times S^5$, which is dual to $\mathcal{N} = 4$ super Yang-Mills theory in four dimensions with gauge group SU(N).

The correspondence relates the parameters of the two theories. The AdS radius l and the string length l_s are related by [3, 39]

$$\frac{l^4}{l_\mathrm{s}^4} = N g_\mathrm{YM}^2 \equiv \lambda, \tag{1.13}$$

where g_YM is the Yang-Mills coupling, and λ is the 't Hooft coupling [43]. On the other hand, the string coupling constant g_s and the Yang-Mills coupling are related through [3, 39]

$$4\pi g_s = g_\mathrm{YM}^2 = \frac{\lambda}{N}. \tag{1.14}$$

According to (1.14), if we take the $N \gg 1$ limit while keeping the 't Hooft coupling λ fixed, then $g_s \to 0$, and corrections from string diagrams with loops are suppressed. Then, we can take the $\lambda \gg 1$ limit, which corresponds to a strong coupling of the gauge theory. According to (1.13), this limit implies that the string length l_s becomes negligible compared to the AdS radius l, and the string theory is reduced to classical gravity.

In summary, we reach a limit in which classical gravity in the AdS bulk corresponds to the strong coupling limit of the CFT, enabling calculations in regimes otherwise inaccessible.

1.2.1. Holographic dictionary

Mathematically, the correspondence is often expressed as:

$$Z_{\text{gravity}}[\phi \to \phi_0] = Z_{\text{CFT}}[\phi_0], \tag{1.15}$$

where Z_{gravity} is the gravitational partition function and Z_{CFT} is the partition function of the CFT. ϕ represents fields in the bulk gravitational theory, and their values at the boundary ϕ_0 serve as sources for operators $\mathcal{O}$ with dimension Δ in the CFT.

For the aforementioned limit in which we can consider classical gravity, the left-hand side of (1.15) becomes

$$Z_{\text{gravity}}[\phi \to \phi_0] \simeq \exp\left[-S^{\text{ren}}_{\text{gravity}}(\phi \to \phi_0)\right], \tag{1.16}$$

where $S^{\text{ren}}_{\text{gravity}}$ is the renormalized classical action obtained after cancelling the divergence terms from the on-shell action.

For the right-hand side of (1.15), in the CFT the correlators can be calculated by deforming the Lagrangian as

$$\mathcal{L} \to \mathcal{L} + \phi_0(x)\mathcal{O}(x) \tag{1.17}$$

and utilizing the generating functional

$$Z_{\text{CFT}}(\phi_0) = \left\langle \exp\left[-\int_{\partial \text{AdS}} \phi_0(x)\mathcal{O}(x)\right]\right\rangle_{\text{CFT}} \tag{1.18}$$

Correlation functions for an operator $\mathcal{O}$ of the CFT can then be computed by differentiation with respect to the boundary scalar field:

$$\langle \mathcal{O}(x_1)...\mathcal{O}(x_n)\rangle = \left.\frac{\delta^{(n)} S^{\text{ren}}_{\text{gravity}}(\phi)}{\delta\varphi(x_1)...\varphi(x_n)}\right|_{\varphi=0}, \tag{1.19}$$

where

$$\varphi \equiv \lim_{z\to 0} z^{\Delta-d}\phi(z,x) \tag{1.20}$$

is the value of the scalar field at the boundary ϕ_0 once the divergence produced by its asymptotic behaviour near the boundary ($z \to 0$) is removed.

The set of relations between quantities on both sides of the correspondence, which allows us to obtain observables in one theory by performing computations in the dual theory, is usually known as the *holographic dictionary*.

1.3. AdS instability: Bizoń-Rostworowski collapse

An important part of this thesis is related to the topic of instability in anti-de Sitter (AdS) spacetime. Among the three maximally symmetric spacetimes, Minkowski and de Sitter are known to be non-linearly stable [44, 45]. The non-linear stability of global AdS space has been

under intense scrutiny since the seminal work of P. Bizoń and A. Rostworowski in 2011 [4]. In this section, we mostly address the results described in that work about the AdS instability and the characteristic features of the mechanism that leads the system to collapse after a cascade of energy to higher modes.

As we observed in 1.1.2, a crucial feature of the AdS space is the existence of a timelike boundary at spatial infinity, and initial data at a spacelike surface are not sufficient for performing the evolution in the whole space. Instead, it is necessary to set some boundary conditions on the boundary at infinity.

One can set some boundary conditions where there is no flux of energy at the boundary. A paradigmatic example of this situation is a massless scalar field with Dirichlet boundary conditions. As we will see in the description of this model in 2.1, the conservation law of the energy-momentum tensor (2.9) – (2.10) establishes that a fixed scalar field at the boundary ϕ_0 with no time dependence implies that $\langle T_{00} \rangle$ is conserved. In [4], the authors address the question of the stability of AdS under this setup.

1.3.1. Bizoń-Rostworowski instability

In the previously mentioned work, Ref. [4], the authors consider spherically symmetric, asymptotically global AdS_4 geometries supported by a massless scalar field. This is the same model that we will describe in detail in section 2.1, with the following ansatz for the metric:

$$ds^2 = \frac{l^2}{\cos^2 x}\left(-f(t,x)e^{-2\delta(t,x)}dt^2 + f^{-1}(t,x)dx^2 + \sin^2 x d\Omega_2^2\right). \tag{1.21}$$

They imposed Dirichlet boundary conditions by fixing the scalar field at the boundary, $\phi(t, x = \pi/2) = 0$.

Starting with Gaussian-type initial data with small width σ, the scalar field is localized in space and propagates as a wave packet. The dynamics of the system are as follows. Beginning with a large enough amplitude ε of the scalar field, the system collapses into a black hole before the wave packet is able to travel until the boundary, and an apparent horizon is formed at a certain radius x_{h}. As long as the initial amplitude decreases, the horizon appears at a smaller radius until $x_h \to 0$ for a certain value of ε. If an even lower amplitude is introduced, then the scalar field wave packet travels up to the boundary located at infinity and leads the system into collapse when returning near the origin. If smaller and smaller amplitudes of the initial data are set, then the same behaviour repeats over and over, and the scalar field travels multiple times between the boundary and the origin before eventually collapsing. It takes a time of $t \approx \pi$ for the scalar field to travel a complete trip around the whole space. This behaviour can be observed in Fig. 1 in [4].

Another characteristic feature of this instability can be observed by exploring the behaviour of the scalar curvature at the origin, since this observable can properly signal the emergence of instability. For each evolution, at the beginning the value of the scalar curvature is upper bounded by its initial value. After some time, it starts to grow almost exponentially, entering several distinct stages of progressively amplified growth. The most distinctive feature of this type of instability is that the emergence of the first growing phase scales as ε^{-2}, and initial

data consisting of a Gaussian with small width σ always start growing, no matter how small their amplitude ε was. We will refer to this type of instability as the *Bizoń-Rostworowski (BR) instability*.

We will use in chapter 4 this analysis of the scalar curvature to provide additional evidence of the existence of this type of instability.

1.3.2. Linearized modes analysis and energy cascade

We will now introduce the mechanism that produces this instability using the tools of the non-linear perturbation theory. The equations of motion allow a power series expansion for the metric and the scalar field around AdS. This process is described in 2.1.1, where the equations of motion (2.3) – (2.4) with $V(\phi) = 0$ are solved order by order for a spherically symmetric ansatz (2.2). At the first order, we obtain the linearized normal modes for the scalar field

$$\phi_1(t, x) = \cos(\omega_n t) e_n(x), \tag{1.22}$$

with[4]

$$e_n(x) = \sqrt{\frac{16(n+1)(n+2)}{\pi}} \cos^2 x \, {}_2F_1(-n, 3+n; \frac{3}{2}; \sin^2 x), \tag{1.23}$$

where ${}_2F_1$ are the hypergeometric functions. Their corresponding eigenvalues are

$$\omega_n^2 = (2n+3)^2 l^{-2}. \tag{1.24}$$

At the second order, there appears the backreaction on the metric, which depends on the first-order scalar field. At the third order (and higher odd orders), there is an equation of the form

$$\ddot{\phi}_3 + L\phi_3 = S_3, \tag{1.25}$$

where $L = -\cot^2 x \, \partial_x \left(\tan^2 x \, \partial_x\right)$, and the inhomogeneous term S_3 depends on the scalar field and metric corrections obtained at previous orders.

In general, S_3 can contain terms proportional to $\cos \omega_n t$ or $\sin \omega_t$, which are referred to as resonant terms and generate secular terms in ϕ_3. As already noted in [4], each triad (n_1, n_2, n_3) defines a resonant channel characterized by:

$$\omega_n = \omega_{n_1} + \omega_{n_2} - \omega_{n_3}. \tag{1.26}$$

The authors in [4] proposed this mechanism as being responsible for producing an energy cascade to higher modes, ultimately leading the system to collapse.

To perform an analysis of the energy spectrum, one can define the following projections:

$$\Phi_n \equiv (\sqrt{f}\Phi, e_n') \, , \quad \Pi_n \equiv (\sqrt{f}\Pi, e_n), \tag{1.27}$$

[4] This is just another way of rewriting (2.14). For a massless scalar field in 4 dimensions, $\Delta_- = 0$ and $\Delta_+ = 3$.

where Φ and Π are defined in Eq. (2.3) as:

$$\Phi \equiv \phi', \qquad \Pi \equiv \frac{e^{\delta}}{f}\dot{\phi}. \tag{1.28}$$

Then the total energy can be defined as

$$E = \sum_{n=0}^{\infty} E_n(t) = \sum_{n=0}^{\infty} (\Pi_n^2 + \omega_n^{-2}\Phi_n^2), \tag{1.29}$$

where $E_j(t)$ corresponds to the energy of the mode n. An analysis of the time evolution of the energy spectrum (see Fig. 3 in [4]) shows that the mechanism behind the BR instability is a weakly turbulent cascade of energy (occurring at non-linear order) to progressively higher frequencies (smaller spatial scales), which eventually leads to the formation of a black hole on times scaling as ε^{-2} in the $\varepsilon \to 0$ limit.

After the work of Bizon and Rostworoski, various methods have been developed to describe the dynamics of this mechanism and address the role of resonances. The Two-Time Formalism [22] is a multi-scale method that introduces a *slow time* to characterize the energy transfer between modes, and is able to describe both direct and inverse cascades of energy. Additional methods have also been proposed in [46, 47].

Chapter 2

The model: Einstein gravity with a scalar field

The main model that we will use throughout this thesis consists of four-dimensional Einstein gravity with a negative cosmological constant and a spherically symmetric real scalar field,

$$S = \frac{1}{16\pi G}\int d^4x\sqrt{-g}\,(R-2\Lambda) - \frac{1}{2}\int d^4x\sqrt{-g}\,(\partial_\mu\phi\partial^\mu\phi - V(\phi)) + S_{\rm GHY} + S_{\rm ct}, \quad (2.1)$$

where the cosmological constant is given by $\Lambda = -3\,l^{-2}$. $S_{\rm GHY}$ and $S_{\rm ct}$ are the Gibbons-Hawking-York and the counterterms actions respectively.

In this thesis, we work with two systems, one with a massless scalar field, where $V(\phi) = 0$, and another with a massive one with $m^2 = -2\,l^{-2}$. We will see that there are differences between both systems when setting boundary conditions. In the massless case, the linearized normal modes corresponding to solutions with vanishing v.e.v. in the dual theory are non-normalizable. In contrast, a scalar field with $m^2 = -2\,l^{-2}$ is in a range of values for the mass where the solutions with zero v.e.v. are also normalizable and the scalar field allows an alternative quantization [48, 49]. Moreover, more general boundary conditions are possible in this second case, where neither the source nor the v.e.v. vanish [50, 51].

In both cases, we are interested in spherically symmetric geometries with the following ansatz:

$$ds^2 = \frac{l^2}{\cos^2 x}\left(-f(t,x)e^{-2\delta(t,x)}dt^2 + f^{-1}(t,x)dx^2 + \sin^2 x\, d\Omega_2^2\right), \quad (2.2a)$$

$$\phi = \phi(t,x), \quad (2.2b)$$

where $x \in [0,\pi/2)$ parameterizes the radial direction, with $x=0$ being the origin and $x=\frac{\pi}{2}$ the asymptotic boundary. Global AdS_4 corresponds to a vanishing $\phi(t,x)=0$ and is given by $f(t,x)=1$ and $\delta(t,x)=0$. From now on, we set the AdS radius as $l=1$.

The equations of motion follow from the action (2.1) with the ansatz (2.2). The effective system of equations is conveniently expressed in terms of the following variables:

$$\Phi \equiv \phi', \qquad \Pi \equiv \frac{e^{\delta}}{f}\dot{\phi}, \tag{2.3}$$

where $\dot{}$ and $'$ represent the time and spatial derivatives respectively. With these definitions, the equations of motion become

$$\dot{\Phi} = (fe^{-\delta}\Pi)', \tag{2.4a}$$

$$\dot{\Pi} = \frac{1}{\tan^2 x}(\tan^2 x f e^{-\delta}\Phi)' - \frac{e^{-\delta}}{\cos^2 x}\frac{dV(\phi)}{d\phi}, \tag{2.4b}$$

$$\delta' = -4\pi G \sin x \cos x \left(\Phi^2 + \Pi^2\right), \tag{2.4c}$$

$$f' = \frac{1+2\sin^2 x}{\sin x \cos x}(1-f) + f\delta' - 8\pi G \tan x V(\phi), \tag{2.4d}$$

There is an additional equation of motion—the momentum constraint—that holds when the rest do. It is given by

$$\dot{f} = -8\pi G \sin x \cos x e^{-\delta} f^2 \Pi\Phi. \tag{2.5}$$

In practice, we will use this equation to monitor the overall quality of our numerical simulations in chapters 3 and 4.

2.1. Massless scalar field

We start describing the case with a massless scalar field $m^2 = 0$. Expanding near the boundary $x = \pi/2$ and solving the equations of motion yields:

$$\phi(t,x) = \phi_0(t) - \frac{1}{2}\ddot{\phi}_0(t)(\pi/2-x)^2 + \phi_3(t)(\pi/2-x)^3 + \mathcal{O}((\pi/2-x)^4), \tag{2.6a}$$

$$\delta(t,x) = \frac{1}{2}\dot{\phi}_0^2(t)(\pi/2-x)^2 + \mathcal{O}((\pi/2-x)^4), \tag{2.6b}$$

$$f(t,x) = 1 - \dot{\phi}_0^2(t)(\pi/2-x)^2 + f_3(t)(\pi/2-x)^3 + \mathcal{O}((\pi/2-x)^4), \tag{2.6c}$$

where we have chosen the coordinate time at the boundary to coincide with the proper time, so that $\delta(t, x = \pi/2) = 0$. The coefficient function $f_3(t)$ is related to the instantaneous mass of the system and is given by a radial integral that is constructed with $\phi(t,x)$ and $\delta(t,x)$. Rewriting the metric (2.2a) in Fefferman-Graham coordinates g_{ij}^{FG} [52],

$$ds^2 = \frac{1}{r^2}(dr^2 + g_{ij}^{\mathrm{FG}}(r)dx^i dx^j), \tag{2.7}$$

where

$$g^{\mathrm{FG}}(r) = g_{(0)}^{\mathrm{FG}} + g_{(2)}^{\mathrm{FG}} r^2 + g_{(3)}^{\mathrm{FG}} r^3 + \mathcal{O}(r^4), \tag{2.8}$$

we have $g^{\rm FG}_{(3)ij} = -\text{diag}\left(\frac{2}{3}f_3, \frac{1}{3}f_3, \frac{1}{3}f_3 \sin^2\theta\right)$. Then the energy-momentum tensor of the dual theory is given by [53]

$$\langle T_{ij}\rangle = \frac{3}{16\pi G} g^{\rm FG}_{(3)ij} = -\frac{1}{8\pi G}\text{diag}\left(f_3, \frac{1}{2}f_3, \frac{1}{2}f_3 \sin^2\theta\right). \tag{2.9}$$

The following constraint,

$$\dot{f}_3 = 6\phi_3\dot{\phi}_0, \tag{2.10}$$

is the tt component of the conservation law for the energy-momentum tensor that follows from coordinate reparametrization invariance. Finally, the function $\phi_3(t)$ is related by the holographic dictionary to the v.e.v. of the scalar operator $\mathcal{O}$, dual to $\phi(t,x)$.

2.1.1. Linearized theory: normal modes

We analyse here the linearized theory in the background of global AdS, which corresponds to $f(t,x) = 1$, $\delta(t,x) = 0$. The equations of motion allow the following power series expansion around AdS for the metric and the scalar field:

$$\phi(t,x) = \sum_{n=0}^{\infty} \phi_{2n+1}(t,x)\gamma^n, \tag{2.11a}$$

$$f(t,x) = 1 - \sum_{n=1}^{\infty} f_{2n}(t,x)\gamma^n, \tag{2.11b}$$

$$\delta(t,x) = \sum_{n=1}^{\infty} \delta_{2n}(t,x)\gamma^n. \tag{2.11c}$$

Inserting this ansatz in the equations of motion (2.4) and solving order by order in γ, we find at the first order:

$$\partial_t^2\phi_1 + L\phi_1 = 0\,, \quad \text{with } L = -\frac{1}{\tan^2 x}\partial_x(\tan^2 x\,\partial_x). \tag{2.12}$$

This equation can be solved by separation of variables,

$$\phi_1(t,x) = \cos(\omega_n t)e_n(x), \tag{2.13}$$

leading to the following normal modes and their corresponding eigenfrequencies:

$$e_n^{\pm}(x) = \cos^{\Delta_\pm} x P_n^{(\frac{3}{2}-1,\Delta_\pm-\frac{3}{2})}(\cos(2x))\,, \qquad \omega_n = 2n + \Delta_\pm, \tag{2.14}$$

where $n = 0, 1, 2, ...$ and $P_n^{(\alpha,\beta)}$ are the Jacobi polynomials. For the case we are analysing with $d = 3$, we have $\Delta_- = 0$ or $\Delta_+ = 3$, and (2.14) represents two types of solutions:

1. Solutions $e_n^+(x)$ have been obtained imposing Dirichlet boundary conditions $e_n^+(\pi/2) = 0$, which correspond to $\phi_0(t) = 0$ in the expansion (2.6a) and vanishing source in the AdS/CFT language. This situation represents the standard quantization in the dual CFT.

These solutions are normalizable with the inner product defined by

$$(e_m^+, e_n^+) = \int_0^{\frac{\pi}{2}} e_m^+ e_n^+ \tan^2 x = \delta_{mn}. \tag{2.15}$$

2. On the other hand, we have $e_n^-(x)$, which are solutions obtained by imposing boundary conditions of the form $\partial_x^3 e_n^-(x)|_{x=\pi/2} = 0$, which correspond to $\phi_3 = 0$ in the expansion (2.6a) and vanishing v.e.v. in the CFT. Contrary to the $e_n^+(x)$ solutions, these solutions are non-normalizable.

The normalizable solutions $e_n^+(x)$ can be promoted to full non-linear oscillating solutions up to fairly high values of the amplitude. This is done in [5] using two different methods: a non-linear perturbative construction, and a fully non-linear numerical evolution using a pseudo-spectral code. Here we will term these non-linear solutions as *oscillons*.

2.1.2. Initial-boundary value problem: corner conditions

In this thesis, we will be interested in solutions where the value of the scalar field at the boundary $\phi(t, x = \frac{\pi}{2}) \equiv \phi_{\rm b}(t)$ is established, i.e., we will impose time-dependent boundary conditions. These are also known as driven systems.

We want to start with AdS vacuum and switch on a time-dependent source $\phi_{\rm b}(t)$. We will see in this section that, given initial data on a spacelike surface, it is generally not possible to specify arbitrary data on the timelike boundary. However, there exists an infinite set of corner conditions that must be satisfied at the intersection of the initial data surface and the boundary.

Starting from the initial data at $t = 0$, the equations of motion (2.4) determine time derivatives of the metric and the scalar field at every point in space. This is true also at the boundary. If we take a time derivative of these equations, we can obtain the value of higher time derivatives as a function of the initial data. Repeating this process, all time derivatives can be obtained at the initial time $t = 0$. Therefore, all time derivatives of the scalar field at the boundary are determined by the given initial data at $t = 0$.

To be more precise, we can expand the equations of motion near the boundary in terms of $\left(\frac{\pi}{2} - x\right)$, and introduce generic initial data whose behaviour near the boundary is given by

$$\begin{aligned} \Phi\left(t = t_0, x\right) &= \sum_{n\geq 0} \Phi_n \left(\frac{\pi}{2} - x\right)^n, \qquad \Pi\left(t = t_0, x\right) = \sum_{n\geq 0} \Pi_n \left(\frac{\pi}{2} - x\right)^n, \\ f\left(t = t_0, x\right) &= \sum_{n\geq 0} f_n \left(\frac{\pi}{2} - x\right)^n, \qquad \delta\left(t = t_0, x\right) = \sum_{n\geq 0} \delta_n \left(\frac{\pi}{2} - x\right)^n. \end{aligned} \tag{2.16}$$

We require that the equations vanish order by order and obtain time derivatives of the metric and the scalar field as a function of the coefficients in (2.16) (spatial derivatives at the boundary). Then we can take time derivatives of the equations and repeat the same process to obtain higher time derivatives of the metric and the scalar field.

Table 2.1 shows the result of this procedure up to the 5th time derivative for the case of a

massless scalar field. This table is interpreted in the following way: n, specified in each row, corresponds to the order in the spatial expansion of the variables near the boundary (2.16); while k, set in each column, means the k-th time derivative. So the k column shows the spatial expansion near the boundary of the k-th time derivative of the variable indicated on the left. The shape in which the cells are filled is related to the fact that the expansions (2.16) are introduced up to a finite order in n and how the structure of the equations relates time derivatives to spatial derivatives. Of course, more terms can be obtained.

We are interested in the implications that these corner conditions have in the driving $\phi\left(t, x=\frac{\pi}{2}\right)$ that we can introduce in the boundary. We have that

$$\Pi\left(t, x=\frac{\pi}{2}\right) = \frac{e^{\delta\left(t,x=\frac{\pi}{2}\right)}}{f\left(t, x=\frac{\pi}{2}\right)}\dot{\phi}\left(t, x=\frac{\pi}{2}\right) = \dot{\phi}\left(t, x=\frac{\pi}{2}\right), \tag{2.17a}$$

$$\Pi^{(k)}\left(t, x=\frac{\pi}{2}\right) = \phi^{(k+1)}\left(t, x=\frac{\pi}{2}\right). \tag{2.17b}$$

So the row with $n = 0$ for Π in table 2.1 represents the derivatives of the scalar field at the boundary. It is worth noting that not only are some leading corrections in the near-boundary expansion of the metric and the scalar field relevant, but higher time derivatives of the boundary are related to higher spatial derivatives of the initial data. Therefore, these conditions imply all the spatial derivatives at the boundary at $t = t_0$.

In the simplest case of setting AdS vacuum as the initial data, all the coefficients Π_n and Φ_n are zero. Note that although f_3 remains undetermined by the equations of motion near the boundary, the full function $f(t = t_0, x)$ is obtained for all x by integrating (2.4c) – (2.4d) once $\Pi(t = t_0, x)$ and $\Phi(t = t_0, x)$ are specified. In AdS vacuum $f(t = t_0, x) = 1$, so $f_3 = 0$. In this situation, we conclude observing the $n = 0$ for Π in table 2.1 that starting with AdS vacuum necessarily implies that all time derivatives of the driving $\phi(t, x = \frac{\pi}{2})$ must vanish.

However, this is not the end of this issue. It is well known that initial data on a spacelike surface can not, by themselves, determine the solution outside their future domain of dependence or Cauchy development. This does not contradict the corner conditions. Although all time derivatives of the scalar field at the boundary at $t = t_0$ are fixed, it is still possible to modify $\phi(t, x = \frac{\pi}{2})$ for $t > t_0$ in a non-analytic way as long as the conditions for the time derivatives at $t = t_0$ are met.

For completeness, we note that a similar issue arises in the other model we work with in section 4, consisting of a massive scalar field with $m^2 = -2$ that decays near the boundary as

$$\phi = \frac{\alpha}{r} + \frac{\beta}{r^2} + \dots. \tag{2.18}$$

In that case, we ensure that all the spatial derivatives of the initial data vanish at the boundary, and we also set $\dot{\alpha}(t) = \dot{\beta}(t) = 0$ at the initial time. As a result, all the time derivatives of the spatial expansion near the boundary also vanish.

	n \ k	0	1	2	3	4	5
Π	0	Π_0	Φ_1	$\frac{3}{2}\Pi_0^3-2\Pi_2$	$-\frac{8}{3}\Phi_1+3\Pi_0^2\Phi_1+2\Phi_3$	$-2\Pi_0^3+\frac{21}{4}\Pi_0^5+\frac{16}{3}\Pi_2$ $-6\Pi_0^2\Pi_2-8\Pi_4+3\Pi_0\Phi_1^2$	$\frac{32}{15}\Phi_1-8\Pi_0^2\Phi_1+\frac{57}{2}\Pi_0^4\Phi_1-6\Pi_0\Pi_2\Phi_1$ $+12\Phi_1^3+24f_3\Phi_2-16\Phi_3-12\Pi_0^2\Phi_3+24\Phi_5$
	1	0	0	0	0	0	
	2	Π_2	$\frac{4}{3}\Phi_1+\frac{3}{4}\Pi_0^2\Phi_1-\Phi_3$	$\Pi_0^3+\frac{3}{4}\Pi_0^5-\frac{8}{3}\Pi_2$ $-\frac{3}{2}\Pi_0^2\Pi_2+4\Pi_4+3\Pi_0\Phi_1^2$	$-\frac{16}{15}\Phi_1-2\Pi_0^2\Phi_1+\frac{51}{4}\Pi_0^4\Phi_1-24\Pi_0\Pi_2\Phi_1$ $-\frac{3}{2}\Phi_1^3-12f_3\Phi_2+8\Phi_3+\frac{21}{2}\Pi_0^2\Phi_3-12\Phi_5$		
	3	Π_3	$-2f_3\Phi_1+\frac{4}{3}\Phi_2+\frac{3}{2}\Pi_0^2\Phi_2-2\Phi_4$	$-4f_3\Pi_0-\frac{15}{2}f_3\Pi_0^3+14f_3\Pi_2-4\Pi_3$ $-9\Pi_0^2\Pi_3+10\Pi_5+8\Pi_0\Phi_1\Phi_2$			
	4	Π_4	$\frac{28}{45}\Phi_1-\frac{1}{4}\Pi_0^2\Phi_1+\frac{9}{32}\Pi_0^4\Phi_1-\frac{9}{4}\Pi_0\Pi_2\Phi_1$ $-\frac{9}{8}\Phi_1^3-3f_3\Phi_2+\frac{4}{3}\Phi_3+\frac{9}{4}\Pi_0^2\Phi_3-3\Phi_5$				
	5	Π_5					
Φ	0	0	0	0	0	0	0
	1	Φ_1	$\frac{3}{2}\Pi_0^3-2\Pi_2$	$-\frac{8}{3}\Phi_1+3\Pi_0^2\Phi_1+2\Phi_3$	$-2\Pi_0^3+\frac{21}{4}\Pi_0^5+\frac{16}{3}\Pi_2$ $-6\Pi_0^2\Pi_2-8\Pi_4+3\Pi_0\Phi_1^2$	$\frac{32}{15}\Phi_1-8\Pi_0^2\Phi_1+\frac{57}{2}\Pi_0^4\Phi_1-6\Pi_0\Pi_2\Phi_1$ $+12\Phi_1^3+24f_3\Phi_2-16\Phi_3-12\Pi_0^2\Phi_3+24\Phi_5$	
	2	Φ_2	$-3f_3\Pi_0-3\Pi_3$	$3f_3\Phi_1-4\Phi_2-\frac{3}{2}\Pi_0^2\Phi_2+6\Phi_4$	$12f_3\Pi_0+9f_3\Pi_0^3-36f_3\Pi_2+12\Pi_3$ $+18\Pi_0^2\Pi_3-30\Pi_5-15\Pi_0\Phi_1\Phi_2$		
	3	Φ_3	$\Pi_0^3+\frac{3}{8}\Pi_0^5-4\Pi_4-\frac{3}{2}\Pi_0\Phi_1^2$	$-\frac{112}{45}\Phi_1+4\Pi_0^2\Phi_1-\frac{15}{4}\Pi_0^4\Phi_1+15\Pi_0\Pi_2\Phi_1$ $+3\Phi_1^3+12f_3\Phi_2-\frac{16}{3}\Phi_3-9\Pi_0^2\Phi_3+12\Phi_5$			
	4	Φ_4	$-5f_3\Pi_2+\frac{9}{4}\Pi_0^2\Pi_3-5\Pi_5-\frac{3}{2}\Pi_0\Phi_1\Phi_2$				
	5	Φ_5					
f	0	1	0	0	0	0	0
	1	0	0	0	0	0	0
	2	$-\frac{1}{2}\Pi_0^2$	$-\Pi_0\Phi_1$	$-\frac{3}{2}\Pi_0^4+2\Pi_0\Pi_2-\Phi_1^2$	$\frac{8}{3}\Pi_0\Phi_1-\frac{15}{2}\Pi_0^3\Phi_1+6\Pi_2\Phi_1-2\Pi_0\Phi_3$	$2\Pi_0^4-12\Pi_0^6-\frac{16}{3}\Pi_0\Pi_2+24\Pi_0^3\Pi_2-12\Pi_2^2$ $+8\Pi_0\Pi_4+\frac{32}{3}\Phi_1^2-15\Pi_0^2\Phi_1^2-8\Phi_1\Phi_3$	
	3	f_3	$-\Pi_0\Phi_2$	$3f_3\Pi_0^2+3\Pi_0\Pi_3\Phi_1\Phi_2$	$3f_3\Pi_0\Phi_1+6\Pi_3\Phi_1+4\Pi_0\Phi_2$ $+2\Pi_2\Phi_2-6\Pi_0\Phi_4$		
	4	$-\frac{1}{3}\Pi_0^2-\frac{1}{4}\Pi_0^4+\Pi_0\Pi_2+\frac{1}{2}\Phi_1^2$	$\frac{2}{3}\Pi_0\Phi_1+\frac{5}{4}\Pi_0^3\Phi_1-\Pi_2\Phi_1-\Pi_0\Phi_3$	$\frac{3}{2}\Pi_0^6-\frac{4}{3}\Pi_0\Pi_2-4\Pi_0^3\Pi_2+2\Pi_2^2$ $+4\Pi_0\Pi_4-\frac{2}{3}\Phi_1^2+\frac{9}{2}\Pi_0^2\Phi_1^2$			
	5	$\frac{1}{4}f_3\Pi_0^2+\frac{1}{2}\Pi_0\Pi_3+\frac{1}{2}\Phi_1\Phi_2$	$-2f_3\Pi_0\Phi_1-\Pi_3\Phi_1+\frac{2}{3}\Pi_0\Phi_2$ $+\frac{5}{4}\Pi_0^3\Phi_2-\Pi_2\Phi_2-\Pi_0\Phi_4$				
	6	$-\frac{1}{45}\Pi_0^2-\frac{1}{24}\Pi_0^6-\frac{2}{9}\Pi_0\Pi_2+\frac{1}{6}\Pi_2^2$ $+\frac{1}{3}\Pi_0\Pi_4-\frac{1}{9}\Phi_1^2+\frac{1}{6}\Phi_2^2+\frac{1}{3}\Phi_1\Phi_3$					
δ	0	0	0	0	0	0	0
	1	0	0	0	0	0	0
	2	$\frac{1}{4}\Pi_0^2$	$\frac{1}{2}\Pi_0\Phi_1$	$\frac{3}{4}\Pi_0^4-\Pi_0\Pi_2+\frac{1}{2}\Phi_1^2$	$-\frac{4}{3}\Pi_0\Phi_1+\frac{15}{4}\Pi_0^3\Phi_1-3\Pi_2\Phi_1+\Pi_0\Phi_3$	$-\Pi_0^4+6\Pi_0^6+\frac{8}{3}\Pi_0\Pi_2-12\Pi_0^3\Pi_2+6\Pi_2^2$ $-4\Pi_0\Pi_4-\frac{16}{3}\Phi_1^2+\frac{15}{2}\Pi_0^2\Phi_1^2+4\Phi_1\Phi_3$	
	3	0	0	0	0		
	4	$-\frac{1}{12}\Pi_0^2+\frac{1}{4}\Pi_0\Pi_2+\frac{1}{8}\Phi_1^2$	$\frac{1}{6}\Pi_0\Phi_1+\frac{9}{16}\Pi_0^3\Phi_1-\frac{1}{4}\Pi_2\Phi_1-\frac{1}{4}\Pi_0\Phi_3$	$\frac{3}{4}\Pi_0^6-\frac{1}{3}\Pi_0\Pi_2-\frac{3}{2}\Pi_0^3\Pi_2+\frac{1}{2}\Pi_2^2$ $+\Pi_0\Pi_4-\frac{1}{6}\Phi_1^2+\frac{15}{8}\Pi_0^2\Phi_1^2$			
	5	$\frac{1}{5}\Pi_0\Pi_3+\frac{1}{5}\Phi_1\Phi_2$	$-f_3\Pi_0\Phi_1-\frac{2}{5}\Pi_3\Phi_1+\frac{4}{15}\Pi_0\Phi_2$ $+\frac{3}{5}\Pi_0^3\Phi_2-\frac{2}{5}\Pi_2\Phi_2-\frac{2}{5}\Pi_0\Phi_4$				
	6	$\frac{1}{90}\Pi_0^2-\frac{1}{9}\Pi_0\Pi_2+\frac{1}{12}\Pi_2^2+\frac{1}{6}\Pi_0\Pi_4$ $-\frac{1}{18}\Phi_1^2+\frac{1}{12}\Phi_2^2+\frac{1}{6}\Phi_1\Phi_3$					

Table 2.1: Coefficients of the expansion in powers of $\left(\frac{\pi}{2}-x\right)^n$ of time derivatives d^k/dt^k for a massless scalar field and the initial conditions $\Pi=\sum_{n\geq 0}\Pi_n\left(\frac{\pi}{2}-x\right)^n$, $\Phi=\sum_{n\geq 0}\Phi_n\left(\frac{\pi}{2}-x\right)^n$ and $d^3f/dx^3=-6f_3$. We work in the boundary time gauge $\delta\left(t,x=\frac{\pi}{2}\right)=0$ and set $8\pi G=1$.

2.1.3. Quenches and frequency modulation

In this section, we deal with the issue of how to introduce a non-zero boundary scalar field or driving starting from the AdS vacuum, while fulfilling the corner conditions presented in 2.1.2. As explained in that section, this must involve using a non-analytic function for which all time derivatives at $t = t_0$ must vanish.

We achieve this requirement using the function $\tanh\tau$, which ranges from -1 as $\tau \to -\infty$ to +1 as $\tau \to +\infty$, with all its derivatives vanishing in both limits. Taking this into account, we define the following *quench* function:

$$q_{\pm}\left(t,\beta,\sigma\right) = \frac{1}{2}\left(1 \pm \tanh\left(\sigma\,\beta\left(-\frac{1}{t-t_0} + \frac{1}{(t_0+\beta)-t}\right)\right)\right). \tag{2.19}$$

This function interpolates between 0 at $t = t_0$ and ± 1 at $t = t_0 + \beta$. At both points, all its time derivatives vanish.[1] The parameter σ controls the slope of this function. For amplitude modulations, we set $\sigma = 1/2$.

We will use this function to modulate the amplitude of the scalar field at the boundary as follows:

$$\phi(t, x = \pi/2) = \begin{cases} \rho_i f(t), & t < t_0, \\ \left[\rho_i + (\rho_f - \rho_i) q_+(t,\beta,\sigma)\right] f(t), & t_0 \le t \le t_0 + \beta, \\ \rho_f f(t), & t > t_0 + \beta, \end{cases} \tag{2.20}$$

which allows for a smooth interpolation between two amplitudes, ρ_i and ρ_f, of the driving. Since the time derivatives of $q_+(t,\beta,\sigma)$ vanish at $t = t_0$ and $t = t_0 + \beta$, the expression $q_+(t,\beta,\sigma)f(t)$ matches all the derivatives with $f(t)$ at both instants. By this method, the time derivatives of the scalar field at the boundary remain continuous at all times.

In particular, we will be interested in introducing time-dependent functions as drivings starting from the AdS vacuum at $t = 0$. In this case,

$$\phi(t, x = \pi/2) = \begin{cases} \rho_f q_+(t,\beta,\sigma) f(t), & t \le \beta, \\ \rho_f f(t), & t > \beta, \end{cases} \tag{2.21}$$

ensuring that all time derivatives of the driving vanish at $t = 0$. Therefore, the corner conditions at $t = t_0$ are satisfied.

We will also modulate the frequency of time-periodic drivings. The problem with using the previous expressions to modulate the frequency is that the instantaneous frequency of the function $\cos(q_{\pm}t)$ will be $d(q_{\pm}t)/dt = q_{\pm} + q'_{\pm}t$, causing the frequency to go up and down, resulting in undesirable behaviour. We will use instead the following expressions to implement a driving of

[1] Note that although the argument of $\tanh$ introduces additional factors when differentiating, the sech factor from the derivative of $\tanh$ ensures that all terms vanish.

amplitude $\rho_{\rm b}$ that modulates between the frequencies ω_1 at $t = t_0$ and ω_2 at $t = t_0 + \beta$:

$$\begin{aligned}\phi(t,\pi/2) &= \begin{cases}\rho_{\rm b}\cos(\omega_1 t), & t < t_0,\\ \rho_{\rm b}\cos\left(\nu(t)\right), & t_0 \le t \le t_0+\beta,\\ \rho_{\rm b}\cos(\omega_2 t+\delta_\nu), & t > t_0+\beta.\end{cases}\\ \nu\left(t\right) &= \left[\omega_1 + \left(\omega_2-\omega_1\right) q_+\left(t,\beta,\sigma\right)\right] t - \frac{\beta}{2}\left(\omega_2-\omega_1\right) q_+^2\left(t,\beta,\sigma\right),\\ \delta_\nu &= -\frac{\beta}{2}\left(\omega_2-\omega_1\right).\end{aligned} \tag{2.22}$$

With this definition, the instantaneous frequency $\omega(t) = d\nu(t)/dt$ exhibits a more suitable behaviour. We set $\sigma = 1/4$ in (2.22) simply because, qualitatively, it results in a well-shaped function, avoiding excessive steepness or other undesirable behaviours. An example of the profile of this function can be seen in Fig. 3.4(b).

2.1.4. Time-periodic boundary conditions

As said at the end of 2.1.1, there exist full non-linear oscillating solutions with Dirichlet boundary conditions $\phi(t, x = \pi/2) = 0$ [5], called oscillons through this thesis. In [10] this construction was extended to non-normalizable, i.e. sourced, *time-periodic solutions* (hereafter TPSs) with arbitrary frequencies $\omega_{\rm b} \in \mathbb{R}$. The boundary condition needed is $\phi_{\rm b}(t) \equiv \phi(t, x = \pi/2) = \rho_{\rm b}\cos(\omega_{\rm b} t)$, where $\omega_{\rm b}$ and $\rho_{\rm b}$ are the *driving frequency* and *amplitude* respectively.

One of the main results in [10] is the plot reproduced here in Fig. 2.1. Every point in the plot corresponds to a time-periodic solution (TPS) labelled according to $(\omega_{\rm b}, \rho_{\rm o} = \max_{t\in\text{period}}(\phi(t,0)))$, namely, the driving boundary frequency and the maximum amplitude of the scalar field oscillation at the origin (see Fig. 2.2).[2] Level curves correspond to fixed values of the driving amplitude $\rho_{\rm b}$. The holographic dictionary relates these solutions to some time-dependent state of a periodically-driven Hamiltonian whereby $\phi(t, x = \pi/2)$ is the coupling.

The normalizable non-linear oscillons with vanishing driving, $\phi_{\rm b} = 0$, span the black curved lines that hit vertically the horizontal axis at values of $\omega_{\rm b} = 2n + 3$. On either side, each point corresponds to a TPS with one more node of the $\phi(x)$ profile on the right than on the left. Hence, they correspond to Floquet quantum phase transitions. On both sides, there are regions of stable solutions as well as regions of unstable solutions. The stability analysis was performed in [10], where we refer the interested reader for further details.

Besides the explicit numerical construction of the time-symmetric solution, another building method can provide the same solutions by exploiting a holographic version of the adiabatic principle. Starting from the AdS vacuum, the periodic driving can be introduced by modulating the amplitude with a sigmoid-type function as the one described in 2.19, which slowly interpolates between zero and some finite value $(\omega_{\rm b}, 0) \to (\omega_{\rm b}, \rho_{\rm b})$. We label the time span of this quench as β. For slow enough ramping, $\beta \gg 1$, the system follows a sequence of TPSs until the final one is reached. We will call such a protocol an *adiabatic injection*. The opposite one,

[2] Notice that the oscillations $\phi(t, x)$ at any fixed value of x are not purely sinusoidal, just periodic.

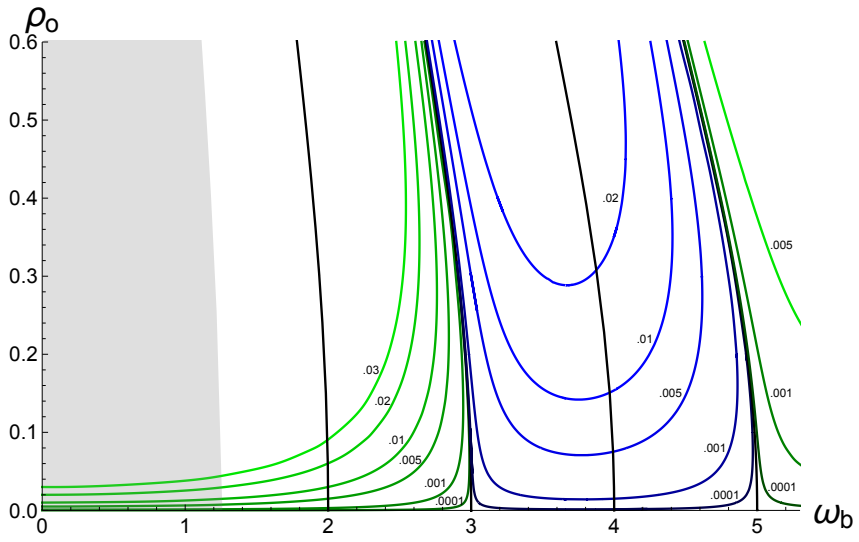

Figure 2.1: Level plot showing the time-periodic solutions (TPSs). The horizontal axis is for the driving frequency $\omega_{\rm b}$ and the vertical axis is for the maximum amplitude at the origin $\rho_{\rm o} \equiv \max_{t\in\text{period}} \phi(t,0)$. The level curves are labelled by the value of the driving maximum amplitude $\rho_{\rm b}$. The vertical black curves emerging from the frequencies $\omega_n = 2n+3$ with $n \geq 0$ correspond to oscillon solutions with vanishing driving amplitude, $\rho_{\rm b} = 0$. Aside from the results already obtained in the mentioned works, this plot also contains the following results obtained in this thesis in chapter 4. The lines emerging from $\omega_n = 2n+2$ with $n \geq 0$ are TPSs with (almost) vanishing v.e.v., $\langle \mathcal{O} \rangle \sim 0$. The shaded region to the left signals the domain of TPSs whose average mass is negative $\bar{M} < 0$.

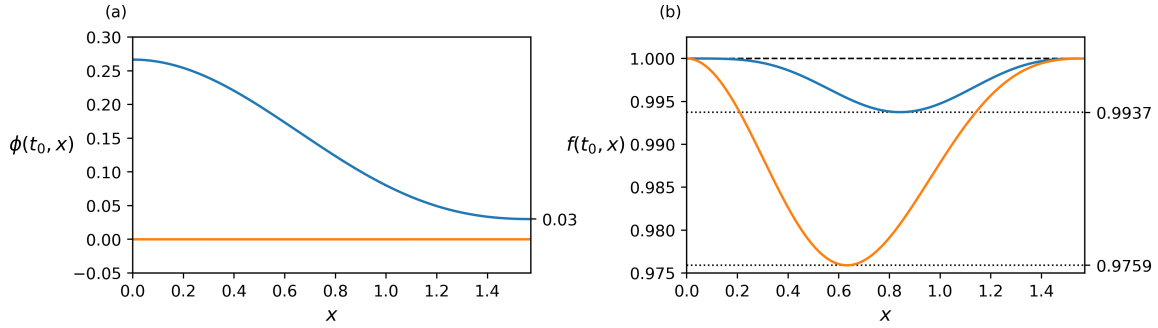

Figure 2.2: Time-periodic solution (TPS) with $\rho_{\rm b} = 0.03$ and $\omega_{\rm b} = 2.5$. The plots show two snapshots of the scalar field $\phi(t_0, x)$ (a) and the metric $f(t_0, x)$ (b) at two fixed times: one when the amplitude of the scalar field at the boundary reaches its maximum (blue) and another when it vanishes (orange). For this amplitude of the driving, the backreaction of the metric is very small, $f_{\rm min} = \min_{x\in(0,\pi/2)} f(t,x) = 0.9759$ and $1 - f_{\rm min} = 0.0241$.

where the driving is smoothly turned off at constant frequency, will be termed the *adiabatic extraction* protocol.

The TPSs thus constructed are tantamount to a so-called *Floquet condensate* in the dual quantum field theory. The adiabatic preparation of Floquet condensates is a topic of active research in the context of periodically-driven systems [54–56].

In Fig. 2.3 we show an example of the dynamical construction of a TPS starting from the AdS vacuum. The first plot, (a), represents the driving profile. It starts from AdS and slowly builds up a harmonic driving with amplitude $\rho_{\rm b} = 0.01$ and frequency $\omega_{\rm b} = 2.5$. The solid blue colour is an artefact of the dense packing of the oscillations, as can be seen from magnifying the small rectangle. The time span of the injection envelope is $\beta = 2000$.

In the remaining subplots, other relevant magnitudes have been monitored. Observe that they all oscillate periodically in time. Sometimes the period is halved. This happens for magnitudes that couple to $|\phi(t, \pi/2)|^2$, such as the metric function $f(t)$ and, hence, its minimum $f_{\rm min}(t)$ or the mass $M(t)$. As the amplitude is slowly increased, the system follows a succession of TPSs. In the magnified rectangles, the TPS that develops after the quench is displayed. The last plot, (f), is a numerical check of the fulfilment of the Ward Identity, meaning the difference

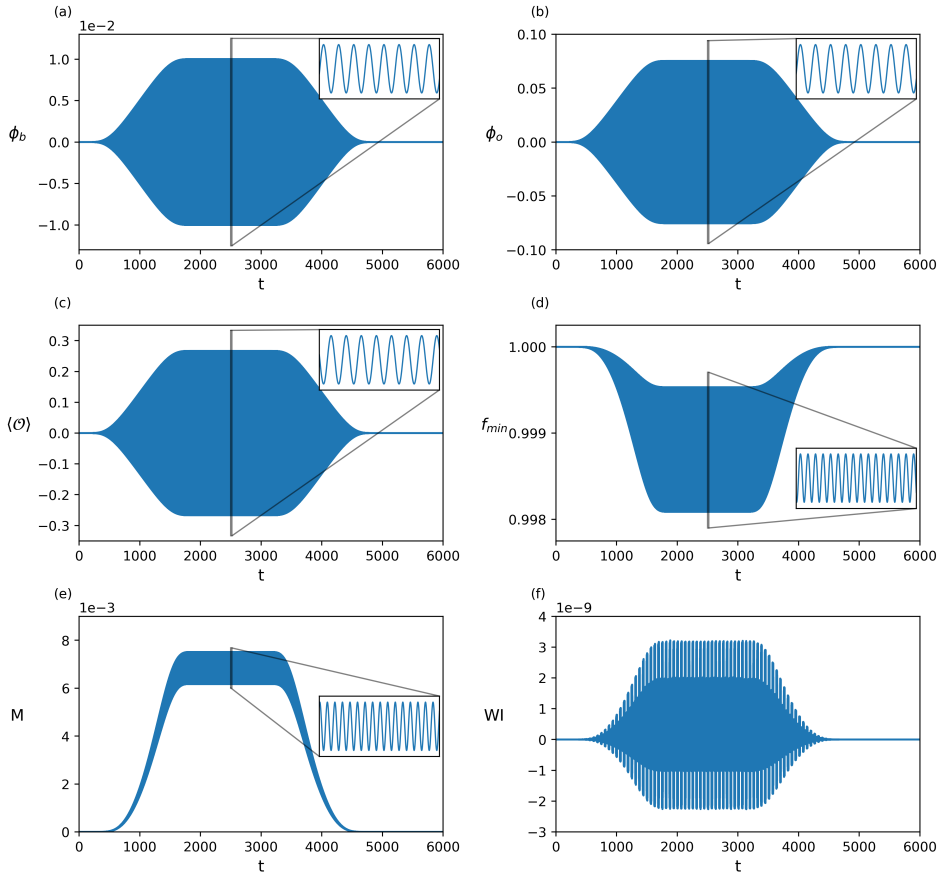

Figure 2.3: Driving protocol for the creation of a time-periodic solution (TPS) with $\omega_{\rm b} = 2.5$. (a) The driving amplitude rises adiabatically $\rho_{\rm b} : 0 \to 0.01$, and then smoothly turns off. (b) The scalar field at the origin $\phi_{\rm o}$, (c) the v.e.v. $\langle\mathcal{O}\rangle$, (d) the minimum value of the metric function and (e) the mass oscillate periodically, signalling that we have indeed constructed a TPS. (f) The Ward Identity (meaning the difference between the left-hand and right-hand sides in (2.10)) supports the simulation's accuracy. The metric, and therefore the mass, oscillates with double the frequency of the scalar field, to which it couples quadratically. By slowly turning off the source, we return adiabatically to the vacuum state, where $\phi_{\rm o} = \langle\mathcal{O}\rangle = M = 0$ and $f_{\rm min} = 1$.

between the left-hand and right-hand sides in (2.10). This is one of the consistency checks that we will perform to ensure that the numerical solutions are sound. The accuracy increases with the spatial grid resolution.

After the TPS has been built, the *adiabatic extraction protocol* smoothly follows the same sigmoid envelope but in reverse order. The end result is a graceful exit back into the vacuum AdS geometry. This smooth and reversible behaviour is generic as long as we keep away from the critical lines of oscillon solutions (see Fig. 2.1). There is where we expect, and indeed see, that the adiabaticity is lost, and a new phenomenon can be observed, as we will see in chapter 3.

Not only the amplitude but also the frequency of the driving, if changed slowly enough, can interpolate smoothly between any two stable TPSs $(\omega_{\rm b}, \rho_{\rm b}) \to (\omega'_{\rm b}, \rho'_{\rm b})$. This *frequency modulation* protocol allows for general paths to be traced in this parameter space. In chapter 3, we will see how things behave when these paths move close to or across critical lines of non-linear resonance using the modulation functions described in 2.1.3.

2.2. Massive scalar field and mixed boundary conditions

In this section, we will see that there are systems where it is possible to set mixed boundary conditions that do not correspond to either the standard or the alternative quantization of the dual CFT.

We start by considering Einstein gravity with a negative cosmological constant coupled to a massive scalar field ϕ with negative mass squared $m^2 < 0$. We have an asymptotically AdS$_{d+1}$ spacetime in global coordinates, where the boundary is located at $r \to \infty$ and the scalar field decays at large r as[3]

$$\phi = \frac{\alpha}{r^{\Delta_-}} + \frac{\beta}{r^{\Delta_+}}, \tag{2.23}$$

with

$$\Delta_\pm = \frac{d \pm \sqrt{d^2 + 4m^2}}{2}. \tag{2.24}$$

Standard quantization: $\alpha = 0$

Boundary conditions with $\alpha = 0$ correspond to the standard quantization of the dual CFT with a scalar operator $\langle \mathcal{O} \rangle \propto \beta$. For these conditions it is known that scalar fields with a mass satisfying $m_{\rm BF} \leq m^2 < 0$, where $m^2_{\rm BF} = -d^2/4$ is the Breitenlohner-Freedman bound [57,58], are stable in AdS spacetime.

Alternative quantization: $\beta = 0$

Furthermore, if the scalar field mass is in the range $m_{\rm BF} \leq m^2 < m_{\rm BF} + 1$, both solutions with Δ_- and Δ_+ in (2.23) are normalizable. In this case, it is possible to set $\beta = 0$ boundary

[3] For fields at $m^2 = m^2_{\rm BF} = -d^2/4$, for which $\Delta_+ = \Delta_-$, one of the solutions would fall off as $\ln r / r^{\Delta_+}$.

conditions, which means an alternative AdS-invariant quantization of the dual CFT, where the vacuum expectation value of the scalar operator $\langle \mathcal{O} \rangle \propto \alpha$.

When $\alpha \neq 0$, the standard fall-off of boundary conditions on the metric must be relaxed because the backreaction of the scalar field causes the metric to fall more slowly than in the standard quantization case. We will discuss AdS asymptotic symmetries and the asymptotic behaviour of the metric that preserves them in 2.2.3.

Mixed boundary conditions

In chapter 4, however, we will focus on boundary conditions that correspond neither to the standard quantization nor to the alternative one. It turns out that a scalar field with a mass squared in the range

$$m_{\mathrm{BF}} \leq m^2 < m_{\mathrm{BF}} + 1 \tag{2.25}$$

allows for mixed boundary conditions, also known in the literature as *designer gravity* [50, 59], of the form

$$\beta = \beta_{\mathrm{BC}}(\alpha), \tag{2.26}$$

where β_{BC} is an arbitrary function.

Remarkably, boundary conditions with $\beta = \alpha^{\Delta_+/\Delta_-}$ preserve AdS asymptotic symmetries, as we will see in 2.2.3.4. For other cases, AdS asymptotic symmetries are generally broken. However, these mixed boundary conditions are still invariant under global time translations, allowing for the definition of a conserved total energy.

2.2.1. Conserved total energy

We now calculate the conserved mass. We start by considering the Hamiltonian of the system, given by

$$H[\xi] = \int_{\Sigma} d^d x \xi^{\mu} \mathcal{H}_{\mu}(x) + Q_{\mathrm{grav}}[\xi] + Q_{\phi}[\xi], \tag{2.27}$$

where Σ is a spacelike surface, ξ^{μ} is an asymptotic Killing vector[4], $\mathcal{H}_{\mu}$ are the usual Hamiltonian and momentum constraints, and $Q_{\mathrm{grav}}[\xi]$, $Q_{\phi}[\xi]$ are surface terms, due to gravity and the scalar field respectively, such that the variation of the Hamiltonian is well defined. This last requirement defines the expressions for the variations of these terms, which must be [60]:

$$\delta Q_{\mathrm{grav}}[\xi] = \frac{1}{2} \oint dS_i G^{ijkl} \left(\xi^{\perp} D_j \delta g_{kl} - \delta g_{kl} D_j \xi^{\perp} \right) + 2 \oint dS_i \frac{\xi^j \delta \pi^i{}_j}{\sqrt{g}} - \oint dS_i \xi^i \frac{\pi^{jk} \delta g_{jk}}{\sqrt{g}}, \tag{2.28a}$$

$$\delta Q_{\phi}[\xi] = - \oint dS_i \delta \phi \left[D^i \phi \xi^{\perp} + \frac{p \xi^i}{\sqrt{g}} \right], \tag{2.28b}$$

where $G^{ijkl} = \frac{1}{2} g^{1/2} \left(g^{ik} g^{jl} + g^{il} g^{jk} - 2 g^{ij} g^{kl} \right)$, $\xi^{\perp} = \xi \cdot n$ with n the unit normal to Σ, D_j denotes the covariant derivative associated with the metric g_{ij}, and π^{ij}, p are the momenta

[4] We will discuss asymptotic Killing vectors in AdS in 2.2.3.

conjugate to g_{ij}, ϕ.

In chapter 4, we will focus on a model with $m^2 = -2$ in $d = 3$, so we will derive the conserved mass for this case. When $\alpha \neq 0$, the scalar field falls off more slowly than in the standard quantization, introducing an additional contribution to the surface terms, which emerges in the first term of (2.28b). If we introduce the asymptotic behaviour of the scalar field, which for $m^2 = -2$ and $d = 3$ is

$$\phi = \frac{\alpha}{r} + \frac{\beta}{r^2}, \tag{2.29}$$

then the mentioned term becomes

$$-\oint dS_i \delta\phi D^i \phi \xi^{\perp} = r \oint (\alpha\delta\alpha) d\Omega + \oint [\delta(\alpha\beta) + \beta\delta\alpha] d\Omega. \tag{2.30}$$

Putting all together, we can integrate to obtain the total charge:[5]

$$Q[\xi] = Q_{\text{grav}}[\xi] + r \oint \frac{\alpha^2}{2} d\Omega + \oint [\alpha\beta + W(\alpha)] d\Omega, \tag{2.31}$$

where

$$W(\alpha) \equiv \int_0^{\alpha} \beta(\tilde{\alpha}) d\tilde{\alpha}. \tag{2.32}$$

In (2.31), a surface term proportional to the radius appears, causing a divergence. However, this divergence is exactly cancelled by another one arising from the integration of the usual gravitational term (2.28a). For spherically symmetric solutions, the total mass is given by

$$M = 4\pi \left(m_{\text{grav}} + \alpha\beta + W \right), \tag{2.33}$$

where m_{grav} is the usual term coming from the gravity contribution, $m_{\text{grav}} \equiv \langle T_{tt} \rangle = \frac{3}{16\pi G} g^{\text{FG}}_{(3)tt}$ (see Eq. (2.9)). For the coordinates used in this thesis, (2.2a),

$$m_{\text{grav}} = -f_3 / 8\pi G, \tag{2.34}$$

where f_3 is the third coefficient in the near-boundary expansion (2.6c).

2.2.2. Multi-trace deformations of the dual CFT

Traditionally, there are two different AdS-invariant quantizations for the scalar field in the CFT. For the standard quantization, holography interprets β in (2.23) as the expectation value of a scalar operator $\mathcal{O}$ of dimension Δ_+ in the boundary CFT, while α is related to a source for $\mathcal{O}$. As we have seen, for a certain range of negative values of m^2, there is an alternative way to quantize the scalar field, where $\mathcal{O}$ is an operator of dimension Δ_-. In this alternative quantization α is identified with $\langle \mathcal{O} \rangle$, while β behaves as the source. Let us consider the standard quantization and propose to calculate the expectation value of $\exp\left(-N^2 \int d^n x f(x) \mathcal{O}\right)$ or the partition function

[5] The terms depending on $\pi^i j$ and p in (2.28) vanish because of the fall-off of the conjugate momenta.

of the boundary CFT when there is a perturbation in the Lagrangian given by [39, 40]

$$\mathcal{L} \to \mathcal{L} + N^2 \mathcal{W} \,, \quad \text{with } \mathcal{W} = \int d^n x f\left(x\right) \mathcal{O}. \tag{2.35}$$

To calculate this expectation value, the prescription in holography is to compute the AdS partition function with the boundary condition

$$\alpha = f. \tag{2.36}$$

As we have seen, β corresponds to the expectation value of the operator $\mathcal{O}$, so we can rewrite

$$\mathcal{W} = \int d^n x f\left(x\right) \beta, \tag{2.37}$$

and the boundary condition $\alpha = f$ becomes

$$\alpha = \frac{\delta \mathcal{W}}{\delta \beta}. \tag{2.38}$$

Usually, one considers trace operators

$$\mathcal{O} = \frac{1}{N} \mathrm{Tr} f\left(\Phi_i\right), \tag{2.39}$$

where f is an arbitrary function of the fields Φ_i defined without traces, so $\mathcal{O}_\alpha$ is a *single-trace operator*. Now the approach is to replace $\mathcal{W}$ by a non-linear functional $\mathcal{W}\left(x, \mathcal{O}, d\mathcal{O}, ...\right)$, replace $\mathcal{O}$ by β, and impose the boundary condition $\alpha = \frac{\delta \mathcal{W}}{\delta \beta}$ even if $\mathcal{W}$ is not a linear function [13].

For definiteness, we consider again $d = 4$ and $m^2 = -2$, where the field behaves as

$$\phi = \frac{\alpha}{r} + \frac{\beta}{r^2}. \tag{2.40}$$

The standard quantization implies the boundary condition $\alpha = 0$. In this case, the operator $\mathcal{O}$ has conformal dimension $\Delta = 2$ and $\langle \mathcal{O} \rangle \propto \beta$. On the other hand, the alternative quantization corresponds to the boundary condition $\beta = 0$, the operator $\mathcal{O}$ has conformal dimension $\Delta = 1$, and $\langle \mathcal{O} \rangle \propto \alpha$.

Alternatively, mixed boundary conditions correspond neither to the standard quantization nor to the alternative one. They are dual to a deformation of the original CFT, consisting of adding a term $\mathcal{W}(\mathcal{O})$ to the Lagrangian and replacing the operator $\mathcal{O}$ by β in it. For boundary conditions of the form

$$\beta = c\, \alpha^n, \tag{2.41}$$

we have

$$\alpha = \frac{\delta \mathcal{W}}{\delta \beta} = c^{-1/n} \beta^{1/n}, \tag{2.42}$$

and the corresponding deformation of the CFT is [50]

$$\mathcal{W} = \frac{c^{-1/n}}{1+\frac{1}{n}} \int d^3x \mathcal{O}^{1+1/n}. \tag{2.43}$$

As another option, one can start with the CFT in the alternative quantization, dual to $\beta = 0$. We consider the same boundary conditions (2.41) and define

$$\beta = \frac{\delta \mathcal{W}}{\delta \alpha} = n\alpha^n. \tag{2.44}$$

Now we must formally replace the operator $\mathcal{O}$ by α in the deformation, yielding

$$\mathcal{W} = \frac{c}{n+1} \int d^3x \mathcal{O}^{n+1}. \tag{2.45}$$

For $c \to \infty$, the boundary condition approaches the situation with $\alpha = 0$, defining a family of solutions between the two quantizations. In conclusion, we have obtained that these boundary conditions are dual to a *multi-trace deformation* of the original CFT.

2.2.3. AdS asymptotic symmetries

In this section, we discuss the concept of asymptotic symmetries in AdS [61, 62], and explore how the mixed boundary conditions affect them.

2.2.3.1. Asymptotic Killing vectors

Asymptotic symmetries correspond to diffeomorphisms that map the asymptotic conditions into themselves. The first step in their study consists of finding the asymptotic Killing vectors ξ^μ that preserve the asymptotic form of the metric. This requires solving the so-called asymptotic Killing equations,

$$\mathcal{L}_\xi g_{\mu\nu} = \mathcal{O}\left(h_{\mu\nu}\right), \tag{2.46}$$

where the right-hand side represents the allowed deviation of the metric $g_{\mu\nu}$ from the background metric $g_{0\mu\nu}$,

$$g_{\mu\nu} = g_{0\mu\nu} + h_{\mu\nu}. \tag{2.47}$$

Eq. (2.46) ensures that after acting on the background metric with the asymptotic Killing vectors, the resulting metric perturbations preserve the same asymptotic behaviour.

2.2.3.2. AdS vacuum

We firstly focus on AdS_4 in global coordinates as the background metric $g_{0\mu\nu}$,

$$ds_0^2 = -\left(1+\left(\frac{r}{l}\right)^2\right) dt^2 + \frac{1}{1+\left(\frac{r}{l}\right)^2} dr^2 + r^2 d\Omega^2. \tag{2.48}$$

The asymptotic behaviour of the metric $g_{\mu\nu}$ (and therefore also its allowed variation) is obtained by requiring that the boundary conditions remain invariant under the AdS group $\mathrm{O}(3,2)$.

To achieve this, we start with the Kerr-AdS metric [63], which is a solution of Einstein's equations with mass, angular momentum and a negative cosmological constant. We consider this metric as the model to which all isolated systems in AdS asymptotically approach at infinity. We are interested in a form of this metric that is manifestly asymptotically AdS and that expresses its deviation from the AdS background at leading order in $1/r$. This metric is given by (see Appendix B in [61])

$$\begin{aligned}
g_{tt} &= -\frac{r^2}{l^2} - 1 + \frac{2m}{r}\left(1 - \frac{a^2}{l^2}\sin^2\theta\right)^{-\frac{5}{2}} + \mathcal{O}\left(1/r^3\right), \\
g_{rr} &= \left(1 + \left(\frac{r}{l}\right)^2\right)^{-1} + \frac{2ml^4}{r^5}\left(1 - \frac{a^2}{l^2}\sin^2\theta\right)^{-\frac{3}{2}} + \mathcal{O}\left(1/r^7\right), \\
g_{\theta\theta} &= r^2 + \frac{2ma^4}{r^3}\left(1 - \frac{a^2}{l^2}\sin^2\theta\right)^{-\frac{7}{2}}\sin^2\theta\cos^2\theta + \mathcal{O}\left(1/r^5\right), \\
g_{\varphi\varphi} &= r^2\sin^2\theta + \frac{2ma^2\sin^4\theta}{r}\left(1 - \frac{a^2}{l^2}\sin^2\theta\right)^{-\frac{5}{2}} + \mathcal{O}\left(1/r^3\right), \\
g_{t\varphi} &= -\frac{2am\sin^2\theta}{r}\left(1 - \frac{a^2}{l^2}\sin^2\theta\right)^{-\frac{5}{2}} + \mathcal{O}\left(1/r^3\right), \\
g_{r\theta} &= -\frac{2ml^2a^2}{r^4}\left(1 - \frac{a^2}{l^2}\sin^2\theta\right)^{-\frac{5}{2}}\sin\theta\cos\theta + \mathcal{O}\left(1/r^6\right), \\
g_{tr} &= g_{t\theta} = g_{r\varphi} = g_{\theta\varphi} = 0,
\end{aligned} \tag{2.49}$$

where m and a are the mass and the angular momentum per unit mass, respectively. We then act on this metric with the $\mathrm{O}(3,2)$ group in all possible ways. The perturbations generated by this procedure determine the allowed variation of the metric in (2.47) as

$$\begin{aligned}
&h_{tt} = h_{t\theta} = h_{t\varphi} = h_{\theta\theta} = h_{\theta\varphi} = h_{\varphi\varphi} = \mathcal{O}\left(1/r^1\right), \\
&h_{tr} = h_{r\theta} = h_{r\varphi} = \mathcal{O}\left(1/r^4\right), \quad h_{rr} = \mathcal{O}\left(1/r^5\right).
\end{aligned} \tag{2.50}$$

These perturbations define the order $\mathcal{O}(h_{\mu\nu})$ that must be introduced in the right-hand side of (2.46).

Solving the asymptotic Killing equations (2.46), we find the components for the asymptotic Killing vectors:

$$\xi^t = T_0(t,\theta,\varphi) + \frac{T_2(t,\theta,\varphi)}{r^2} + \frac{T_4(t,\theta,\varphi)}{r^4} + \mathcal{O}\left(1/r^5\right), \tag{2.51a}$$

$$\xi^r = rR_{+1}(t,\theta,\varphi) + \frac{R_1(t,\theta,\varphi)}{r} + \mathcal{O}\left(1/r^2\right), \tag{2.51b}$$

$$\xi^\theta = \Theta_0(t,\theta,\varphi) + \frac{\Theta_2(t,\theta,\varphi)}{r^2} + \frac{\Theta_4(t,\theta,\varphi)}{r^4} + \mathcal{O}\left(1/r^5\right), \tag{2.51c}$$

$$\xi^\varphi = \varphi_0(t,\theta,\varphi) + \frac{\varphi_2(t,\theta,\varphi)}{r^2} + \frac{\varphi_4(t,\theta,\varphi)}{r^4} + \mathcal{O}\left(1/r^5\right), \tag{2.51d}$$

where the functions $T_n(t,\theta,\varphi)$, $R_n(t,\theta,\varphi)$, $\Theta_n(t,\theta,\varphi)$ and $\Phi_n(t,\theta,\varphi)$ are determined by the following constraint equations:

$$\begin{aligned}
\partial_t T_0 &= \partial_\theta \Theta_0 = -R_{+1}, & T_4 &= \frac{3l^6}{8}\partial_t R_{+1},\\
\partial_\varphi \varphi_0 &= -R_{+1} - \cot\theta \Theta_0, & \Theta_4 &= -\frac{l^4}{8}\partial_\theta R_{+1},\\
\partial_\theta T_0 &= l^2 \partial_t \Theta_0 = l^2 \partial_t \partial_\theta R_{+1}, & \varphi_4 &= -\frac{l^4}{8\sin^2\theta}\partial_\varphi R_{+1},\\
\partial_\varphi T_0 &= l^2 \sin^2\theta \partial_t \varphi_0 = l^2 \partial_t \partial_\varphi R_{+1}, & R_1 &= \frac{l^2}{2} R_{+1},\\
\partial_\varphi \Theta_0 &= -\sin^2\theta \partial_\theta \varphi_0, & l^2 \partial_t \partial_t R_{+1} &= -R_{+1},\\
T_2 &= -\frac{l^4}{2}\partial_t R_{+1}, & \partial_\theta \partial_\theta R_{+1} &= -R_{+1},\\
\Theta_2 &= \frac{l^2}{2}\partial_\theta R_{+1}, & \partial_\theta \partial_\varphi R_{+1} &= \cot\theta \partial_\varphi R_{+1},\\
\varphi_2 &= \frac{l^2}{2\sin^2\theta}\partial_\varphi R_{+1}, & \partial_\varphi \partial_\varphi R_{+1} &= -\sin^2\theta\, R_{+1} - \sin\theta\cos\theta\, \partial_\theta R_{+1}.
\end{aligned} \tag{2.52}$$

These equations can be solved to obtain the asymptotic form of the Killing vectors in AdS_4. The complete expressions of the Killing vectors can be found in Appendix A. The asymptotic expansions of (A.1) in the radial coordinate match the asymptotic Killing vectors given by the components $(\xi^t, \xi^r, \xi^\theta, \xi^\varphi)$ in (2.51) with the constraints in (2.52).

These Killing vectors K_{ab} obey the algebra of $\mathcal{O}(3,2)$ [61],

$$[K_{ab}, K_{cd}] = A_{abcd}{}^{ef} K_{ef}, \tag{2.53}$$

where

$$A_{abcd}{}^{ef} = \frac{1}{2}\eta_{bc}\left(\delta_a{}^e \delta_d{}^f - \delta_a{}^f \delta_d{}^e\right) - \frac{1}{2}\eta_{bd}\left(\delta_a{}^e \delta_c{}^f - \delta_a{}^f \delta_c{}^e\right) - (a \leftrightarrow b) \tag{2.54}$$

and $\eta = (-1,+1,+1,+1,-1)$.

2.2.3.3. Scalar field

If we now introduce a scalar field with $m^2 = -2$ that decays as

$$\phi(t,r,\theta,\varphi) = \frac{\alpha(t,\theta,\varphi)}{r} + \frac{\beta(t,\theta,\varphi)}{r^2} + ..., \tag{2.55}$$

the asymptotic behaviour of the metric with the allowed variation is

$$\begin{aligned}
g_{tt} &= -\frac{r^2}{l^2} - 1 + \mathcal{O}(1/r), & g_{rr} &= \frac{l^2}{r^2} - \frac{l^4}{r^4} - \frac{l^2 8\pi G\alpha^2}{2r^4} + \mathcal{O}\left(1/r^5\right),\\
g_{\theta\theta} &= r^2 + \mathcal{O}(1/r), & g_{\varphi\varphi} &= r^2\sin^2\theta + \mathcal{O}(1/r),\\
g_{t\theta} &= g_{t\varphi} = g_{\theta\varphi} = \mathcal{O}(1/r), & g_{tr} &= g_{r\theta} = g_{r\varphi} = \mathcal{O}\left(1/r^2\right).
\end{aligned} \tag{2.56}$$

Solving the asymptotic Killing equations for this metric with the order of the allowed pertur-

bations specified in (2.56) as the right-hand side in (2.47), we obtain the following asymptotic Killing vectors:

$$\xi^t = T_0(t,\theta,\varphi) + \frac{T_2(t,\theta,\varphi)}{r^2} + \mathcal{O}\left(1/r^3\right), \tag{2.57a}$$

$$\xi^r = rR_{+1}(t,\theta,\varphi) + \frac{R_1(t,\theta,\varphi)}{r} + \mathcal{O}\left(1/r^2\right), \tag{2.57b}$$

$$\xi^\theta = \Theta_0(t,\theta,\varphi) + \frac{\Theta_2(t,\theta,\varphi)}{r^2} + \mathcal{O}\left(1/r^3\right), \tag{2.57c}$$

$$\xi^\varphi = \varphi_0(t,\theta,\varphi) + \frac{\varphi_2(t,\theta,\varphi)}{r^2} + \mathcal{O}\left(1/r^3\right), \tag{2.57d}$$

where the functions $T_n(t,\theta,\varphi)$, $R_n(t,\theta,\varphi)$, $\Theta_n(t,\theta,\varphi)$ and $\Phi_n(t,\theta,\varphi)$ are determined by the following constraint equations:

$$\begin{aligned}
&\partial_t T_0 = \partial_\theta \Theta_0 = -R_{+1}, && \varphi_2 = \frac{l^2}{2\sin^2\theta}\partial_\varphi R_{+1},\\
&\partial_\varphi \varphi_0 = -R_{+1} - \cot\theta\Theta_0, && R_1 = \frac{l^2}{2}\left(1+\frac{\kappa^2}{2l^2}\alpha\right)R_{+1} - \frac{\kappa^2}{8}\xi_0^m\partial_m\alpha,\\
&\partial_\theta T_0 = l^2\partial_t\Theta_0 = l^2\partial_t\partial_\theta R_{+1}, && l^2\partial_t\partial_t R_{+1} = \left(-1+\frac{\kappa^2}{2l^2}\alpha\right)R_{+1} - \frac{\kappa^2}{4l^2}\xi_0^m\partial_m\alpha,\\
&\partial_\varphi T_0 = l^2\sin^2\theta\partial_t\varphi_0 = l^2\partial_t\partial_\varphi R_{+1}, && \partial_\theta\partial_\theta R_{+1} = -\left(1+\frac{\kappa^2}{2l^2}\alpha\right)R_{+1} + \frac{\kappa^2}{4l^2}\xi_0^m\partial_m\alpha,\\
&\partial_\varphi\Theta_0 = -\sin^2\theta\partial_\theta\varphi_0, && \partial_\theta\partial_\varphi R_{+1} = \cot\theta\partial_\varphi R_{+1},\\
&T_2 = -\frac{l^4}{2}\partial_t R_{+1}, &&\\
&\Theta_2 = \frac{l^2}{2}\partial_\theta R_{+1}, &&
\end{aligned} \tag{2.58}$$

$$\partial_\varphi\partial_\varphi R_{+1} = -\left(1+\frac{\kappa^2}{2l^2}\alpha\right)\sin^2\theta\, R_{+1} - \sin\theta\cos\theta\,\partial_\theta R_{+1} + \frac{\kappa^2}{4l^2}\sin^2\theta\,\xi_0^m\partial_m\alpha.$$

2.2.3.4. Asymptotic symmetries in mixed boundary conditions

Our main interest in the asymptotic symmetries is to know their influence in the mixed boundary conditions. The transformation of a scalar field with the action of an asymptotic Killing vector is the following:

$$\phi \to \phi + \mathcal{L}_\xi\phi = \phi + \xi^\mu\partial_\mu\phi. \tag{2.59}$$

Using the asymptotic behaviour of the Killing vectors (2.51), this transformation yields

$$\phi \to \phi + rR_{+1}\partial_r\phi + \xi_0^m\partial_m\phi + ..., \tag{2.60}$$

where $m = t,\theta,\varphi$ and $\xi_0^m = T_0, \Theta_0, \Phi_0$. Considering a scalar field that decays as

$$\phi = \frac{\alpha}{r^{\Delta_-}} + \frac{\beta}{r^{\Delta_+}}, \tag{2.61}$$

we obtain the following transformation for α and β:

$$\alpha \to \alpha - R_{+1}\Delta_{-}\alpha + \xi_0^m \partial_m \alpha, \tag{2.62a}$$
$$\beta \to \beta - R_{+1}\Delta_{+}\beta + \xi_0^m \partial_m \beta. \tag{2.62b}$$

As we have seen, mixed boundary conditions define β as a function of α, $\beta = \beta_{\mathrm{BC}}(\alpha)$. Compatibility of this relation with the transformation of α and β in (2.62) requires that

$$\beta + \left(-R_{+1}\Delta_{+}\beta + \xi_0^m \partial_m \beta\right) d\lambda + \mathcal{O}\left(d\lambda^2\right) = \beta_{\mathrm{BC}}\left(\alpha + \left[-R_{+1}\Delta_{-}\alpha + \xi_0^m \partial_m \alpha\right] d\lambda\right),$$

$$\beta + \left(-R_{+1}\Delta_{+}\beta + \xi_0^m \partial_m \beta\right) d\lambda = \beta + \frac{\partial \beta}{\partial \alpha}\left(-R_{+1}\Delta_{-}\alpha + \xi_0^m \partial_m \alpha\right) d\lambda$$
$$\Rightarrow R_{+1}\left(\Delta_{-}\alpha \frac{\partial \beta}{\partial \alpha} - \Delta_{+}\beta\right) + \xi_0^m \left(\partial_m \beta - \partial_m \alpha \frac{\partial \beta}{\partial \alpha}\right) = 0. \tag{2.63}$$

As we are considering that β is only a function of α, the second parenthesis in (2.63) vanishes. Therefore, if $R_{+1} \neq 0$, the following relation must be satisfied:

$$\beta = c\, \alpha^{\frac{\Delta_{+}}{\Delta_{-}}}. \tag{2.64}$$

For the case with $d = 3$ and $m^2 = -2$ in which we will focus on chapter 4, $\Delta_{+} = 2$ and $\Delta_{-} = 1$. Then, the mixed boundary conditions $\beta = \beta_{\mathrm{BC}}(\alpha)$ that preserve all AdS asymptotic symmetries must have the following form:

$$\beta = c\, \alpha^2. \tag{2.65}$$

An important observation is that, for the Killing vector $(1, 0, 0, 0)$, we have $R_{+1} = 0$ in (2.51), and therefore the relation (2.64) is not required to preserve invariance under time translations. Therefore, it is still possible to define a conserved mass with mixed boundary conditions, as we did in 2.2.1.

In summary, in our previous language, only marginal deformations are guaranteed to keep the asymptotically AdS symmetry intact. Other types of deformations will generally break them. We will investigate a correlation between this symmetry breaking and the preservation or removal of the corner of instability.

2.2.4. Linearized theory: normal modes

To conclude this section on mixed boundary conditions, we will obtain the spectrum of linearized normal modes for a model that admits this type of boundary condition. We focus on the model we will work with in section 4, which consists of a four-dimensional system of Einstein gravity with a negative cosmological constant and a massive scalar field with the potential

$$V(\phi) = -4 \sinh^2\left(\frac{\phi}{2}\right) \tag{2.66}$$

in the action 2.1. This model arises as a consistent truncation of eleven-dimensional supergravity on $\text{AdS}_4 \times S^7/Z_k$, and has a dual interpretation as a particular sector of ABJM theory [64,65].

The scalar field has a negative squared mass $m^2 = -2$, which belongs to the range (2.25) where mixed boundary conditions are possible, and behaves asymptotically as

$$\phi = \frac{\alpha}{r} + \frac{\beta}{r^2} + \dots \tag{2.67}$$

To compute the normal modes, we put forward the following power series ansatz for the geometry,

$$\phi(t,x) = \sum_{n=1}^{\infty} \phi_n(t,x)\gamma^n, \tag{2.68a}$$

$$f(t,x) = 1 + \sum_{n=1}^{\infty} f_n(t,x)\gamma^n, \tag{2.68b}$$

$$\delta(t,x) = \sum_{n=1}^{\infty} \delta_n(t,x)\gamma^n, \tag{2.68c}$$

and solve the equations of motion at leading order in $\gamma \to 0$. Assuming that the boundary condition takes the form $\beta = c\,\alpha^n$ (as given in Eq. (2.41)), and that $c = O(1)$ while $\alpha = O(\gamma)$ in the $\gamma \to 0$ limit, it follows that $\beta = o(\gamma)$ for marginal and irrelevant deformations, whereas $\beta = O(\gamma)$ for relevant double-trace deformations.

The equation of motion for ϕ_1 is

$$-\ddot{\phi}_1 + \phi_1'' + 2\sec x \csc x \phi_1' + 2\sec^2 x \phi_1 = 0, \tag{2.69}$$

where dots (primes) denote temporal (spatial) derivatives. This equation allows for plane-wave solutions of the form

$$\phi_1(t,x) = \frac{A\sin(\omega x) + B\cos(\omega x)}{\tan x}\cos\omega t. \tag{2.70}$$

Regularity of $\phi(t,x)$ at $x = 0$ requires that $B = 0$. On the other hand, given Eq. (2.70), the series expansion of ϕ near the asymptotic boundary up to $O(\gamma)$ reads ($y \equiv \frac{\pi}{2} - x$)

$$\gamma\left[A\sin\left(\frac{\pi}{2}\omega\right) y - A\,\omega\cos\left(\frac{\pi}{2}\omega\right) y^2 + O(y^3)\right], \tag{2.71}$$

and has to match the general expression (2.67),

$$\alpha y + \beta y^2 + \mathcal{O}(y^3), \tag{2.72}$$

resulting in

$$\alpha = \gamma A \sin\left(\frac{\pi}{2}\omega\right) + O(\gamma^2), \tag{2.73a}$$

$$\beta = -\gamma A\,\omega\cos\left(\frac{\pi}{2}\omega\right) + O(\gamma^2). \tag{2.73b}$$

For non-relevant deformations, $\beta = o(\gamma)$, and hence the normal mode eigenfrequencies $\{\omega_n, n \in \mathbb{N}\}$ are the roots of $\cos\left(\frac{\pi}{2}\omega\right) = 0$,

$$\omega_n = 2n - 1, \ n \in \mathbb{N}. \tag{2.74}$$

This is the same eigenfrequency spectrum as in the alternative quantization, and it is exactly resonant. In contrast, for relevant double-trace deformations, $\beta = c_2\alpha$, the normal mode eigenfrequencies are the roots of a transcendental equation

$$\frac{c_2\pi}{2}\text{sinc}\left(\frac{\pi}{2}\omega\right) + \cos\left(\frac{\pi}{2}\omega\right) = 0. \tag{2.75}$$

In the absence of the double-trace deformation, $c_2 = 0$, we recover the normal mode eigenfrequency spectrum of the alternative quantization, Eq. (2.74). In the opposite, $c_2 \to \infty$ limit, we recover the normal mode eigenfrequency spectrum of the standard quantization,

$$\omega_n = 2n, \ n \in \mathbb{N}. \tag{2.76}$$

Analytical control over the full eigenfrequency spectrum can be gained by solving Eq. (2.75) in a perturbative expansion in $c_2 \to 0$. We find

$$\omega_n = \omega_n^{(0)} + \frac{2}{\pi\omega_n^{(0)}}c_2 - \frac{4}{\pi^2{\omega_n^{(0)}}^3}c_2^2 + O(c_2^3), \tag{2.77}$$

where $\omega_n^{(0)} = 2n-1, \ n \in \mathbb{N}$ is the alternative quantization eigenfrequency spectrum. Assuming that the $c_2 \to 0$ and $n \to \infty$ limits commute, the expression above results in

$$\omega_{n+1} - \omega_n = 2 - \frac{c_2}{\pi n^2} + O\left(\frac{1}{n^4}\right) \tag{2.78}$$

and implies that the eigenfrequency spectrum is not exactly resonant, but only asymptotically so. This assumption can be verified by an explicit numerical computation. Note that both for oscillons and boson stars in global AdS_4 the difference between two consecutive eigenfrequencies is $O\left(\frac{1}{n}\right)$ at large n [6, 8], while here it is $O\left(\frac{1}{n^2}\right)$.

Finally, we note that in the $c_2 \to -\frac{2}{\pi}$ limit the system supports a zero mode, as can be immediately seen by expanding Eq. (2.75) around $\omega = 0$. The existence of the zero mode allows for an analytical description of the lowest-lying eigenfrequency in the vicinity of $c_2 = -\frac{2}{\pi}$,

$$\begin{aligned}\omega_1 = \left(\frac{6}{\pi}\right)^{\frac{1}{2}}\left(c_2 + \frac{2}{\pi}\right)^{\frac{1}{2}}\Bigg[1 - \frac{\pi}{20}\left(c_2 + \frac{2}{\pi}\right) + \\ \frac{9\pi^2}{5600}\left(c_2 + \frac{2}{\pi}\right)^2 + \dots\Bigg].\end{aligned} \tag{2.79}$$

Note that, for $c_2 < -\frac{2}{\pi}$, $\omega_1 = i\lambda$ with $\lambda \in \mathbb{R}$ and the system becomes linearly unstable.

Away from the limits $c_2 \to 0$, $c_2 \to \infty$ and $n \to \infty$, the full eigenfrequency spectrum has to be determined numerically. The reader can find the first three eigenfrequencies as a function of c_2 in Fig. 2.4, where the linear instability kicking in at $c_2 = -\frac{2}{\pi}$ is clearly visible.

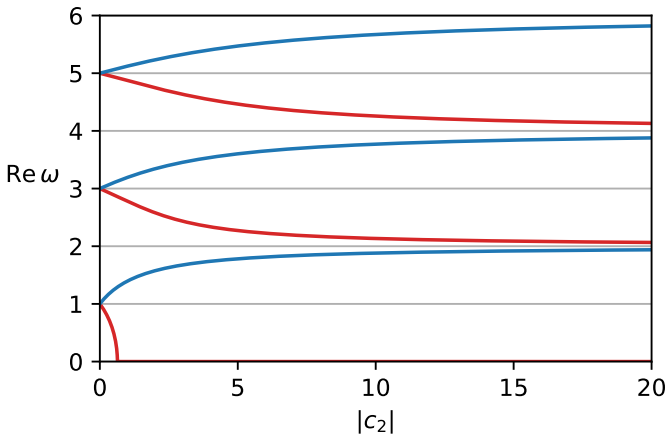

Figure 2.4: Eigenfrequencies for double-trace deformations as a function of c_2. Blue (red) curves correspond to positive (negative) values of c_2. For $c_2 \to 0$ ($c_2 \to \infty$), we recover the alternative (standard) quantization frequencies. At $c_2 = -2/\pi$, the first eigenfrequency vanishes. For lower values of c_2, this eigenfrequency is purely imaginary, signalling a linear instability.

2.3. Summary

In this chapter, we have introduced the model that will be used throughout the following chapters: Einstein gravity minimally coupled to a scalar field in AdS_4. We have seen that different scalar field masses allow for different types of boundary conditions.

In the first model, with a massless scalar field, two types of linearized normal modes arise: normalizable solutions corresponding to vanishing sources, and non-normalizable solutions corresponding to configurations with no v.e.v. We have discussed important aspects such as the corner conditions required for a well-posed initial-boundary value problem, and the specific functions employed to perform amplitude and frequency modulations while satisfying these conditions. Additionally, we have reviewed the extension of oscillon solutions to non-normalizable, sourced, time-periodic solutions (TPSs).

In contrast, for a massive scalar field, mixed boundary conditions are allowed, which do not correspond to either the standard or alternative quantization. We have related these boundary conditions to multi-trace deformations in the dual CFT. Finally, we introduced the concept of AdS asymptotic symmetries and showed that only marginal deformations preserve them.

In the following chapters, we will investigate various aspects of the AdS instability using these models.

Chapter 3

Probing the system by periodic driving at resonance

This chapter presents the results derived from a study on the dynamics of a real massless scalar field under time-periodic driving in a global anti-de Sitter spacetime in four dimensions (AdS_4), which corresponds to the system described in section 2.1. The research explores the scalar field's response to resonant and near-resonant drivings and investigates the formation and stability of time-periodic solutions. These results provide insight into the general picture of the system studied in [10], and aim to deepen our understanding of its dynamics near the resonance frequencies.

The work in this chapter proceeds by exploring protocols that allow a driving to be switched on and off adiabatically, as well as protocols that perform frequency modulation in order to traverse the resonance frequencies of the linearized system (see 2.1.1). To accomplish these modulations adiabatically and fulfil corner conditions (see section 2.1.2), the amplitude and frequency modulations are performed by implementing the functions described in 2.1.3. The outcomes of these simulations are analysed in terms of the spectral composition of the solutions, the cascading effects, and their stability. In Appendix D, tests that exhibit fourth-order convergence are provided, supporting the validity of the simulations presented in this chapter.

3.1. Single-frequency driving

In this first section, we investigate the system's response to a periodic driving at a single frequency. First, we inject and extract the driving at a resonant frequency of the linear system, i.e. $\omega_n = 2n + 1$ with $n \geq 0$. In the next protocol, we apply a frequency-modulated driving and analyse the system's behaviour when the resonant frequencies are traversed, either in one direction or the other. We also examine the system near the frequencies corresponding to the other solutions of the linearized equations of motion, those modes with vanishing v.e.v. and frequencies $\omega_n = 2n + 2$ with $n \geq 0$. Finally, we identify a region at low driving frequencies where TPSs with negative mass emerge.

We note here that as the energy density of the dual theory is $\langle T_{tt} \rangle \propto f_3$ (Eq. (2.9)), with f_3

being the coefficient of $(x - \pi/2)^3$ in the expansion of f (Eq. (2.6c)), our convention when referring to the mass M in the plots throughout this chapter will be

$$M \equiv f_3. \tag{3.1}$$

3.1.1. Creating oscillons driving at the resonance frequency

Probe Approximation on a Static AdS Background

Initially, we consider the scalar field response in a probe approximation, where the field evolves on a static AdS background. Under these conditions, with the gravitational backreaction neglected, the governing equations are linear. Here, the driving process leads to a monotonic increase in the amplitude over time, as shown in Fig. 3.1. Even for a small driving amplitude, $\rho_{\rm b} = 0.001$, the oscillation amplitude grows linearly with time. This effect illustrates the standard resonance behaviour for linear systems, characterized by continuous energy absorption from the driving source.

Backreaction and Non-linear Effects

When the gravitational backreaction is activated, the dynamics change markedly from the linear approximation. As shown in Fig. 3.2, the amplitude of the oscillation no longer grows unboundedly but instead saturates, manifesting an intense modulation pattern typical of interference between two close frequencies. A Fourier analysis reveals that the scalar field oscillates primarily at two frequencies: the driving frequency $\omega = \omega_{\rm b} = 3$, and a slightly lower frequency. This second frequency moves progressively further from the driving frequency as the amplitude of the driving increases.

At $t = 3000$ (equivalent to approximately 1500 oscillations in terms of the driving period, $T = 2\pi/\omega$), the driving is slowly turned off. Contrary to the return to AdS observed with a driving at a non-resonant frequency (see section 2.1.4), the system now leaves a remnant non-linear oscillon with a finite mass and no source.

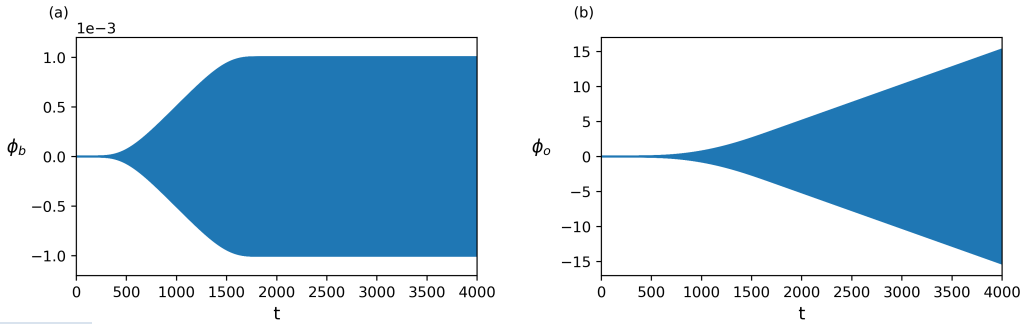

Figure 3.1: (a) Resonant driving at $\omega_{\rm b} = 3$ on a static AdS background. (b) The linear response shows monotonic energy absorption due to the resonance.

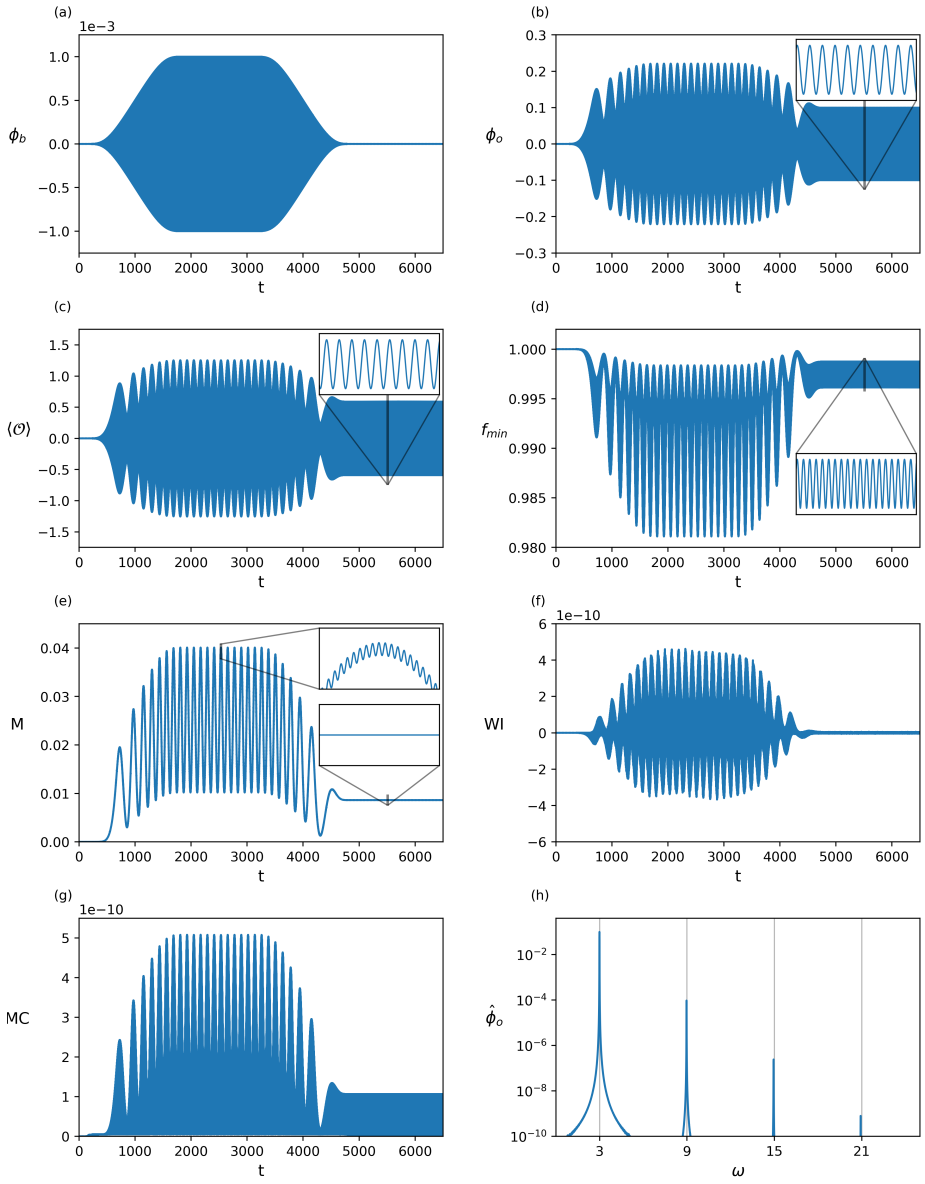

Figure 3.2: (a) Resonant driving at $\omega_{\rm b} = 3$ excites a nearby frequency, leading to interference and amplitude modulation. (b-d) The interference pattern produces amplitude saturation and mass (Eq. (3.1)) gain (e). Simulation accuracy is confirmed by the Ward Identity (f) (meaning the difference between the left-hand and right-hand sides in (2.10)), and by integrated Momentum Constraint (g) (i.e. the spatially integrated absolute value of the difference between the left-hand and right-hand sides in (2.5)). The final state, after the driving is switched off, is a sourceless TPS with spectral content shown in (h). This is an oscillon with a tower of frequencies, $\omega_{\rm osc}(2k+1)$ with $k \geq 0$, above the fundamental $\omega_{\rm osc} = 2.99$.

Fourier analysis of this remnant oscillon (Fig. 3.2(h)) reveals a spectral structure composed of a tower of frequencies: $\omega_k = \omega_{\rm osc}(2k+1)$, with $\omega_{\rm osc} = 2.99$ and $k \geq 0$. The fundamental frequency $\omega_{\rm osc}$ is the most prominent, while the amplitudes of the higher harmonics decrease rapidly.[1] The system thus settles into a stable, periodic state with period $T = 2\pi/\omega_{\rm osc}$.

The properties of the final oscillon depend on the specific parameters of the driving process, particularly the amplitude reached by the driving $\rho_{\rm b}$ and the adiabatic extraction speed β, as well as on the starting time at which the extraction is performed. For a given maximum amplitude of the driving, the maximum possible mass of the remnant oscillon decreases as the extraction becomes slower. As shown in Fig. 3.3, the final oscillon approaches a zero-mass state in the limit $\beta \to \infty$, i.e. the system returns to AdS vacuum as it does in the case of a non-resonant driving.

This dependence on quench speed highlights a breakdown of adiabaticity at resonance, in contrast to the behaviour observed in Fig. 2.3. While a non-resonant system returns to the vacuum state, driving the system at a resonant frequency disrupts this adiabatic behaviour, causing it to retain oscillatory states after finite-time quenches.

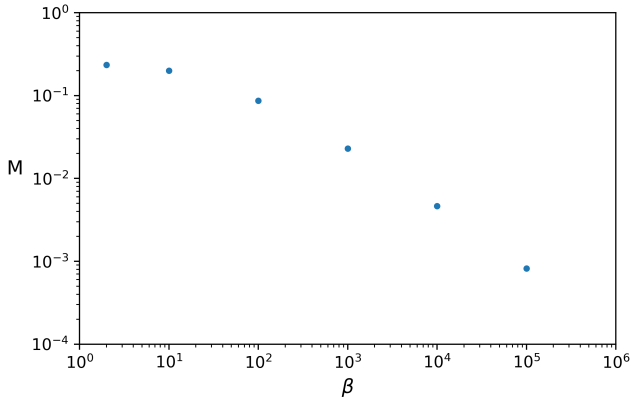

Figure 3.3: The maximum possible mass M (Eq. (3.1)) of the remaining oscillon decreases as the adiabaticity parameter β increases. In the limit $\beta \to \infty$, the system goes back to the AdS vacuum.

3.1.2. Crossing the resonances

We now analyse the system's response to a gradual modulation of the driving frequency as it traverses a resonant frequency. The process consists of three steps: an initial adiabatic injection of a stable time-periodic solution (TPS) at a chosen frequency; a slow modulation of this frequency upward or downward while keeping the driving amplitude constant; and a final adiabatic extraction of the driving, returning the system toward zero amplitude. This approach allows us to observe the effects of modulation across a resonant frequency by analysing the final states of the system.

[1] More details about these sourceless solutions can be found in [5].

Upward frequency chirping

When the driving frequency is gradually increased, as shown in Fig. 3.4, the system initially maintains a TPS state until the frequency reaches the resonant region. As the frequency approaches the resonance $\omega_{\rm b} \approx 3$, strong backreaction effects emerge, causing a significant mass increase in the system. This interaction causes the state to no longer be a TPS, resulting in an interference pattern between the driving frequency and that of a newly excited oscillon. This pattern becomes faster as the driving frequency continues to increase, moving further away from the frequency of the oscillon.

Once the driving is turned off, the system stabilizes into an oscillon state characterized by a spectral composition of the form $\omega_{\rm osc}(2k+1)$ with $k \geq 0$. The specific characteristics of the resulting oscillon vary depending on the modulation protocol, particularly the chirping speed. Indeed, if the modulation is too slow, the resonance can destabilize the system, leading it into the unstable region and causing it to collapse.

Downward frequency chirping

In contrast, when the frequency is chirped downward, as shown in Fig. 3.5, the system's behaviour changes significantly. As the driving approaches the linear resonant frequency, the field's amplitude, the backreaction on the metric and the mass increase steadily. The system evolves through a sequence of TPSs without crossing the oscillon line. That is, it follows one of the constant $\rho_{\rm b}$ curves shown in Fig. 2.1. We can choose a very small driving amplitude and try to trace a curve that follows the oscillon curve very closely.

The modulation can then be halted at a chosen frequency, where the driving is removed. The resulting state after this process is a stable oscillon with a similar frequency and mass to that of the last TPS encountered during the chirp. Downward chirping thus allows for the formation of an oscillon state that is generally more massive than one produced by upward chirping.

This downward frequency modulation protocol allows us to dynamically construct oscillons with much greater control over the final frequency than with the upward modulation protocol. We can increase the precision of the reached frequency through this process by choosing a smaller driving amplitude and following a curve closer to the oscillon line.

This chirping approach is also a valuable tool for mapping the full oscillon curve. By gradually decreasing the frequency while keeping the boundary amplitude particularly small, we capture the entire profile of oscillon states. Note in Fig. 2.1 that the curve for $\rho_{\rm b} = 10^{-4}$ and the oscillon line become indistinguishable as $\rho_{\rm o}$ begins to increase. In Fig. 3.6, we plot the evolution of the $\rho_{\rm b} = 10^{-4}$ curve, which reconstructs the oscillon curve, as well as the mass and the v.e.v. $\langle \mathcal{O} \rangle$ along this path. We observe a turning point in the mass profile $M(\omega_{\rm b})$, which corresponds to a stability limit. This point marks a threshold beyond which an oscillon collapses into a black hole, representing the *Chandrasekhar* limit.

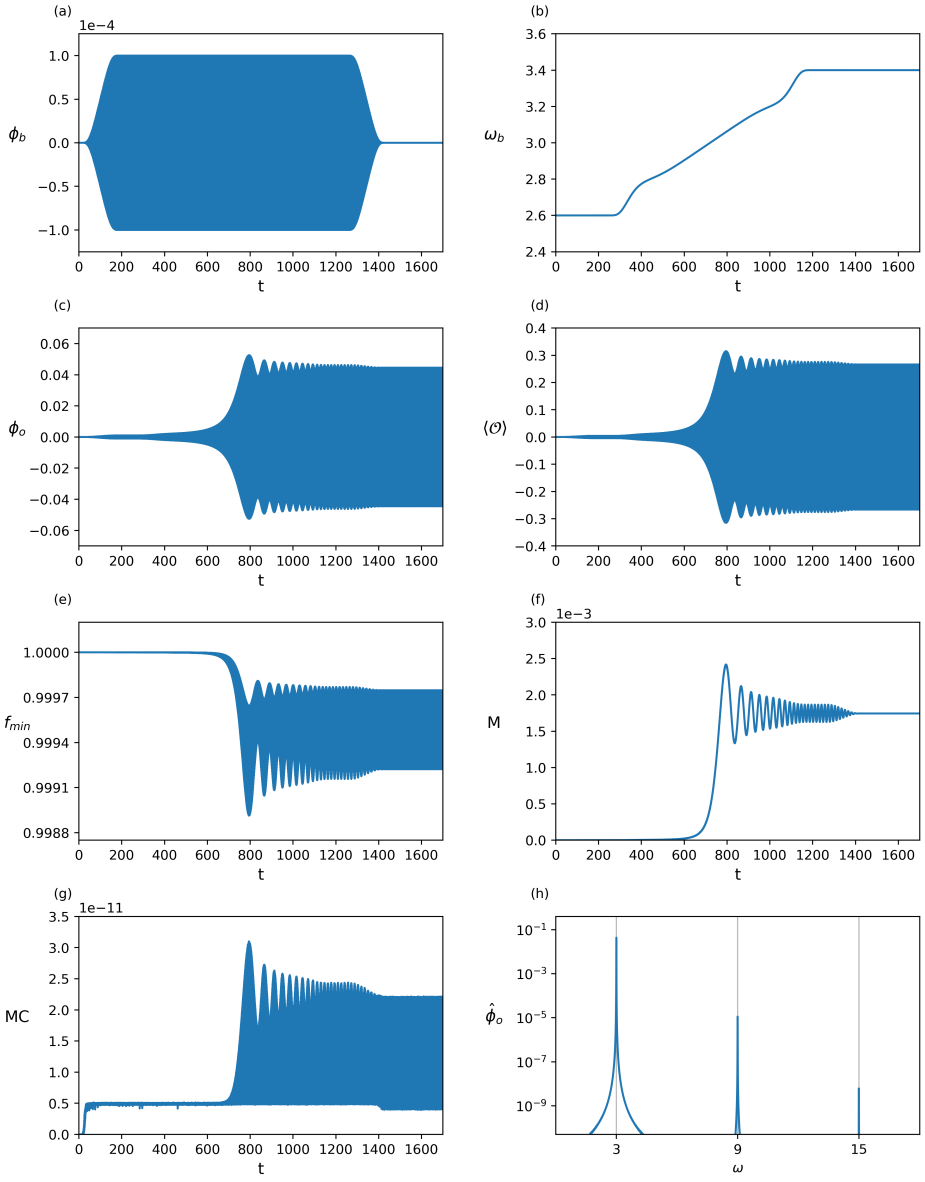

Figure 3.4: Up-chirping: (a-b) Driving consisting of an injection at a frequency $\omega_{\rm b} = 2.6$ up to a small amplitude $\rho_{\rm b} = 10^{-4}$, followed by a slow modulation in frequency ($\beta = 1000$) up to $\omega_{\rm b} = 3.4$, and a final extraction. (c-f) Resonance at $\omega_{\rm b} \approx 3$ generates substantial backreaction and mass increase. (g) The integrated Momentum Constraint supports the reliability of the simulations. (h) After the driving is turned off, an oscillon remains with the frequency spectrum $\omega_{\rm osc}(2k+1)$, with $k \geq 0$ and $\omega_{\rm osc} \approx 2.998$.

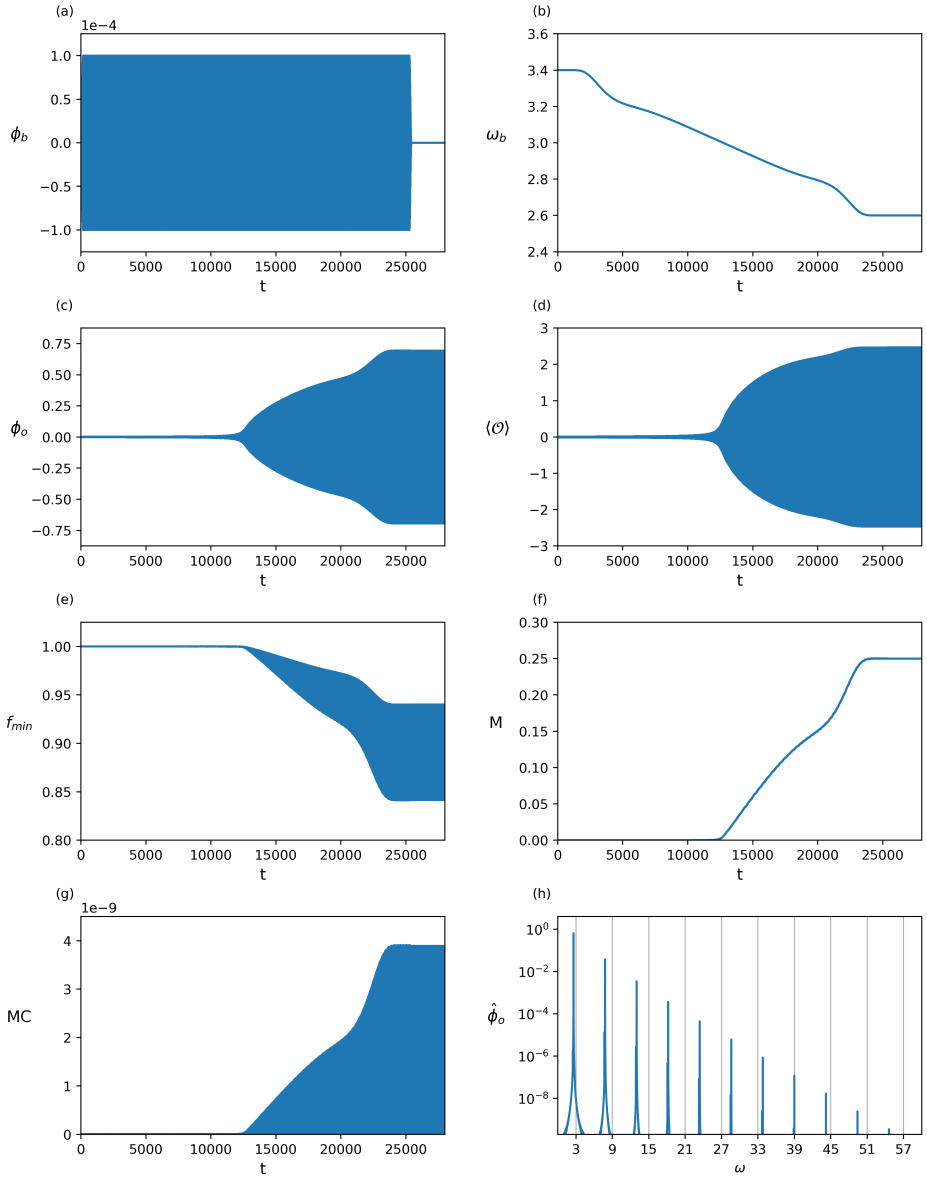

Figure 3.5: Down-chirping: (a-b) Driving with an initial injection at $\omega_{\rm b} = 3.4$, followed by slow downward modulation ($\beta = 2.5\times10^4$) to $\omega_{\rm b,final} = 2.6$, and a final extraction. As $\omega_{\rm b}$ approaches the linear resonant frequency, $\omega_{\rm b} = 3$, an increase occurs in the amplitude of the oscillations (c-d), in the backreaction on the metric (e), and in the mass (f). (g) The integrated Momentum Constraint supports the reliability of the simulations. (h) After extraction of the driving, the final state is an oscillon whose spectrum is $\omega_{\rm osc}(2k+1)$, with $k \geq 0$ and $\omega_{\rm osc} \approx \omega_{\rm b,final}$.

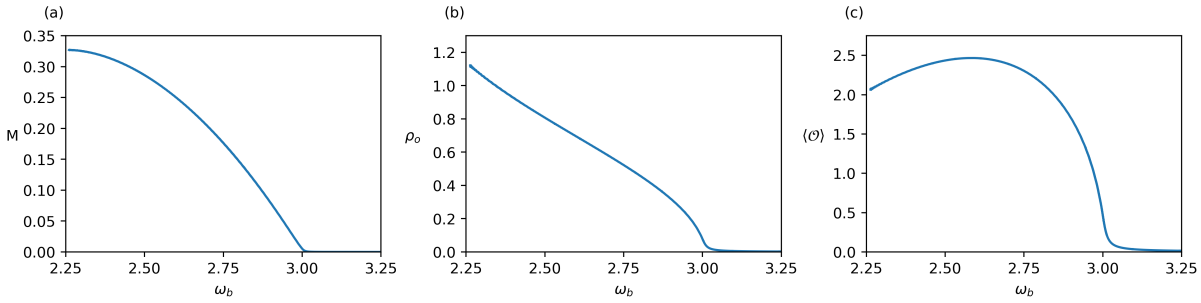

Figure 3.6: Oscillon mapping with frequency down-chirping. Starting at $\omega_{\rm b} = 3.25$ with $\rho_{\rm b} = 10^{-4}$, the frequency modulation continues down without stopping until the system collapses. (a) The mass curve shows a maximum that represents a stability limit. (b) $\rho_{\rm o}$ reconstructs the oscillon curve. (c) v.e.v. along the curve.

Frequency modulation without resonance crossing

If the modulation does not cross any resonance, the system evolves through a sequence of TPS states. A naive expectation would be that the system could return to the AdS vacuum when the driving is slowly removed. However, TPSs are periodic solutions where, in addition to the frequency $\omega_{\rm b}$ spanning a certain interval $\Delta\omega_{\rm b}$ during modulation, there are also higher harmonics $\omega_k = \omega_{\rm b}(2k+1)$ covering a broader interval $\Delta\omega_{\rm b}(2k+1)$. Some of these higher harmonics may cross a resonance, exciting an oscillon at that frequency. As shown in Fig. 3.7, once the driving is turned off, the scalar field retains a linear combination of excited linear normal modes, preserving a memory of the frequency modulation path. The amplitude of this *gas* of oscillons is, however, so small that no backreaction is observed, and the final state geometry remains AdS.

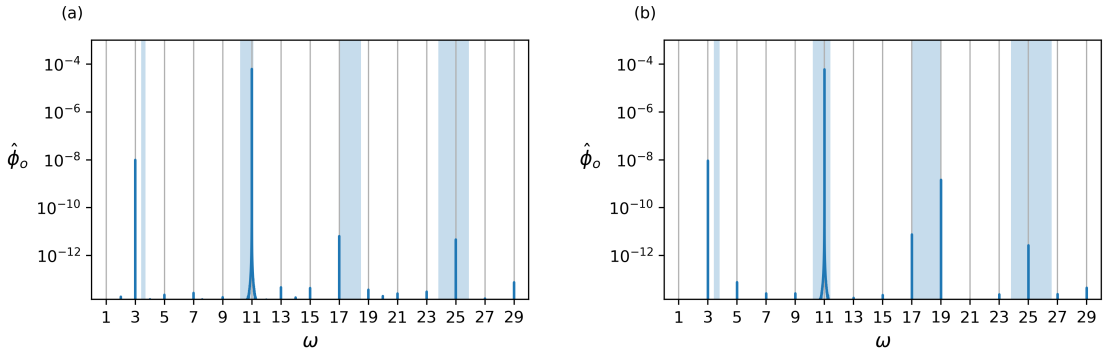

Figure 3.7: Frequency modulation without resonance crossing. Final Fourier decomposition of the scalar field at the origin after the extraction of a driving with amplitude $\rho_{\rm b} = 0.01$, modulated downwards over the intervals $\omega_{\rm b} = 3.7 \to 3.4$ (a) and $3.8 \to 3.4$ (b). The light blue shaded areas represent the frequency intervals spanned by the different harmonics of the TPSs during the frequency modulation. The resulting spectrum retains a memory of the path followed by the frequency modulation. In (b), where the driving starts at $\omega_{\rm b} = 3.8$, we observe that the harmonic with $k = 5$ has excited the mode at $\omega = 19$. In contrast, in (a), where the driving starts at $\omega_{\rm b} = 3.7$, the same harmonic does not cross this frequency, and thus the mode at $\omega = 19$ is not excited.

3.1.3. Solutions with vanishing v.e.v.

In the study of time-periodic solutions (TPSs) in AdS spacetimes, the linearized equations of motion admit two distinct families of solutions (see 2.1.1). The first family, denoted as $e_n^+(x)$, corresponds to modes with vanishing source and frequencies $\omega_n = 2n + 3 = 3, 5, ...$ in AdS_4. These solutions, which have been the primary focus of the previous subsections, give rise to non-linear oscillons. The second family, $e_n^-(x)$, consists of modes with vanishing v.e.v., defined by the condition $\partial_x^{(3)} e_n^-(x)\Big|_{x=\pi/2} = 0$. These solutions exhibit even frequencies in AdS_4, $\omega_n = 2n + 2 = 2, 4, ...$

The goal of this subsection is to identify lines of solutions with vanishing v.e.v. branching out from the even frequencies, in a manner analogous to how oscillons lines with vanishing source branch out from the frequencies $\omega_n = 2n + 3 = 3, 5, ...$ in the ω_b–ρ_o plane in Fig. 2.1.

Fig. 3.8 illustrates the protocol we followed. Starting from a constant ρ_b after an initial ramp-up, the frequency ω_b is slowly reduced. As the modulation crosses certain critical frequencies, which we identify with the aforementioned lines, the amplitude of the oscillations in both the mass and the v.e.v. decreases significantly. While $\langle \mathcal{O} \rangle$ appears to approach zero, closer examination (see inset in 3.8(d)) reveals that it does not vanish entirely. Interestingly, there is a subtle transition where the relative phase between the driving, $\phi_b(t)$, and the v.e.v., $\langle \mathcal{O}(t) \rangle$, shifts by π radians as the system moves through this region. This phase shift is analogous to the one observed between the boundary driving, $\phi_b(t)$, and the field at the origin, $\phi_o(t)$, when traversing the oscillon lines. In that case, the phase shift signals the emergence of an additional node in the profile function $\phi(t, x)$.

The most effective protocol for constructing the aforementioned curves that span solutions with almost vanishing v.e.v. involves performing small modulations in both amplitude and frequency, following the direction in which the v.e.v. is minimized and attempting to move along that curve. These lines are illustrated in Fig. 2.1.

A natural question arises as to why the solutions obtained with our protocol do not achieve a completely vanishing v.e.v. Solutions without v.e.v. share a conceptual symmetry with oscillon solutions. Oscillons are characterized by a vanishing source, $\phi_b(t) = 0$, while their field profile $\phi(t, x)$, and particularly their v.e.v., remain periodic but non-harmonic. Conversely, it is reasonable to expect that for solutions defined by $\langle \mathcal{O}(t) \rangle = 0$, the boundary source $\phi_b(t)$ must be periodic but non-harmonic. In this case, solutions with vanishing v.e.v. would be associated with a spectrum of the form $\omega_{\langle \mathcal{O} \rangle = 0}(2k + 1)$, similarly to how $\phi_o(t)$ and $\langle \mathcal{O} \rangle$ exhibit a spectrum of the form $\omega_{osc}(2k+1)$ for the oscillon solutions. Here, $\omega_{\langle \mathcal{O} \rangle = 0} \lesssim \omega_n = 2n+2$ would lie along the curves of vanishing v.e.v. branching out from the even frequencies (see Fig. 2.1).

The exact construction of these solutions remains an open question. The challenging problem to solve is to adapt the methods developed in Refs. [5, 24] to a context where non-normalizable modes do not allow us to immediately define a non-divergent inner product.

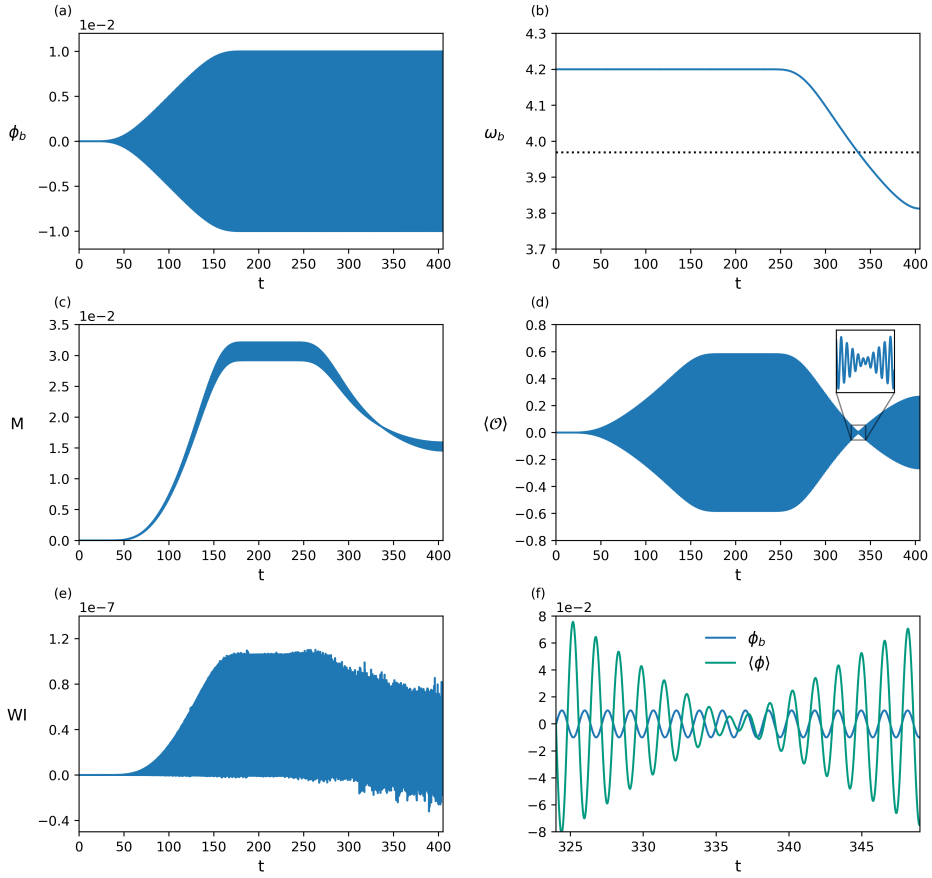

Figure 3.8: Construction of (almost) vanishing v.e.v. solutions. (a-b) Driving parameters: the amplitude ρ_{b} is held constant after a ramp-up with $\beta = 200$, while ω_{b} is modulated downwards. As the system crosses a critical frequency (dotted line), the oscillations in the mass (c) and the vev (d) reach a minimum. We identify this frequency as lying on a curve branching out from even frequencies in Fig. 2.1, corresponding to the non-normalizable solutions with vanishing v.e.v. in Eq. (2.14). (e) The Ward Identity is always well satisfied. (f) A π-radian shift in the relative phase between $\langle\mathcal{O}\rangle$ and ϕ_{b} is observed when transitioning across the region of (almost) vanishing v.e.v. solutions.

3.1.4. Solutions with negative average mass

Thus far, the TPSs we have observed exhibit masses oscillating above the AdS vacuum mass. We describe this behaviour as *energy-injecting*. This aligns with the holographic duality perspective, where AdS corresponds to the vacuum state in the boundary quantum field theory (QFT). In contrast, oscillons (sourceless, stable non-linear solutions) are interpreted as excited states of the dual QFT. Unlike oscillons, sourced TPSs are not expected to directly correspond to well-defined dual states of the dual QFT. Nevertheless, the concept of average mass remains meaningful by continuity. As we have observed in the previous sections, when the driving is gradually turned off, TPSs can evolve into oscillons. During this process, the average mass of the TPS smoothly transitions to the constant mass of the resulting oscillon, effectively bridging the gap between sourced and unsourced solutions.

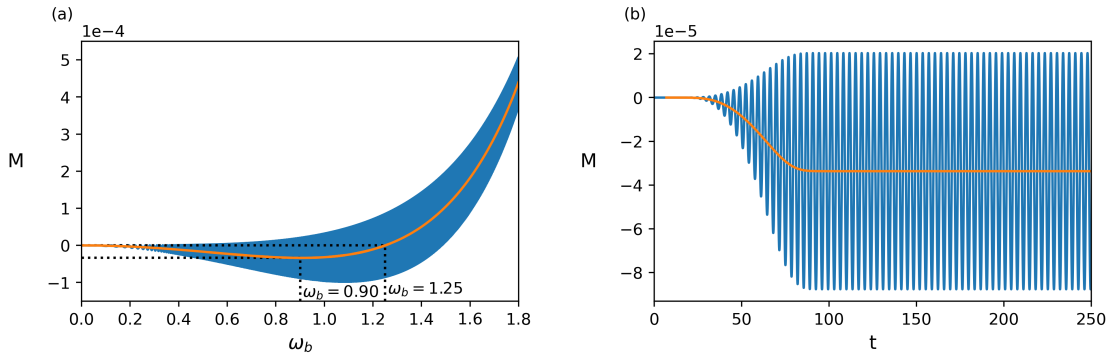

Figure 3.9: Negative average mass solutions: (a) TPSs obtained with a driving amplitude of $\rho_{\rm b} = 0.01$ while scanning over the frequencies $\omega_{\rm b} \in (0, 1.8]$. For each frequency $\omega_{\rm b}$, the mass of the corresponding TPS oscillates between a minimum and a maximum value, represented by the solid blue band, with the average mass given as the orange line. Solutions with $\omega_{\rm b} \leq 1.25$ exhibit a negative average mass. (b) Example of a TPS with $\omega_{\rm b} = 0.9$ and $\rho_{\rm b} = 0.01$, showing mass oscillations around an average mass below zero, obtained via adiabatic injection at a constant frequency.

If we search for TPSs at a low frequency of $\omega_{\rm b} \leq 1.25$, the situation becomes markedly different. Fig. 3.9(a) presents the collection of TPSs within the frequency range $\omega_{\rm b} \in (0, 1.8]$ and a driving amplitude of $\rho_{\rm b} = 0.01$. These solutions were obtained by starting with a TPS at $\omega_{\rm b} = 1.8$ and slowly modulating the frequency downwards until $\omega_{\rm b} = 0$. For each frequency, there exists a TPS where the mass oscillates between a minimum and a maximum value, represented by a solid blue band in the figure. The average mass[2] is also shown as an orange line.

Remarkably, for $\omega_{\rm b} \leq 1.25$, the average mass becomes negative, diverging from the typical energy-injecting behaviour of TPSs. An example of such a negative mass TPS is shown in Fig. 3.9(b), where the driving protocol involves an adiabatic injection at a constant frequency of $\omega_{\rm b} = 0.9$ up to an amplitude of $\rho_{\rm b} = 0.01$. In this case, the mass oscillates around a negative average value, demonstrating the viability of sustaining *energy-extracting* configurations under periodic driving.

The shaded region in Fig. 2.1 highlights the parameter space of TPSs with negative average mass. Fig. 3.10 focuses on this region, presenting level curves of constant average mass in the $\omega_{\rm b}$–$\rho_{\rm o}$ plane. Unfortunately, no oscillon states are found in this region that could allow a transition from driven TPSs to sourceless periodic configurations with negative mass. Such a state would represent a realization of a *holographic time crystal* [66].

Notably, as $\omega_{\rm b}$ decreases toward zero with a finite amplitude $\rho_{\rm b}$, the left edge in Fig. 3.10 is reached with a finite $\rho_{\rm o}$ (see Fig. 2.1), and the mass becomes zero. Alternatively, the frequency can be reduced by performing a double-scaling limit where $\omega_{\rm b} \to 0$ and $\rho_{\rm b} \to \infty$ while maintaining $\omega_{\rm b}\rho_{\rm b} \equiv \alpha_{\rm b}$ constant. This limit continuously connects the TPSs to the *pumping solutions* first studied in [28], where the scalar field's source grows linearly with time as $\phi_{\rm b}(t) = \alpha_{\rm b} t$.[3]

[2] By average mass, we refer to the time-averaged value over a period to eliminate periodic oscillations.

[3] See Appendix B in [10] for details on the connection between the TPSs and the pumping solution under this limit.

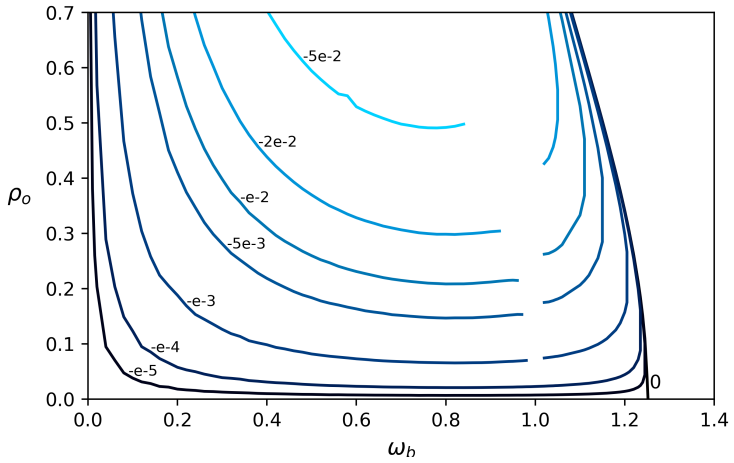

Figure 3.10: Level curves of constant negative average mass in the $(\omega_{\rm b}, \rho_{\rm o})$ plane. The left edge of the plot shows that solutions with finite $\rho_{\rm b}$ and $\omega_{\rm b} \to 0$ return to $M = 0$. A double-scaling limit where $\omega_{\rm b} \to 0$ and $\rho_{\rm b} \to \infty$ allows connecting these negative mass TPSs to the pumping solutions, which are characterized by a source that grows linearly with time, $\phi_{\rm b}(t) = \alpha_{\rm b} t$. The discontinuity observed around $\omega_{\rm b} = 1$ occurs because the higher harmonics of the TPS interfere with the resonances around $\omega_n = 2n + 1$ for $n > 0$.

Pumping solutions can have a negative mass that is sustained as long as the source remains active. It is worth noting the work in [67], where a periodic driving is applied to a charged black hole dual to a thermal (positive mass) state. In that context, it is possible to have a net mass-energy extraction after switching off the periodic driving.

3.2. Blocking the cascade: double-frequency resonant driving

A natural question to continue the study of driven systems after the success of the adiabatic injection protocol to construct non-linear oscillons is: what happens when the system is driven by more than one resonant frequency? This section explores the dynamics and outcomes of driving the system at two resonances, both while the driving is active and after switching it off. There are several ways to apply such a driving to the system. Here, we present three different protocols.

Sequential injection of two resonant drivings

The first protocol investigates the outcome of adiabatically injecting and extracting two resonant drivings sequentially. This can be done in various ways, such as modifying the order or the duration of the driving injections. The procedure described here and shown in Fig. 3.11 produces one of the cleanest outcomes. Starting from the AdS vacuum, we first drive the system at $\omega_{\rm b} = 5$ and then extract this driving to form an oscillon, similar to the one created in 3.1.1. Once this oscillon is formed, a second driving at $\omega_{\rm b} = 3$ is introduced and removed adiabatically.

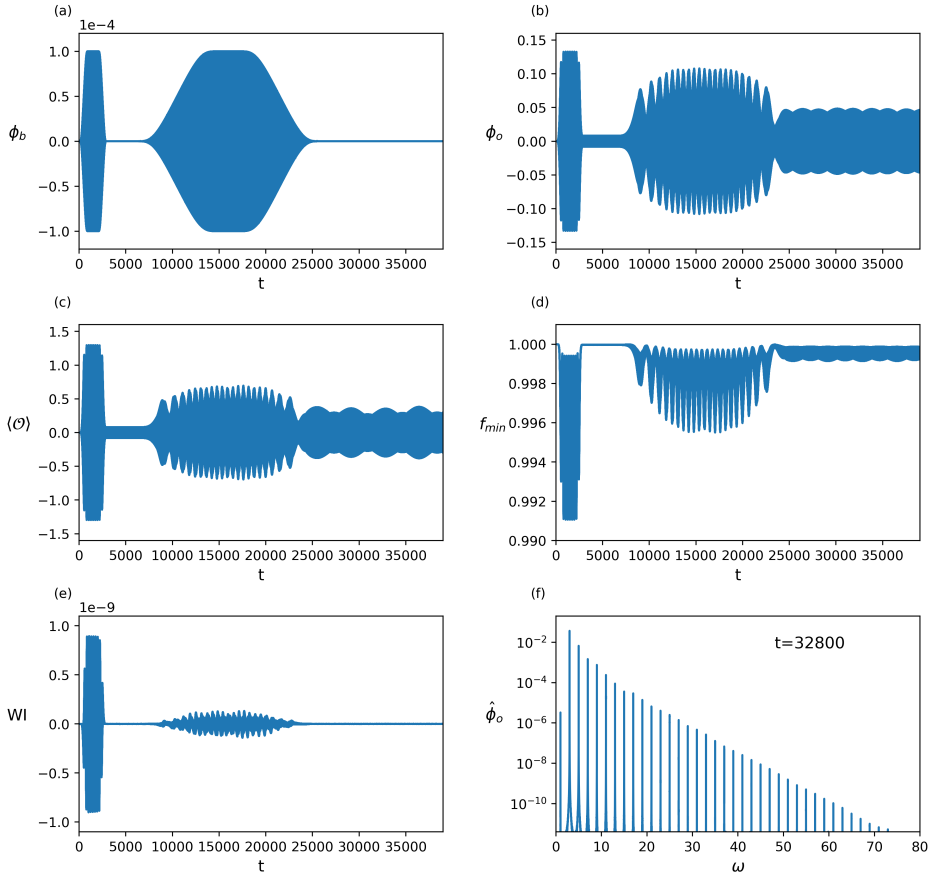

Figure 3.11: Sequential injection of two resonant frequencies. (a) Injection and extraction of the first driving at $\omega_b = 5$, amplitude $\rho_b = 10^{-4}$, and injection and extraction time of $\beta = 1000$, followed by the same procedure for a driving at $\omega_b = 3$ with the same amplitude and $\beta = 10000$. (b-d) When the second driving is injected, an interference pattern emerges. After extracting this last driving, the system evolves into the quasi-periodic solution observed for $t > 2.5 \times 10^4$. (e) The Ward Identity is always well satisfied. (f) The spectrum of the state after switching off both drivings displays the frequencies $\omega_k = \omega_0(2k+1)$ with $\omega_0 = 0.9994$, and shows an exponential decay beginning at the dominant frequency $\omega = 3$. The Fourier transform was performed at a central time $t = 32800$ with a window of $\Delta t = 10^4$.

The naive expectation of a non-linear two-frequency state after switching off the driving is not realized.[4] As shown in Fig. 3.11(b-d), the remnant solution exhibits quasi-periodic behaviour. The Fourier transform of this solution, displayed in Fig. 3.11(f), reveals a spectrum composed of frequencies $\omega_k = \omega_0(2k+1)$, where $\omega_0 = 0.9994$ is very close to 1. The spectrum shows an exponential decay in amplitude, beginning at the dominant frequency $\omega = 3$. This result connects to the solutions presented in [22] (see Figs. 1 and 2), where similar quasi-periodic states with exponential decay were observed in the context of the effective Two-Time Formalism.

[4] Non-linear two-mode oscillons constructed in [68, 69] have frequencies not related to those of the linearized normal modes.

Frequency chirping across multiple resonances

The second protocol employs a frequency chirping method to traverse multiple resonant oscillon branches. As shown in Fig. 3.12, a driving of the same amplitude as before, $\rho_{\mathrm{b}} = 10^{-4}$, is injected at $\omega_{\mathrm{b}} = 2.8$. Subsequently, the driving frequency is gradually increased to $\omega_{\mathrm{b}} = 5.2$, crossing both the $\omega_{\mathrm{b}} \sim 3$ and $\omega_{\mathrm{b}} \sim 5$ oscillon lines. After the driving is extracted, the system is left with a strongly modulated quasi-periodic oscillation, as seen in Fig. 3.12(c-d). The time-dependent Fourier spectrum of the remnant state exhibits an exponential decay and alternates in time between configurations dominated by $\omega = 3$ and $\omega = 5$, as shown in Fig. 3.12(e-f). These states again show similarities to the solutions proposed in [22].

Although less evident, this back-and-forth movement is also present in the first protocol involving

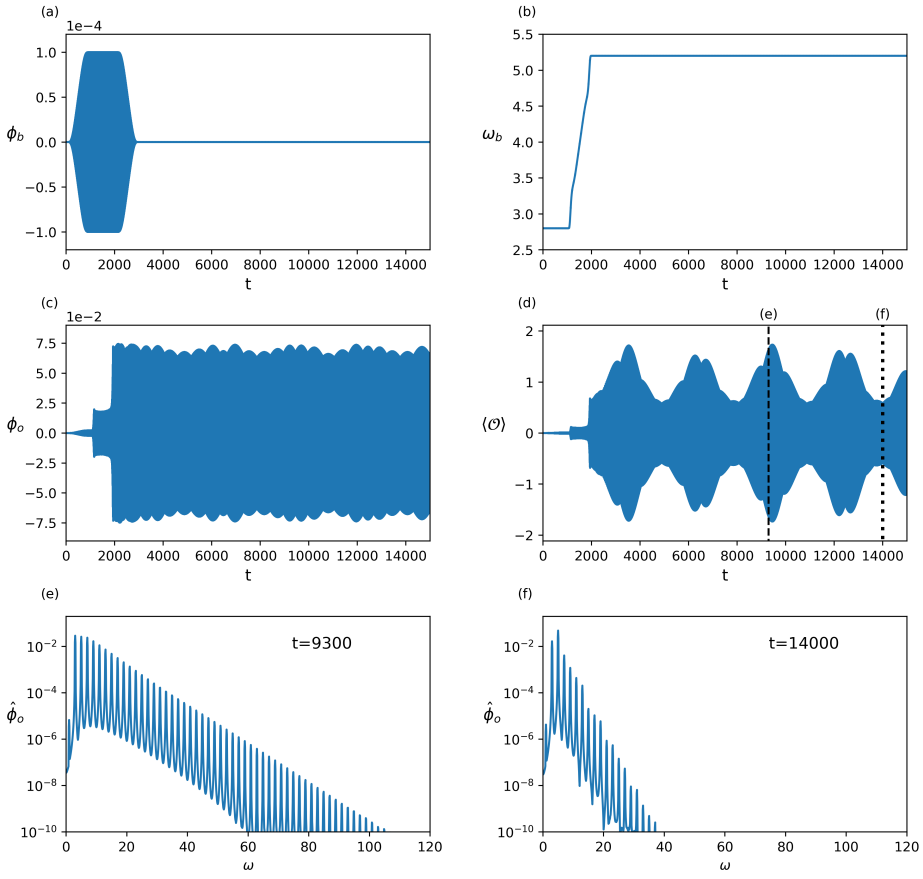

Figure 3.12: Frequency chirping across multiple resonances. (a-b) Injection of a driving at $\omega_{\mathrm{b}} = 2.8$ with an amplitude of $\rho_{\mathrm{b}} = 10^{-4}$, followed by a frequency modulation up to $\omega_{\mathrm{b}} = 5.2$ over a time of $\beta = 1000$, and a final extraction of the driving. (c-d) After the driving is switched off, there remains a solution with a quasi-periodic modulation in amplitude. (e-f) The Fourier spectrum of the final state consists of the frequencies $\omega_k = 2k + 1$, with $k \geq 0$, and alternates in time between exponentially decaying spectra dominated by $\omega = 3$ and $\omega = 5$. Two instants illustrating these distinct dominances are shown in plots (e) and (f) at the times marked by vertical lines in plot (d).

the sequential injection of the drivings shown in Fig. 3.11. In that case, however, this oscillation is much smaller and the dominant frequency does not change.

Simultaneous injection of two resonant drivings: blocking the energy cascade

The third protocol involves injecting and extracting a driving with two frequencies simultaneously, $\omega_{\mathrm{b}} = 3$ and 5. During the driving phase, a strong interference pattern dominates the interior dynamics, as shown in Fig. 3.13(b-d). Once the driving is removed, the envelope becomes smooth, but the oscillation amplitude begins to grow unboundedly, suggesting an eventual collapse into a black hole.

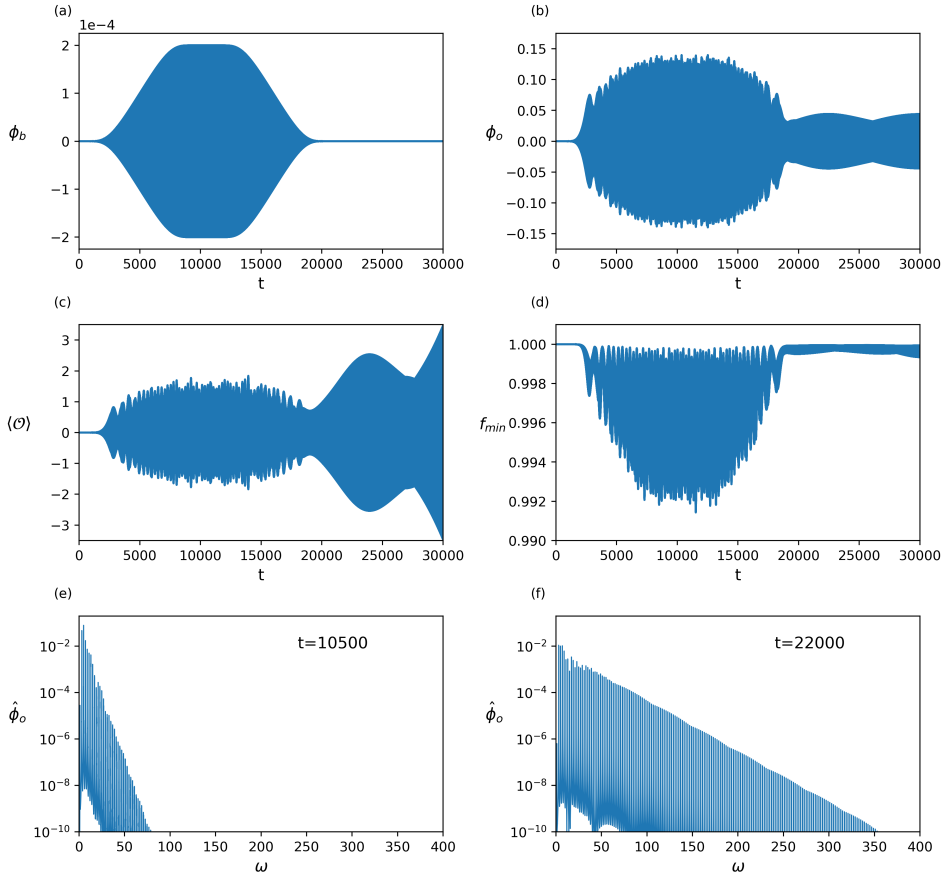

Figure 3.13: Simultaneous injection of two resonant frequencies. (a) Injection of a driving with two frequencies, $\omega_{\mathrm{b}} = 3$ and 5. (b-d) While the driving is on, a strong interference pattern is observed. After extraction of the driving, a monotonic increase in amplitude, mainly observable in the v.e.v. $\langle\mathcal{O}\rangle$ (c), begins immediately. (e-f) The Fourier spectrum consists of the frequencies $\omega_k = 2k + 1$ with $k \geq 0$. It reveals that while the driving is active (e), the energy cascade to higher frequencies is blocked. Once the driving is switched off (f), a rapid population of higher frequencies begins. This seems to be consistent with non-linear turbulent behaviour leading to future collapse. However, the convergence drops monotonically from its value of 4, and the simulation stops being reliable.

Fourier analysis reveals significant differences between the dynamics during the driven phase and after the driving is switched off. During the driving phase, shown in Fig. 3.13(e), the spectrum decays rapidly and the energy transfer to higher modes is suppressed. However, once the driving is removed, as shown in Fig. 3.13(f), a cascade begins, rapidly populating higher energy modes. The transition between these two regimes occurs very quickly once the driving is switched off. This behaviour suggests that the system transitions into a turbulent regime, potentially leading to a collapse into a black hole.

Interestingly, the driving can be kept on, and the regularity and the strong fall-down of the spectrum are preserved for very long-time drivings. Indeed, the open periodically-driven system remains stable and maintains fourth-order convergence for as long as we have been able to simulate it. In the boundary language for Floquet systems, this behaviour indicates that for sufficiently low driving amplitudes, the driving acts to keep a non-heating phase, where coherence is preserved and thermalization is avoided, similar to what is observed for the single-resonant-driven TPSs. From the bulk perspective, the exchange of energy-momentum through the boundary[5] acts to block the turbulent cascade. It would be interesting to clarify this issue by resorting to a resonant analysis of the non-normalizable solutions, probably along the lines of [70].

It is worth noting that the final fate of the system after the two-frequency driving is removed remains speculative.[6] While the unbounded growth of oscillation amplitude and rapid population of higher modes strongly suggest collapse into a black hole, simulating the dynamics of this collapse is numerically challenging. Convergence tests, provided in D, confirm the reliability of the simulation during the driven phase, achieving a convergence factor of 4. However, they highlight the numerical difficulties in capturing the late-time cascade, which is not fast enough to show collapse into a black hole before convergence deteriorates.

3.3. Multi-frequency resonant driving: simulating stochastic noise

After analysing single-frequency and two-frequency resonant drivings, this section addresses the system's response under a multi-mode driving. Here, we introduce a driving composed of a non-coherent ensemble of resonant frequencies, thereby modelling stochastic noise. The initial motivation for this approach is to model a holographic open system coupled to a thermal bath. In the setup presented here, a parameter T takes on the role of the environment temperature.

The boundary driving is implemented as a sum of multiple resonant modes:

$$\phi_{\mathrm{b}}(t) = \frac{\epsilon}{N(T)} \sum_{i=1}^{n} \phi_n \cos(\omega_{\mathrm{b},n} t + \varphi_n), \tag{3.2}$$

where ϵ is a constant that controls the overall amplitude of the driving, and $N(T)$ is a nor-

[5] Note that, from Eqs. (2.9) and (2.10), it follows that $\langle T_{ij} \rangle$ varies with time when $\dot{\phi}_0$ and ϕ_3 are nonzero.

[6] In [71], using the Two-Time Formalism, two-mode data were conjectured to initialize solutions that collapse in infinite time.

malization factor that will be determined to ensure that the total power of the signal remains independent of the temperature T. The relative amplitudes ϕ_n are distributed according to:

$$\phi_n^2 = \frac{n_{\mathrm{BE}}}{\omega_n}\ , \quad n_{\mathrm{BE}} = (e^{\omega_n/T} - 1)^{-1}, \tag{3.3}$$

where n_{BE} represents the Bose-Einstein distribution, and T controls the amplitude decay with frequency. This formulation ensures that the relative amplitudes of the driving's time derivative, $\Pi_n = \omega_n \phi_n$, follow a Johnson-Nyquist noise distribution [72]:

$$\Pi_n^2 = \omega_n n_{\mathrm{BE}}. \tag{3.4}$$

The power spectral density of Π_{b} is given by:

$$P(\omega) = \frac{\epsilon^2}{N(T)^2} \sum_{n=1}^{\infty} \Pi_n^2 \delta(\omega - \omega_n), \tag{3.5}$$

and the normalization factor $N(T)$ is chosen such that:

$$N(T)^2 = \sum_{n=1}^{\infty} \Pi_n^2, \tag{3.6}$$

ensuring, as mentioned earlier, that the total power remains independent of T:

$$P = \int_{-\infty}^{\infty} P(\omega) d\omega = \epsilon^2. \tag{3.7}$$

The driving frequencies correspond to resonant modes $\omega_n = 2n + 3$, while the phases φ_n are randomly distributed in $[0, 2\pi)$. This setup mimics thermal noise restricted to the resonant frequencies.

Numerical simulations were performed for different values of T, with the multi-mode driving gradually injected up to $\epsilon = 2 \times 10^{-4}$ over an extended injection time $\beta = 2 \times 10^4$ to minimize overheating effects due to the injection quench.

The system's response varies significantly with the noise temperature T. Fig. 3.14(a) shows the envelope of $\Pi(t, x = 0)^2$ for these simulations. This quantity is related to the scalar curvature at the origin, $R = -2\Pi(t, x = 0)^2/l^2 - 12/l^2$, and its growth was previously proposed in [4] as a useful diagnostic for identifying dynamics that lead to collapse into a black hole.

The results suggest the existence of a threshold temperature at approximately $T \sim 0.7$. Above this value, the dynamics absorb energy monotonically since the beginning of the simulation, suggesting that the system may be on a trajectory toward collapse into a black hole. Unfortunately, the convergence[7] deteriorates before the simulations can definitively show collapse. The results are shown up to the point where the convergence factor drops below 2.

[7] Convergence tests are provided in Appendix D.

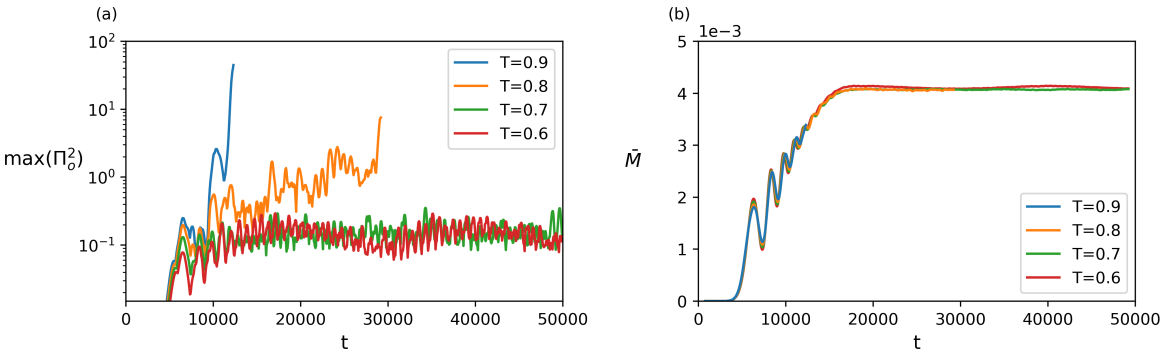

Figure 3.14: Multi-resonant mode driving: (a) Envelope of $\Pi(t, x = 0)^2$, showing different behaviour above and below $T \sim 0.7$. (b) Mass averaged over many oscillations, displaying similar behaviour for the different temperatures. In both plots, the curves end at the time when the convergence factor drops below 2.

Conversely, for temperatures below the threshold, the dynamics remained regular for as long as the simulations were run. In this regime, fourth-order convergence is maintained, and the oscillations in $\Pi(t, x = 0)$ saturate at a finite amplitude. It should be noted that these results do not rule out the possibility of a later regime that could lead to destabilization for longer timescales. For clarity, the number of active modes (i.e. those contributing above the machine precision value) ranges from 22 for $T = 0.6$ to 34 for $T = 0.9$.

In Fig. 3.14(b), the mass of the system, averaged over many oscillation periods, is shown for the same simulations. The mass evolution is similar for the different temperatures and does not provide evidence of the possibility of an eventual collapse.

3.4. Summary

In this chapter, we have analysed how a massless scalar field in AdS spacetime responds to a periodic external driving. We first examined the system's response to a single-mode driving at a resonant frequency. When the driving is active, interference patterns emerge, consisting of the driving frequency and a slightly lower secondary frequency. After the driving is switched off, the system evolves into a stable, self-sustained oscillating solution, referred to as an oscillon. The properties of the resulting oscillon, such as its mass and frequency, depend on the amplitude reached during the driving phase, the rate at which the driving is turned off, and the moment when the extraction begins. If the extraction process is very slow, the system tends to relax back to the AdS vacuum state.

Another approach explored in this study involves modulating the driving frequency over time, known as chirping. It was found that both increasing and decreasing the driving frequency can produce oscillons, although downward modulation is more effective and easier to control. This method allows the system to closely follow the oscillon curve, enabling the creation of an oscillon at a chosen frequency. Interestingly, even if the driving frequency is modulated without directly crossing a resonance, higher harmonics can still trigger oscillon formation.

This study also identified time-periodic solutions with negative mass in the case of a low-frequency driving, and explored a non-linear extension of the solutions without v.e.v., similar to the oscillon lines that emerge from the resonant frequencies in Fig. 2.1.

Furthermore, the effect of applying two distinct driving frequencies was investigated, revealing complex spectral behaviours. Some solutions display frequency components that shift over time, and certain driving protocols appear to temporarily suppress the energy cascade while the driving is active, with the cascade resuming once the driving stops.

Finally, we modelled noise by applying a multi-frequency driving signal designed to emulate a thermal bath. These simulations suggest the existence of a critical temperature-like parameter, above which the system appears to head toward collapse, and below which the dynamics remain regular for extended periods.

In the next chapter, we will study the AdS instability from a different perspective. Instead of imposing a time-dependent driving, we will set mixed boundary conditions and investigate how altering the resonant structure of the spectrum affects stability.

Chapter 4

Non-linear instability with mixed boundary conditions

A crucial insight gained from research following the initial work of P. Bizoń and A. Rostworowski [4] is that the occurrence of BR instability requires the initial data to be interpretable as a small perturbation of a geometry with an exactly resonant eigenfrequency spectrum [31]. This resonance enables the turbulent energy cascade that characterizes the instability. While this condition is fulfilled in the AdS vacuum, it is absent in time-periodic configurations such as oscillons [5, 6], boson stars [7, 8], or static geometries such as solitons within the Einstein-Maxwell-scalar theory [9]. These geometries act as attractors and form *islands of non-linear stability* [5,6,31] in the space of initial data, where both direct and inverse energy cascades [22] occur, balancing each other and preventing the transfer of energy to higher and higher modes, thereby effectively avoiding gravitational collapse.

The approach to studying the role of the resonant character of the eigenfrequency spectrum in the BR instability can be thought of as proceeding in three steps. First, one identifies a special excited state exhibiting either discrete or continuous time-translational invariance, such that the concept of a normal mode is applicable. Second, one checks by an explicit computation that the resonant property of the AdS vacuum spectrum is spontaneously broken in this excited state. Finally, it remains to assess whether the non-linearly stable initial data of interest can indeed be understood as a special excited state subject to a finite, but sufficiently small, perturbation [31].

In this chapter, we propose an alternative route. Rather than focusing on stability islands sourced by special excited states in our original theory, we will instead consider a deformed theory where the boundary conditions at asymptotic infinity are modified and the resonant character of the AdS vacuum spectrum is explicitly broken from the very beginning. This allows studying the interplay of the resonance condition and the BR instability in initial data corresponding to a *bona fide* perturbation of the AdS vacuum.

In order to implement the mentioned deformed quantum theory and the boundary conditions, we will use the framework described in 2.2. We work with a system that allows mixed boundary conditions. Specifically, our setup is the Einstein-Klein-Gordon system described in 2.2.4,

Einstein gravity in AdS_4 coupled to a scalar field with the potential

$$V(\phi) = -4\sinh\left(\frac{\phi}{2}\right)^2, \tag{4.1}$$

which corresponds to a scalar field with mass squared $m^2 = -2$. Near the boundary, the field exhibits the following behaviour :

$$\phi = \frac{\alpha}{r} + \frac{\beta}{r^2} + \dots \tag{4.2}$$

We impose boundary conditions of the form:

$$\beta_{\rm BC}(\alpha) = c_n \alpha^{n-1}\,, \quad \text{with } n = 2, 3, 4. \tag{4.3}$$

As explained in 2.2.2, this type of boundary conditions corresponds to a multi-trace deformation of the Lagrangian of the dual CFT. When $c_n = 0$ in (4.3), we recover $\beta = 0$ boundary conditions, meaning our undeformed theory is the CFT in the alternative quantization. Therefore, we are in the situation described by expressions (2.44) and (2.45), and the boundary conditions (4.3) correspond to a deformation of the CFT Lagrangian of the form

$$\mathcal{W} = \frac{c}{n}\int d^3x \mathcal{O}^n. \tag{4.4}$$

Given that $\mathcal{O}$ is a single-trace primary operator with conformal dimension $\Delta = 1$, we classify the deformations as follows:

- $\mathcal{O}$ and $\mathcal{O}^2$ are relevant deformations.
- $\mathcal{O}^3$ is a marginal deformation. This triple-trace deformation corresponds to a designer gravity boundary condition of the form

  $$\beta_{BC}(\alpha) = c_3\alpha^2, \tag{4.5}$$

  and is singled out by the property that it does not destroy the algebra of asymptotic isometries of global AdS_4 (see 2.2.3.4 and Refs. [59, 73]).
- $\mathcal{O}^n$ with $n \geq 4$ are irrelevant deformations.

This study builds on numerical simulations to explore stability under these different types of boundary conditions. The equations of motion for our AdS-Einstein-scalar system and an explanation of how to recast them in a form suitable for numerical implementation are included in Appendix B. Details about our simulation code and convergence tests are provided in Appendix D.

Once the setup is established, we follow an approach similar to the one introduced in [4]. We set the following Gaussian initial data:

$$\Pi(t=0,x) = \frac{2\varepsilon}{\pi}\exp\left(-\frac{4\tan^2 x}{\pi^2\sigma^2}\right), \tag{4.6a}$$

$$\Phi(t=0,x) = 0, \tag{4.6b}$$

where the Gaussian width σ remains fixed while the amplitude ε is varied. Throughout most of the analysis, unless otherwise stated, we set $\sigma = 0.1$, This is a narrow width compared with the AdS radius $L = 1$, and the scalar field propagates as a wave packet. The procedure consists of evolving the initial data (4.6) in time exploring a range of values for the amplitude ε. The main objective is to determine whether, for sufficiently low amplitudes, the non-linear instability (BR instability) observed in the undeformed CFT persists or not. This procedure is repeated for the different types of mixed boundary conditions (4.3) with $n = 2, 3$ and 4, corresponding to relevant, marginal and irrelevant deformations respectively.

4.1. Marginal deformations

We begin with the case of marginal triple-trace deformations, which correspond to boundary conditions of the form $\beta = c_3\alpha^2$. For this type of deformation, our numerical simulations indicate that the non-linear instability persists, exhibiting the same behaviour as observed in [4]. Fig. 4.1 illustrates the collapse time t_{col} as a function of the initial amplitude ε for various marginal deformations, as well as for the undeformed case ($\beta = 0$). All these boundary conditions exhibit non-linear instability as $\varepsilon \to 0$, with the collapse time scaling as $t_{\text{col}} \sim \varepsilon^{-2}$, consistent with the behaviour of the BR instability.

This behaviour is expected for marginal deformations, as they do not alter the resonant structure of the AdS eigenfrequency spectrum (see section 2.2.4) and the asymptotic symmetries of AdS are preserved (see 2.2.3).

Further evidence of a BR-like instability is found by examining the envelope of $\Pi(t, x = 0)^2$. This quantity was already proposed in [4] as a reliable indicator of instability emergence due to its relationship with the scalar curvature at the origin. Fig. 4.2 shows that, as in the undeformed

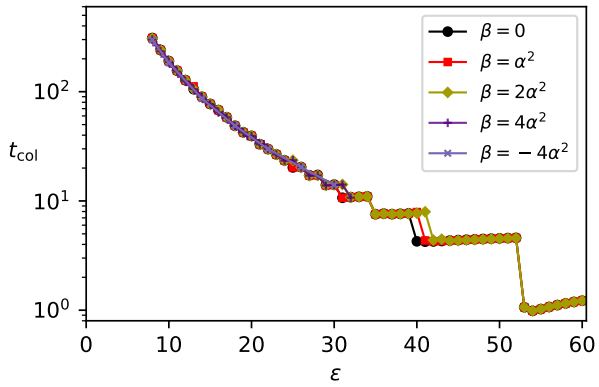

Figure 4.1: Collapse time t_{col} as a function of the initial amplitude ε for some different boundary conditions of the form $\beta \propto \alpha^2$ (marginal deformations) and for the case with $\beta = 0$ (no deformation). The BR instability is preserved, with t_{col} scaling as ε^{-2} for $\varepsilon \to 0$ and behaving as in the undeformed case. Although this study focuses on the behaviour as $\varepsilon \to 0$, for the higher amplitudes shown, the jumps in the collapse time corresponding to a different number of reflections from the AdS boundary are clearly visible.

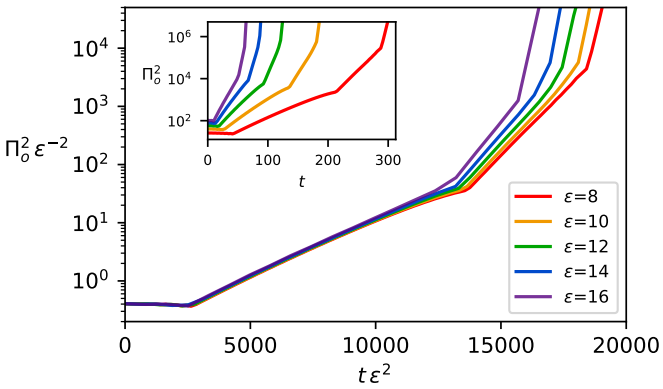

Figure 4.2: The inset shows the upper envelope of $\Pi(t, x = 0)^2$ for some evolutions with $\beta = 2\alpha^2$ boundary conditions (marginal deformations) and small amplitudes ε. This quantity, related to the curvature scalar at the origin, highlights the onset of instability and exhibits several distinct phases of increasing growth. The main plot shows the rescaled curves $\varepsilon^{-2}\Pi^2(\varepsilon^2 t, x = 0)$ approaching a universal profile characteristic of the BR instability.

case, for marginal deformations the rescaled quantity $\varepsilon^{-2}\Pi^2(\varepsilon^2 t, x = 0)$ converges to a universal curve for small amplitudes ε. This curve also reflects the characteristic progression of the BR instability, displaying several distinct phases clearly marked. Initially, the upper envelope of $\Pi(t, x = 0)^2$ remains approximately constant, but after some time, a phase of exponential growth begins suddenly. Subsequently, different phases emerge, each exhibiting increasingly rapid growth, until collapse ultimately occurs.

4.2. Irrelevant deformations

For boundary conditions of the form $\beta = c_4\alpha^3$, our findings reveal that such deformations also do not seem to disrupt the non-linear instability, at least within the parameter space explored by the numerical simulations presented in Fig. 4.3. This figure shows the collapse time t_{col} as a function of the initial amplitude ε for various irrelevant deformations and for the undeformed case.

In Fig. 4.4, we analyse the scaling of the instability evolution with the amplitude, as was done for the marginal deformations, but now for an irrelevant deformation of the form $\beta = 2\alpha^3$. We observe again that the rescaled quantity $\varepsilon^{-2}\Pi^2(\varepsilon^2 t, x = 0)$ approaches a universal curve for small amplitudes.[1]

[1]The growth of the rescaled curvature at the origin for irrelevant deformations (Fig. 4.4) appears to be slightly delayed compared to the rescaled curve for marginal deformations (Fig. 4.2). A potential connection between this observation and the comment on irrelevant deformations made at the end of this chapter warrants further investigation.

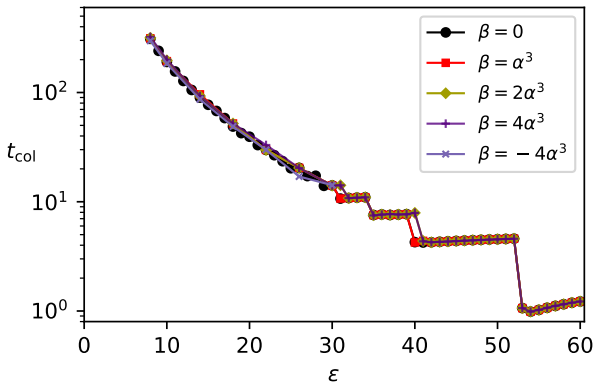

Figure 4.3: Collapse time t_{col} as a function of the initial amplitude ε for various boundary conditions of the form $\beta \propto \alpha^3$ (irrelevant deformations) and for the case with $\beta = 0$ (no deformation). The BR instability is preserved, with t_{col} scaling as ε^{-2} for $\varepsilon \to 0$ and behaving as in the undeformed case.

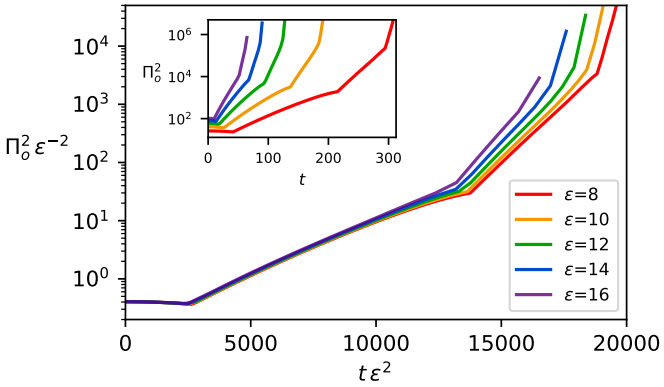

Figure 4.4: The inset shows the upper envelope of $\Pi(t, x = 0)^2$ for some evolutions with $\beta = 2\alpha^3$ boundary conditions (irrelevant deformations) and small amplitudes ε. This quantity, related to the curvature scalar at the origin, highlights the onset of instability and exhibits several distinct phases of increasing growth. The main plot shows the rescaled curves $\varepsilon^{-2}\Pi^2(\varepsilon^2 t, x = 0)$ approaching a universal profile characteristic of the BR instability.

4.3. Relevant deformations

Boundary conditions of the form $\beta = c_2\alpha$, corresponding to relevant deformations, behave quite differently from the cases discussed previously. As we already observed in 2.2.4, these deformations alter the normal mode frequencies in such a way that the spectrum is no longer exactly resonant but only asymptotically so. Furthermore, the system's response varies significantly depending on the sign of c_2.

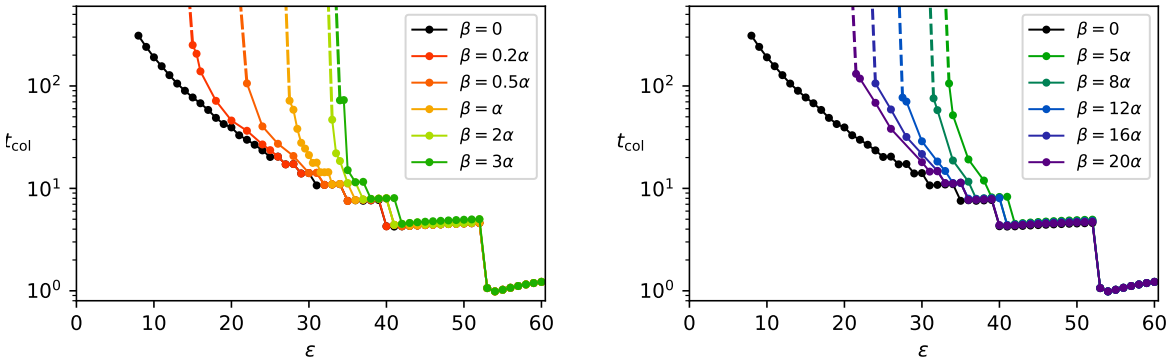

Figure 4.5: Collapse time $t_{\rm col}$ as a function of the initial amplitude ε for various boundary conditions of the form $\beta = c_2\alpha$ (relevant deformations) with $c_2 > 0$, and for the case with $\beta = 0$ (no deformation). The BR instability has disappeared (dashed lines connect to evolutions which have not yet undergone gravitational collapse). Left panel: Upon increasing c_2 away from zero, the collapse time curves depart from the $\beta = 0$ one at progressively larger values of ε. Right panel: Increasing c_2 further, after a critical value, the collapse time curves start to lie down again. The reason for this behaviour is that, in the $c_2 \to \infty$ limit, we should recover the alternative quantization result, where the BR instability is again present.

4.3.1. Positive c_2

In the case of positive c_2, Fig. 4.5 shows the collapse time $t_{\rm col}$ as a function of the initial data amplitude ε for various double-trace deformations, $\beta = c_2\alpha$, with $c_2 > 0$. We observe that the BR instability disappears for any finite value of c_2 when ε is sufficiently small. The left panel illustrates how, as c_2 increases, the system becomes stable at progressively larger values of ε. This behaviour exhibits a maximum value of ε for which the system becomes stable, observed around $c_2 \sim 3$ to 5.

As shown in the right panel, for higher values of c_2, the collapse time curves start to descend again, approaching the undeformed case curve. This behaviour can be understood by noting that, in the limit $c_2 \to \infty$, the ratio $\alpha/\beta \to 0$, and the system approaches Dirichlet boundary conditions ($\alpha = 0$) or standard quantization (see section 2.2), where the BR instability re-emerges.

4.3.2. Negative c_2

For boundary conditions with $c_2 < 0$, the results shown in Fig. 4.6 differ from the positive case. The first observed difference is that there are two regimes.

For $c_2 < -2/\pi$, as explained in 2.2.4, there appears a purely imaginary eigenfrequency that leads the system to a linear instability. For small values of ε, this exponentially growing mode leads the system to collapse before the BR instability can manifest. In this regime, the collapse time scales as $\log \varepsilon$, as illustrated in the right panel of Fig. 4.6, rather than following the characteristic ε^{-2} scaling of the BR instability.

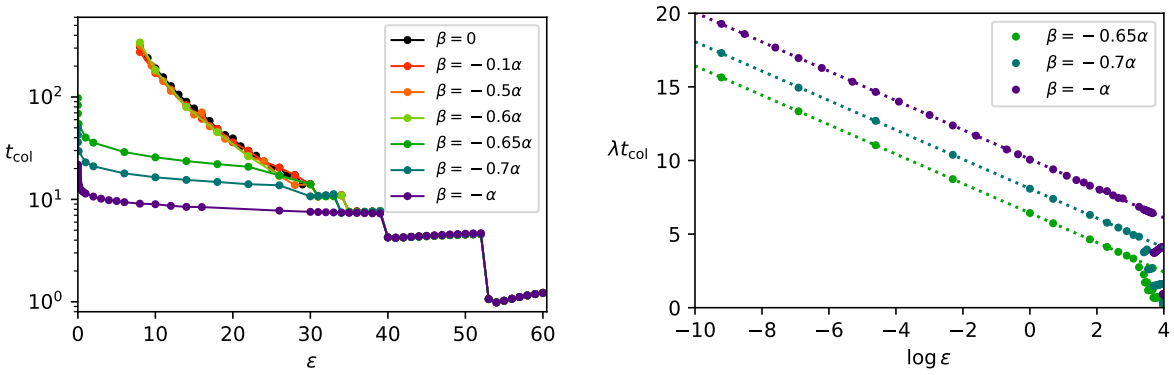

Figure 4.6: Left panel: Collapse time t_{col} as a function of the initial amplitude ε for various boundary conditions of the form $\beta = c_2\alpha$ (relevant deformations) with $c_2 < 0$, and for the case with $\beta = 0$ (no deformation). For $-\frac{2}{\pi} < c_2 < 0$, deviation from the non-linear instability behaviour of the undeformed case is barely observed. On the other hand, for $c_2 \leq -\frac{2}{\pi}$, the exponentially growing mode (2.79) dominates the system dynamics for sufficiently small ε, leading to a qualitatively different collapse time curve. Right panel: Demonstration that, for boundary conditions with $c_2 \leq -\frac{2}{\pi}$, $t_{\mathrm{col}}(\varepsilon) \sim -\log \varepsilon$ in the $\varepsilon \to 0$ limit.

For $-2/\pi < c_2 < 0$, no imaginary eigenfrequencies are present. Remarkably, the results displayed in the left panel of Fig. 4.6 suggest that these boundary conditions do not render the system non-linearly stable in the same way as positive c_2 deformations,[2] even though the eigenfrequency spectrum is only asymptotically resonant (see 2.2.4). It is worth noting here that the numerical construction of these curves is quite resource demanding, requiring a large number of global mesh refinements to keep the constraints satisfied and the numerical simulation convergent until the very last moments of the collapse (see Appendix C for technical details).

Although the collapse time curves do not clearly indicate that this is a different scenario from the BR instability, we can once again analyse the observable $\Pi^2(t, x = 0)$ to shed light on the situation. Fig. 4.7 shows the evolution of this quantity and the rescaled curve $\varepsilon^{-2}\Pi^2(\varepsilon^2 t, x = 0)$. The behaviour of this observable differs significantly from what is observed for non-relevant deformations (Figs. 4.2 and 4.4). These curves do not exhibit clearly marked phases of increasingly rapid growth, and the rescaled functions do not approach a universal curve as ε decreases. Accordingly, t_{col} does not follow a ε^{-2} scaling.[3]

This analysis suggests that negative relevant deformations will actually render the system non-linearly stable for sufficiently small amplitudes ε, below the values accessible by our simulations. In order to provide further evidence for this hypothesis, we have explored $\beta \propto \alpha$ boundary conditions with a larger value of the width, $\sigma = 0.3$. The collapse time curves illustrated in Fig. 4.8 show that for no deformation ($\beta = 0$) the BR-instability is still present. For

[2] Mention should be made here that simulations with $\varepsilon = 7$ (below the smallest amplitude shown in Fig. 4.6, $\varepsilon = 8$) have been performed, where the case with deformation seems to remain without collapsing slightly longer than the undeformed case (around $\Delta t \sim 100$ longer). Unfortunately, the maximum refinement of the code that we have managed to perform is not enough to observe the collapse. Although unreliable, this potential result would be in line with the rest of the evidence provided.

[3] We note that the results presented in Fig. 4.7 look qualitatively similar to the ones obtained in the flat space case discussed in Ref. [11] for a non-resonant spectrum (see Fig. 5 in the published version).

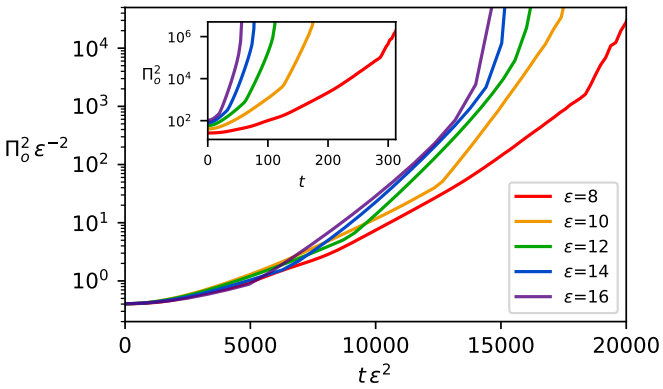

Figure 4.7: The inset shows the upper envelope of $\Pi(t, x = 0)^2$ for some evolutions with $\beta = -0.6\alpha$ boundary conditions (relevant deformations) and small amplitudes ε. The main plot shows the rescaled curves $\varepsilon^{-2}\Pi^2(\varepsilon^2 t, x = 0)$. In contrast to the non-relevant cases depicted in Figs. 4.2 and 4.4, there is no universal behaviour emerging when ε is reduced. This is incompatible with a BR instability being at work in this case.

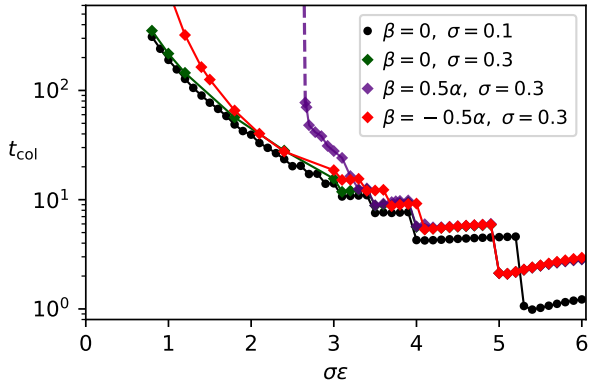

Figure 4.8: Collapse time t_{col} as a function of initial amplitude ε times initial width σ, for the undeformed cases with $\sigma = 0.1$ and 0.3, and two relevant deformations of opposite signs, $\beta = 0.5\alpha$ and $\beta = -0.5\alpha$, with $\sigma = 0.3$. Both undeformed cases follow the collapse time curve characteristic of the BR instability. In the deformed ones, however, the collapse time curves are clearly lifted.

$c_2 < 0$, however, despite the fact that the system is still non-linearly unstable in the range of ε we have been able to probe, the collapse time now deviates significantly from its undeformed counterpart as ε is reduced. This provides another reason to suspect that a similar deviation will also happen for $\sigma = 0.1$ at sufficiently small values of ε.

4.3.3. Interpreting the sign dependence

Leaving aside the question of whether the system is non-linearly stable or not in the $\varepsilon \to 0$ limit, the fact that at finite ε its behaviour is markedly different depending on the sign of c_2—as

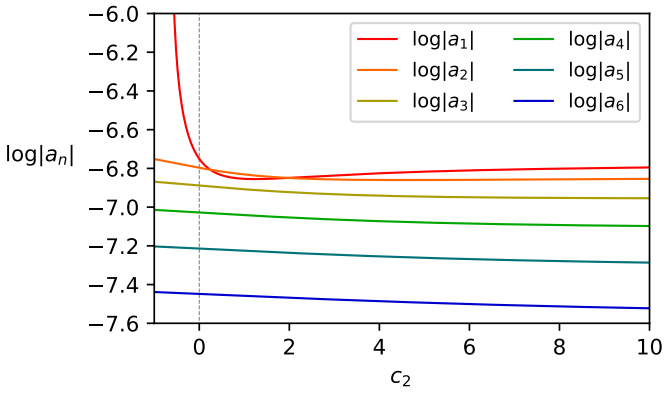

Figure 4.9: First six coefficients $a_1, \ldots, a_6$ of the spectral decomposition (4.7) for the Gaussian initial data (4.6) ($\varepsilon = 1$, $\sigma = 0.1$) as functions of the relevant coupling c_2.

can be seen from Fig. 4.8 and the top panels of Figs. 4.5 and 4.6—is a robust finding of our analysis meriting further study in the search for a definitive explanation.

We believe that the ultimate explanation of this difference will involve a detailed understanding of the interplay between the Gaussian initial data (4.6) and the space of exactly periodic solutions as the relevant coupling c_2 is varied. This is motivated by the following observation. Neglecting the backreaction of the scalar field, the spectral decomposition of $\phi(t, x)$ takes the form

$$\phi(t, x) = \sum_{n=1}^{\infty} a_n \sin(\omega_n t) e_n(x), \tag{4.7a}$$

$$e_n(x) = \frac{2 \sin(\omega_n x)}{\sqrt{\pi}\sqrt{1 - \operatorname{sinc}(\pi\omega_n) \tan x}}, \tag{4.7b}$$

where $\{\omega_n, n \in \mathbb{N}\}$ are the eigenfrequencies, roots of Eq. (2.75), and $\{e_n, n \in \mathbb{N}\}$ a complete set of orthonormal eigenfunctions. Note that, for fixed initial data, the a_n coefficients change as a function of c_2, since ω_n, and hence e_n, do. The lowest coefficients of the spectral decomposition of the Gaussian initial data (4.6) (with $\varepsilon = 1$ and $\sigma = 0.1$) are provided in Fig. 4.9. We observe that, while for $c_2 \in \left[-\frac{2}{\pi}, 0\right]$ and $c_2 \to \infty$ the spectral decomposition is dominated by the fundamental mode (with a strong dominance as $c_2 \to -\frac{2}{\pi}$), there is a window of positive couplings where the first excited mode dominates.[4] This suggests to us that, for a finite energy, at moderate positive values of c_2, the Gaussian initial data (4.6) can fall into the stability island sourced by a multi-oscillon analogous to the ones constructed in Ref. [23]. Thinking along these lines, the enhanced non-linear instability we have found for $c_2 < 0$ could simply be a consequence of the lack of any exactly periodic solution dominated by the fundamental mode for the range of energies we have explored.

If the Gaussian initial data are allowed to evolve, it is observed that the dominant modes in the spectrum are approximately those found between ω_2 and ω_5 (although the shape of the

[4] The equality between $|a_1|$ and $|a_2|$ is attained at $c_2 \approx 0.24$ and $c_2 \approx 1.97$, and the ratio $|a_1|/|a_2|$ only recovers its value in the alternative quantization at $c_2 \approx 5.46$.

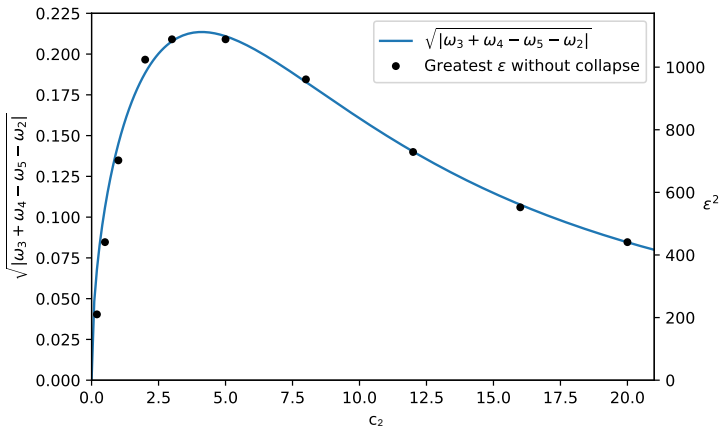

Figure 4.10: Deviation $\Delta\omega$ from a resonant spectrum as a function of c_2 for relevant deformations $\beta = c_2\alpha$ with positive values of c_2, and the highest amplitude of the initial data that avoids non-linear instability.

spectrum oscillates over time and is not always clearly defined). Considering the resonant channel described in Eq. (1.26), a measure of how those modes differ from a resonant spectrum can be defined as

$$\Delta\omega \equiv \sqrt{\omega_3 + \omega_4 - \omega_5 - \omega_2}. \tag{4.8}$$

In Fig. 4.10, we present $\Delta\omega$ as a function of c_2 for positive values of c_2 and compare it with the highest amplitude of the initial data that avoids non-linear instability. We observe an apparent correlation between the deviation of the dominant modes from a resonant structure and the maximum amplitude for which the initial data remain stable. This correlation could describe the behaviour of the collapse time curves in Fig. 4.5.

4.4. Comment on irrelevant deformations and AdS asymptotic symmetry breaking

The fact that only marginal deformations preserve the AdS asymptotic symmetries, as explained in 2.2.3.4, raises an intriguing question. On the one hand, irrelevant deformations do not preserve AdS asymptotic symmetries. On the other hand, according to the expansion in 2.68 used to obtain the linearized normal modes, irrelevant deformations $\beta = c_4\alpha^3$ correspond to subleading terms and do not break the resonant character of the eigenfrequency spectrum. This naturally leads to the question of whether this question has any implications for the non-linear stability of these deformations.

A deviation in the behaviour of the collapse time curves has been observed for a particularly large positive value of $c_4 = 100$, where simulations remain stable. In this regime, the arguments described in section 2.2.4 may no longer be valid due to the breakdown of the assumptions $c_n = O(1)$ and $\alpha = O(\gamma)$. This raises the question of whether, for smaller initial data amplitudes, the collapse times would once again approach those of the undeformed case as previous assumptions become valid again. In any case, the implications of the asymptotic symmetry breaking remain an open question.

4.5. Summary

In this final chapter, we have approached the AdS instability problem from a different perspective, employing mixed boundary conditions, which are dual to multi-trace deformations in the CFT. These boundary conditions allow us to explicitly break the resonant structure of the AdS spectrum from the beginning, providing an alternative approach to the conventional framework based on islands of stability.

We have tested the system under relevant, marginal, and irrelevant deformations. While the BR instability persists for marginal and irrelevant deformations, the results differ significantly in the case of relevant deformations. Interestingly, the outcome depends on the sign of the deformation. For positive relevant deformations, the system becomes non-linearly stable, and for sufficiently large positive deformations, the instability reappears as the boundary condition approaches the standard quantization.

For negative relevant deformations, two distinct regimes emerge. For $c_2 < -2/\pi$, an exponentially growing mode leads the system to collapse on a $\log(\varepsilon)$ timescale. Another regime for $-2/\pi < c_2 < 0$ presents a much smaller deviation from the undeformed case than the deviation observed for positive values of c_2.

Finally, we commented on an interesting aspect regarding the breaking of AdS asymptotic symmetries by irrelevant deformations, which do not alter the resonant structure of the linearized frequency spectrum. The implication of this symmetry breaking on non-linear stability remains an important open question for future study.

Chapter 5

Summary and conclussions

The studies presented in this thesis constitute a detailed exploration of scalar field dynamics in an anti-de Sitter (AdS) spacetime under time-periodic driving and mixed boundary conditions. This chapter summarizes the findings, offering a comprehensive analysis of the results and their implications for AdS dynamics, non-linear instabilities, and boundary-driven phenomena.

Resonance under periodic driving

Chapter 3 explored the response of a real, massless scalar field subjected to a time-periodic driving in AdS spacetime. The key results include:

- Resonant amplification and oscillons: Periodic driving at resonant frequencies leads to an interference pattern in the scalar field oscillations. Time-periodic solutions remain when the driving is switched off. We refer to these oscillating solutions without driving as *oscillons*. They are characterized by a spectrum of the form

$$\omega_{\rm osc}(2k+1) \ \text{ with } k \geq 0. \tag{5.1}$$

  The frequency and mass of the final oscillon depend on the amplitude reached by the driving, on the speed of the extraction, and also on the starting time of the extraction. The maximum possible mass decreases as long as the extraction becomes slower. In the limit $\beta \to \infty$ the system returns to the AdS vacuum, as occurs when the driving is introduced far from resonance.

- Chirped driving: Frequency modulation protocols have demonstrated that both upward and downward modulation can produce oscillons depending on the chirping rate. However, downward modulation is much more useful and easier to control, as the TPSs can approach the oscillon line at very small amplitudes without crossing it. Consequently, the solution can closely follow the oscillon curve and stop at a given frequency to generate an oscillon.

  Interestingly, even if the chirp does not cross any resonant frequency, still a higher harmonic can cross it, producing a linearized gas of oscillons, while the metric returns to AdS vacuum when the driving is switched off.

- Negative mass TPSs: Remarkably, for low driving frequencies of $\omega_{\mathrm{b}} \leq 1.25$, there exist TPSs with negative mass.
- Two-frequency driving: Driving with two frequencies revealed complex spectral behaviours, including solutions with a spectrum of the form

$$\omega_k = 2k + 1 \ \text{ with } k \geq 0 \tag{5.2}$$

  whose dominant frequency may vary over time. The solutions are compatible with the constructions proposed in [22]. Remarkably, certain protocols are able to produce a suppression of the energy cascade while the driving is on, with the cascade reactivating when the driving is switched off.
- Driving with noise: For a multi-mode driving simulating thermal noise, there seems to be a critical value for the parameter T, which plays the role of the temperature, that marks a threshold between collapsing and non-collapsing evolutions.

Non-linear instability with mixed boundary conditions

Chapter 4 addressed the effects of mixed boundary conditions on the non-linear instability originally identified by Bizoń and Rostworowski (BR instability). These boundary conditions are dual to multi-trace deformations of the Lagrangian of the dual CFT. The main findings include:

- Persistence of instability: For marginal and irrelevant deformations, the BR instability persists, with the collapse time scaling as ε^{-2} for small initial amplitudes. These deformations do not alter the resonant structure of AdS.
- Stability through relevant deformations: Relevant boundary deformations ($\beta = c_2\alpha$) break the resonance spectrum of AdS. Remarkably, the outcome differs significantly depending on the sign of the deformation. For $c_2 > 0$, the evolution becomes non-linearly stable. For very large deformations ($c_2 \gg 1$), the system returns to a non-linear instability regime, as the boundary condition approaches $\alpha = 0$, which corresponds to the standard quantization in the dual CFT.

  For $c_2 < 0$, there are two different regimes. When $c_2 < -2/\pi$, the fundamental mode becomes linearly unstable, and its exponential growth dominates the system dynamics in the $\varepsilon \to 0$ limit, overtaking the BR instability and leading to gravitational collapse on a time scale $\mathcal{O}(\log \varepsilon)$. In contrast, for $-2/\pi < c_2 < 0$, the collapse time curve hardly differs from the undeformed case. A more in-depth analysis of the scaling of Π^2 (related to the scalar curvature) with the amplitude of the initial data in this second regime reveals that the system does not behave as in the BR instability. The same analysis with a wider initial Gaussian does show a deviation of the collapse time curve with respect to the case without deformation, suggesting that for amplitudes lower than those reached in our simulations, a deviation in the collapse time curve would become evident also for the narrower Gaussian.

  We conjecture that the difference between the behaviour for positive and negative c_2 could be related to the interplay between the spectral decomposition of the initial Gaussian and the normal modes of the system, which depend on the value of c_2. For $c_2 < 0$, the

spectral decomposition of the Gaussian is strongly dominated by the fundamental mode. This suggests that, while for moderate positive values of c_2 the initial data could fall into the island of stability created by some multi-oscillon analogous to the ones constructed in Ref. [23], the non-linear instability for $c_2 < 0$ could be a consequence of the non-existence of oscillons dominated by the fundamental mode.

Both studies underscore the central role of resonance in AdS dynamics. Periodic driving at resonant frequencies can interfere with energy transfer across modes, while breaking the resonant character of the spectrum through relevant multi-trace deformations disrupts the energy cascade. These observations highlight resonance as a key mechanism driving energy cascades and potential instabilities.

Mixed boundary conditions introduce a broader perspective for stability analysis. Relevant deformations effectively break the exact resonance condition from the beginning. This mechanism aligns with the expectation that the resonant nature of the AdS spectrum is the primary driver of turbulence and collapse.

Open questions and future directions

- Refining numerical simulations: While most simulations demonstrated fourth-order convergence, those involving multiple frequencies in chapter 3 are particularly demanding. Simulations maintaining convergence for a longer time could detect the collapse and perhaps provide more insight into how these drivings can stop the energy cascade.
- Vanishing v.e.v. solutions: As argued in section 3.8, we expect that solutions with vanishing v.e.v. require a multiple-frequency driving. The numerical construction of these solutions remains an open challenge. Obtaining these solutions by the methods developed in Refs. [5, 24] requires dealing with non-normalizable modes.
- Difference between relevant deformations with opposite sign: The reason behind the contrasting behaviour for positive and negative values of c_2 in $\beta = c_2\alpha$ deformations remains a question to answer. Testing our hypothesis requires constructing multi-oscillons that would act as attractors to stabilize initial data with a moderate positive c_2 and fail to interact with data with a strong dominant fundamental mode.
- Irrelevant deformations and AdS asymptotic symmetry breaking: Further research would be necessary to understand the issue raised at the end of the chapter 4 regarding irrelevant deformations. On the one hand, these deformations do not preserve AdS asymptotic symmetries. On the other hand, they correspond to subleading terms in the linearized analysis that do not modify the resonant spectrum. Further investigation is required to understand whether this symmetry breaking has implications for nonlinear stability.

Aside from these specific models, dynamical AdS/CFT (with time-dependent boundary conditions) remains a promising area of exploration, offering rich opportunities to extend our knowledge of the correspondence.

Appendix A

Killing vectors of AdS_4

Anti-de Sitter (AdS) is a maximally symmetric spacetime that solves the vacuum Einstein equations with a negative cosmological constant. Therefore, it has the largest possible number of Killing vectors. In AdS_4, there are 10 Killing vectors, which, in the global AdS coordinate system (t, r, θ, ϕ) (Eq. (1.3)), take the following form:[1]

$$K_{51} = lF(r)\,\hat{n}_t, \tag{A.1a}$$

$$K_{21} = -r\sin\left(\frac{t}{l}\right)\sin\theta\cos\phi\,\hat{n}_t + lF(r)\cos\left(\frac{t}{l}\right)\sin\theta\cos\phi\,\hat{n}_r + \frac{l}{r}F(r)\cos\left(\frac{t}{l}\right)\left(\cos\theta\cos\phi\,\hat{n}_\theta - \csc\theta\sin\phi\,\hat{n}_\phi\right), \tag{A.1b}$$

$$K_{31} = -r\sin\left(\frac{t}{l}\right)\sin\theta\sin\phi\,\hat{n}_t + lF(r)\cos\left(\frac{t}{l}\right)\sin\theta\sin\phi\,\hat{n}_r + \frac{l}{r}F(r)\cos\left(\frac{t}{l}\right)\left(\cos\theta\sin\phi\,\hat{n}_\theta + \csc\theta\cos\phi\,\hat{n}_\phi\right), \tag{A.1c}$$

$$K_{41} = -r\sin\left(\frac{t}{l}\right)\cos\theta\,\hat{n}_t + lF(r)\cos\left(\frac{t}{l}\right)\cos\theta\,\hat{n}_r - \frac{l}{r}F(r)\cos\left(\frac{t}{l}\right)\sin\theta\,\hat{n}_\theta, \tag{A.1d}$$

$$K_{25} = r\cos\left(\frac{t}{l}\right)\sin\theta\cos\phi\,\hat{n}_t + lF(r)\sin\left(\frac{t}{l}\right)\sin\theta\cos\phi\,\hat{n}_r + \frac{l}{r}F(r)\sin\left(\frac{t}{l}\right)\left(\cos\theta\cos\phi\,\hat{n}_\theta - \csc\theta\sin\phi\,\hat{n}_\phi\right), \tag{A.1e}$$

$$K_{35} = r\cos\left(\frac{t}{l}\right)\sin\theta\sin\phi\,\hat{n}_t + lF(r)\sin\left(\frac{t}{l}\right)\sin\theta\sin\phi\,\hat{n}_r + \frac{l}{r}F(r)\sin\left(\frac{t}{l}\right)\left(\cos\theta\sin\phi\,\hat{n}_\theta + \csc\theta\cos\phi\,\hat{n}_\phi\right), \tag{A.1f}$$

[1] See, for example, Appendix A in [61].

$$K_{45} = r\cos\left(\frac{t}{l}\right)\cos\theta\,\hat{n}_t + lF(r)\sin\left(\frac{t}{l}\right)\cos\theta\,\hat{n}_r - \frac{l}{r}F(r)\sin\left(\frac{t}{l}\right)\sin\theta\,\hat{n}_\theta, \tag{A.1g}$$

$$K_{23} = \hat{n}_\phi, \tag{A.1h}$$

$$K_{34} = -\sin\phi\,\hat{n}_\theta - \cot\theta\cos\phi\,\hat{n}_\phi, \tag{A.1i}$$

$$K_{42} = \cos\phi\,\hat{n}_\theta - \cot\theta\sin\phi\,\hat{n}_\phi, \tag{A.1j}$$

where we have defined

$$F(r) = \sqrt{1+\left(\frac{r}{l}\right)^2}, \tag{A.2a}$$

$$\hat{n}_t = (F(r)^{-1},0,0,0), \tag{A.2b}$$

$$\hat{n}_r = (0,1,0,0), \tag{A.2c}$$

$$\hat{n}_\theta = (0,0,1,0), \tag{A.2d}$$

$$\hat{n}_\phi = (0,0,0,1). \tag{A.2e}$$

K_{51} is the Killing vector associated with time translations; K_{21}, K_{31} and K_{41} are associated with spatial translation; K_{25}, K_{35} and K_{45} are the generators of boost; while K_{23}, K_{34} and K_{42} are the generators of spatial rotations.

Appendix B

Equations of motion and multi-trace deformations

In this appendix, we explain the transformations needed in the equations of motion for the massless scalar field in section 4 to put them in a form suitable for numerical implementation. For a time-dependent spherically symmetric solution, we work with the ansatz (2.2). The equations of motion (2.4) with the potential (4.1) used in chapter 4 become

$$\delta' = -\frac{1}{4}\sin x \cos x(\Pi^2 + \Phi^2), \tag{B.1a}$$

$$f' = (\cot x + 3\tan x)(1-f) + 2\tan x \sinh\left(\frac{1}{2}\phi\right)^2 + f\delta', \tag{B.1b}$$

$$\dot{\Phi} = (fe^{-\delta}\Pi)', \tag{B.1c}$$

$$\dot{\Pi} = \cot^2 x(\tan^2 x f e^{-\delta}\Phi)' + 2e^{-\delta}\sec^2 x \sinh(\phi). \tag{B.1d}$$

To implement the boundary conditions corresponding to the multi-trace deformation, we start by redefining the fields ϕ and Φ in such a way that their leading-order behaviour close to the asymptotic boundary is isolated,

$$\phi(t,x) = \alpha(t)\cos x + \beta(\alpha(t))\cos^2 x + \tilde{\phi}(t,x)\cos^2 x, \tag{B.2a}$$

$$\Phi(t,x) = -\alpha(t)\sin x - 2\beta(\alpha(t))\sin x \cos x + \tilde{\Phi}(t,x)\cos x. \tag{B.2b}$$

The redefined fields $\tilde{\phi}$ and $\tilde{\Phi}$ satisfy the asymptotic boundary conditions

$$\tilde{\phi}\left(t,\frac{\pi}{2}\right) = 0, \quad \tilde{\Phi}\left(t,\frac{\pi}{2}\right) = 0, \tag{B.3}$$

which ensure that the original fields ϕ and Φ have the correct asymptotic falloff. The equation of motion for $\tilde{\Phi}$ is

$$\dot{\tilde{\Phi}} = \sec x((fe^{-\delta}\Pi)' - \sin x\,\dot{\alpha}) - 2\sin x\,\dot{\alpha}\frac{d\beta}{d\alpha}. \tag{B.4}$$

Note that, after the field redefinition, α becomes a dynamical variable which has to be evolved

in time in conjunction with Π and $\tilde{\Phi}$. The equation of motion for α follows from the relation

$$\dot{\alpha} = -\Pi'\left(t, \frac{\pi}{2}\right). \tag{B.5}$$

Taking stock, the final set of equations of motion we work with is given by

$$\delta' = -\frac{1}{4}\sin x \cos x(\Pi^2 + \Phi^2), \tag{B.6a}$$

$$f' = (\cot x + 3\tan x)(1-f) + 2\tan x \sinh\left(\frac{1}{2}\phi\right)^2 + f\delta', \tag{B.6b}$$

$$\dot{\tilde{\Phi}} = \sec x((fe^{-\delta}\Pi)' + \sin x\,\dot{\alpha}) + 2\sin x\,\dot{\alpha}\frac{d\beta}{d\alpha}, \tag{B.6c}$$

$$\dot{\Pi} = \cot^2 x(\tan^2 x f e^{-\delta}\Phi)' + 2e^{-\delta}\sec^2 x \sinh(\phi), \tag{B.6d}$$

$$\dot{\alpha} = -\Pi'\left(t, \frac{\pi}{2}\right). \tag{B.6e}$$

In the next section, we explain in detail how we solve this non-linear PDE system.

Appendix C

Numerical methods

Although the codes used in chapter 3 and chapter 4 are different due to the implementation of the boundary conditions, both codes share a similar scheme for evolution with a fourth-order Runge-Kutta algorithm. However, the code used for mixed boundary conditions is more challenging, requiring more subtle implementations. Therefore, in this appendix we explain the numerical details of the code used in chapter 4, and we refer to section C.4 for the differences that exist for the code used in chapter 3.

C.1. Integration strategy

We start by discussing the integration strategy we employed to solve Eqs. (B.6a)-(B.6e). The initial data consists of the values of $\tilde{\Phi}(t,x)$, $\Pi(t,x)$ and $\alpha(t)$ at a given time t; from these fields, we compute $\Phi(t,x)$ with Eq. (B.2b), from which $\phi(t,x)$ follows by a spatial integration. With the values of $\phi(t,x)$ and $\Pi(t,x)$ at our disposal, we solve the constraint equations (B.6a)-(B.6b) to find $f(t,x)$ and $\delta(t,x)$. We impose the gauge choice $\delta(t,\frac{\pi}{2})=0$, which identifies the time coordinate t with the time on the boundary field theory. Finally, $\tilde{\Phi}$, Π and α are evolved to time $t+\delta t$ with an explicit fourth-order Runge-Kutta algorithm. Note that the boundary condition $\beta=\beta_{BC}(\alpha)$ is applied implicitly both when obtaining $\Phi(t,x)$ and $\phi(t,x)$ through the redefinition (B.2b) and when using the evolution equation (B.6c) for $\tilde{\Phi}$. Collapse is detected when $f(t,x)$ vanishes for some value of x (or, more precisely, when it falls below a sufficiently small threshold).

C.2. Technical remarks

There are critical technical issues that need to be taken into account to obtain a convergent simulation code.

The first concerns artificial dissipation. Our code employs Kreiss-Oliger (KO) dissipation [74] to damp the numerical noise caused by non-propagating modes with wavelengths commensurate with the lattice spacing. The way the KO terms are added in the vicinity of the asymptotic

boundary critically affects code convergence. The strategy we followed to obtain a good convergence (see App. D) was to damp the KO terms by multiplying them with a linear ramp that goes to zero at the asymptotic boundary. Choosing the right spatial extent for the ramp is crucial: when the time evolution demands a global mesh refinement, one needs to keep intact the total number of grid points along which the KO dissipation is damped, rather than keeping the physical length of the ramp fixed—which would double the number of grid points modulated by the ramp at each refinement.

The second factor influencing the convergence of the simulation code is the method employed to compute $\Pi'\left(t, \frac{\pi}{2}\right)$ (which is needed to obtain $\dot{\alpha}$, cf. Eq. (B.6e)). In our implementation, we proceeded as follows. First, from the near-boundary expansion of the equations of motion, we have that (recall that $y = \frac{\pi}{2} - x$)

$$\Pi = \dot{\alpha} y + \dot{\beta} y^2 + O(y^3). \tag{C.1}$$

Second, the boundary condition $\beta = \beta_{BC}(\alpha)$ implies that

$$\dot{\beta}(\alpha) = \frac{d\beta(\alpha)}{d\alpha}\dot{\alpha}. \tag{C.2}$$

Combining both observations, we take the ansatz

$$\Pi(t, x) = \dot{\alpha} y + \frac{d\beta_{BC}(\alpha)}{d\alpha}\dot{\alpha} y^2 + a_3 y^3 + a_4 y^4, \tag{C.3}$$

demand that it agrees with the numerically determined values of Π at the grid points $y = n\delta x$ for $n = 1, 2, 3$ (where δx is the grid spacing), and solve for $\dot{\alpha}$, a_3 and a_4. In the end, we obtain our working expression for $\dot{\alpha}$,

$$\dot{\alpha} = -\Pi'(t, \pi/2) = \frac{4\Pi_{\frac{\pi}{2}-3\delta x} - 27\Pi_{\frac{\pi}{2}-2\delta x} + 108\Pi_{\frac{\pi}{2}-1\delta x}}{6\delta x\left(11 + 6\frac{d\beta}{d\alpha}\delta x\right)}. \tag{C.4}$$

Finally, we note that evaluating the right-hand sides of Eqs. (B.6c)-(B.6d) on the discretization grid might produce an indeterminate form $0/0$ leading to numerical instabilities. A useful method to deal with this situation is to apply L'Hôpital's rule, as noted in Ref. [75]. Given two functions $f(x)$ and $g(x)$ such that $f(x)/g(x) \to 0/0$ as $x \to x_0$, the key idea is not to evaluate f/g directly, but rather to replace it by the right-hand side of the identity

$$\frac{f}{g} = \frac{f'}{g'} - \frac{g}{g'}\left(\frac{f}{g}\right)'. \tag{C.5}$$

Contrary to the left-hand side, on the right-hand side the first term is well-behaved by construction, and, in the second one, the numerical instabilities induced by the small denominator inside the parenthesis are compensated by the small multiplicative factor in front.

We apply this procedure to evaluate the right-hand sides of the evolution equation of $\tilde{\Phi}$ (near the asymptotic boundary) and of $\tilde{\Pi}$ (both near the origin and near the asymptotic boundary); in the latter case, the method needs to be applied twice. A subtle point here is the way in which the quotient inside the parenthesis in Eq. (C.5) is regularized before taking the derivative. A

significant example of this issue arises when we apply this procedure to $\dot{\tilde{\Phi}}$. The first term on the right-hand side of Eq. (B.6c),

$$\sec x((fe^{-\delta}\Pi)' + \sin x\,\dot{\alpha}), \tag{C.6}$$

behaves as $0/0$ for $y \to 0$. This term corresponds to f/g in Eq. (C.5) and has to be regularized before taking the spatial derivative on the right-hand side of this expression. The value of (C.6) at the boundary could be obtained either as a spatial derivative of the field Π,

$$-\Pi''\left(t, x = \frac{\pi}{2}\right), \tag{C.7}$$

or be specified through α and β as

$$-2\frac{d\beta_{BC}(\alpha)}{d\alpha}\dot{\alpha}, \tag{C.8}$$

explicitly providing information about the multi-trace deformation. We have found that the latter option significantly improves the convergence of the code.

C.3. Error control

To assess the quality of the numerical simulations, we monitor the evolution of certain quantities which have to be zero in the continuum limit: the time derivative of the total mass and the integrated momentum constraint. We also qualitatively check that there is no tail of rapid oscillations following the travelling pulse of the scalar field, as this feature typically arises when the discretization near the asymptotic boundary is not optimal (for instance, by not implementing L'Hôpital's rule).

To keep the numerical simulation in check, we use the integrated momentum constraint to trigger a global mesh refinement when necessary. Simulations undergoing gravitational collapse at very late times with initially small amplitudes are particularly demanding. In these cases, we start with a resolution of $N = 2^{13} + 1$ physical grid points and need to go up to resolutions of $N = 2^{16} + 1$; in fact, the lowest initial amplitude for which we did observe gravitational collapse required a resolution of $N = 2^{18} + 1$.

C.4. Numerical details for the massless scalar field code

Obviously, the first difference with respect to the code explained in the previous paragraphs for a massive scalar field with mixed boundary conditions is that now the equations of motion are (2.4) with $V(\phi) = 0$. The variables evolved in time are only $\Phi(t, x)$ and $\Pi(t, x)$. We still compute $\phi(t, x)$, but since now there is no term $V(\phi)$ in the equations, this is not needed for evolution. When fixing the boundary values according to the driving, it is the time derivatives that are required.

This code also implements Kreiss-Oliger (KO) dissipation with a linear ramp modulation near the boundary. Although the extension of this ramp is important, since here we did not implement

any refinement during evolution, this is not such a crucial issue as in the other code. Since the equations of motion are simpler, it is not necessary to implement L'Hôpital's rule so many times.

As for error control, the same checks are performed, with the exception that mesh refinement is not implemented.

Appendix D

Convergence tests

We have checked the convergence of our simulation codes by evolving the same initial data and boundary conditions using three different grid spacings. Let $g_a(t,x)$ be a certain quantity obtained from the evolution on the grid with spacing $\delta x = \frac{\pi}{2a}$, and consider the norm

$$\|g_a - g_b\|_c \equiv \left(\int_0^{\pi/2} dx \, (g_a - g_b)^2 \right)^{1/2}, \tag{D.1}$$

where the sub-index c denotes that the integration is performed on a grid with $\frac{\pi}{2c}$ spacing. We take the convergence rate to be

$$2^{-q} = \frac{\|\Pi_{4n} - \Pi_{2n}\|_n + \left\|\tilde{\Phi}_{4n} - \tilde{\Phi}_{2n}\right\|_n}{\|\Pi_{2n} - \Pi_n\|_n + \left\|\tilde{\Phi}_{2n} - \tilde{\Phi}_n\right\|_n}, \tag{D.2}$$

where q is the convergence order.

Fig. D.1 shows the convergence order q for some of the simulations presented in chapter 3, while Fig. D.2 does the same for the results in chapter 4. It is natural to expect a convergence factor close to 4, although we could tolerate a slightly smaller value.

We have performed convergence tests for all numerical experiments reported in chapter 3 and for the most challenging evolutions in chapter 4. In Fig. D.1, the convergence factor exhibits a more pronounced initial transient due to the fact that starting with AdS vacuum makes both the numerator and the denominator in D.2 particularly small. Then, in general, the convergence factor indeed approaches 4 and even surpasses it in certain cases. This provides strong confidence in the numerical validity of our results.

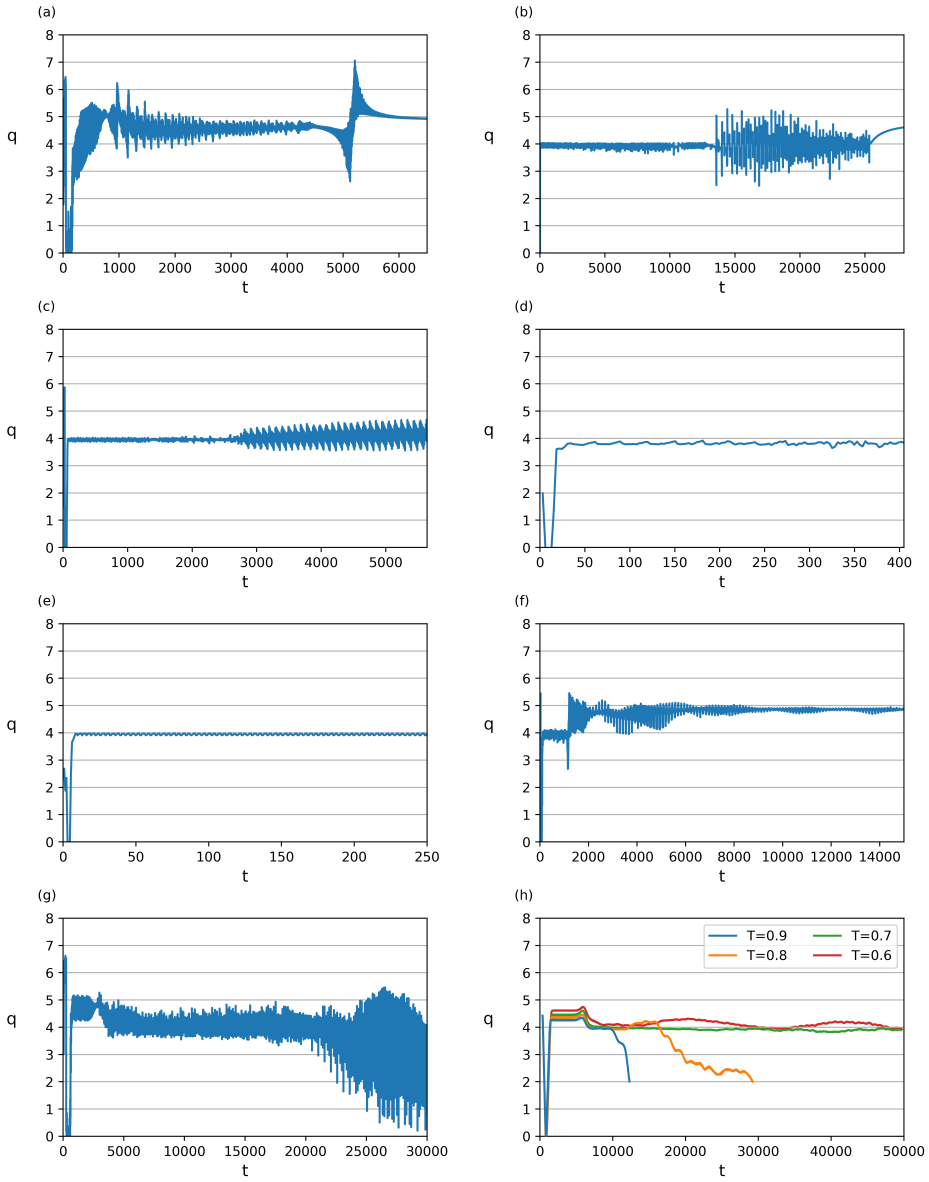

Figure D.1: Order of convergence α. (a) Fig. 3.2: driving at resonance $\omega_{\mathrm{b}} = 3$, (b) Fig. 3.5: down-chirping, (c) Fig. 3.7(a): chirping without crossing any resonance curve, (d) Fig. 3.8: zero v.e.v. solutions, (e) Fig. 3.9(b): energy-extracting solutions, (f) Fig. 3.12: chirping across two resonances, (g) Fig. 3.13: simultaneous $\omega_{\mathrm{b}} = 3$ and 5 drivings, (h) Fig. 3.14: multi-resonant mode driving.

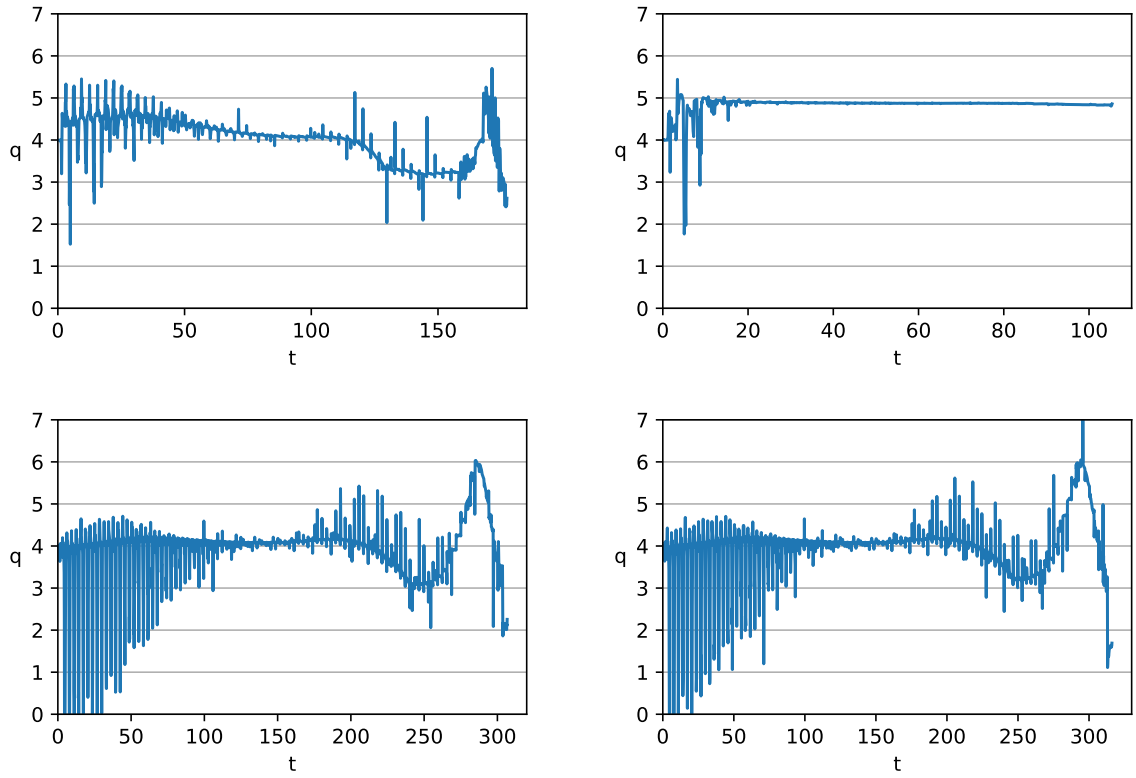

Figure D.2: Top left: Convergence order q for the evolution of initial data with $\varepsilon = 10$, $\sigma = 0.1$, and double-trace boundary conditions $\beta = -0.5\alpha$. Top right: Convergence order for initial data with $\varepsilon = 33.5$ and $\sigma = 0.1$, and boundary conditions $\beta = 5\alpha$. Bottom left: Convergence order for the evolution of initial data with $\varepsilon = 8$, $\sigma = 0.1$, and triple-trace (marginal) boundary conditions $\beta = 2\alpha^2$. Bottom right: Convergence order for the evolution of initial data with $\varepsilon = 8$, $\sigma = 0.1$, and irrelevant boundary conditions $\beta = 2\alpha^3$.

Bibliography

[1] J. Mas and D. Travieso Mayo, *Resonant drivings in global AdS*, *JHEP* **11** (2023) 230 [arXiv:2307.16884].

[2] A. Serantes, D. Travieso Mayo and J. Mas, *Multitrace deformations and the nonlinear stability of anti–de Sitter space*, *Phys. Rev. D* **111** (2025) 024044 [arXiv:2411.03297].

[3] J.M. Maldacena, *The Large N limit of superconformal field theories and supergravity*, *Adv. Theor. Math. Phys.* **2** (1998) 231 [arXiv:hep-th/9711200].

[4] P. Bizon and A. Rostworowski, *On weakly turbulent instability of anti-de Sitter space*, *Phys. Rev. Lett.* **107** (2011) 031102 [arXiv:1104.3702].

[5] M. Maliborski and A. Rostworowski, *Time-periodic solutions in an Einstein AdS–massless-scalar-field system*, *Phys. Rev. Lett.* **111** (2013) 051102 [arXiv:1303.3186].

[6] S.R. Green, A. Maillard, L. Lehner and S.L. Liebling, *Islands of stability and recurrence times in AdS*, *Phys. Rev. D* **92** (2015) 084001 [arXiv:1507.08261].

[7] A. Buchel, S.L. Liebling and L. Lehner, *Boson stars in AdS spacetime*, *Phys. Rev. D* **87** (2013) 123006 [arXiv:1304.4166].

[8] M. Maliborski and A. Rostworowski, *What drives AdS spacetime unstable?*, *Phys. Rev. D* **89** (2014) 124006 [arXiv:1403.5434].

[9] R. Arias, J. Mas and A. Serantes, *Stability of charged global AdS_4 spacetimes*, *JHEP* **09** (2016) 024 [arXiv:1606.00830].

[10] A. Biasi, P. Carracedo, J. Mas, D. Musso and A. Serantes, *Floquet scalar dynamics in global AdS*, *JHEP* **04** (2018) 137 [arXiv:1712.07637].

[11] M. Maliborski, *Instability of Flat Space Enclosed in a Cavity*, *Phys. Rev. Lett.* **109** (2012) 221101 [arXiv:1208.2934].

[12] J. Kurzweil and M. Maliborski, *Resonant dynamics and the instability of the box Minkowski model*, *Phys. Rev. D* **106** (2022) 124020 [arXiv:2209.05608].

[13] E. Witten, *Multitrace operators, boundary conditions, and AdS / CFT correspondence*, 2001, arXiv:hep-th/0112258.

[14] I. Papadimitriou, *Multi-Trace Deformations in AdS/CFT: Exploring the Vacuum Structure of the Deformed CFT*, *JHEP* **05** (2007) 075 [arXiv:hep-th/0703152].

[15] T. Hertog and G.T. Horowitz, *Towards a big crunch dual*, *JHEP* **07** (2004) 073 [arXiv:hep-th/0406134].

[16] T. Hertog and G.T. Horowitz, *Holographic description of AdS cosmologies*, *JHEP* **04** (2005) 005 [arXiv:hep-th/0503071].

[17] P. Basu, D. Das, S.R. Das and K. Sengupta, *Quantum Quench and Double Trace Couplings*, *JHEP* **12** (2013) 070 [arXiv:1308.4061].

[18] F.R. Ares, O. Henriksson, M. Hindmarsh, C. Hoyos and N. Jokela, *Effective actions and bubble nucleation from holography*, *Phys. Rev. D* **105** (2022) 066020 [arXiv:2109.13784].

[19] F.R. Ares, O. Henriksson, M. Hindmarsh, C. Hoyos and N. Jokela, *Gravitational Waves at Strong Coupling from an Effective Action*, *Phys. Rev. Lett.* **128** (2022) 131101 [arXiv:2110.14442].

[20] A. Caddeo, O. Henriksson, C. Hoyos and M. Sanchez-Garitaonandia, *Spinodal slowing down and scaling in a holographic model*, *JHEP* **08** (2024) 091 [arXiv:2406.15297].

[21] O. Aharony, O. Bergman, D.L. Jafferis and J. Maldacena, *N=6 superconformal Chern-Simons-matter theories, M2-branes and their gravity duals*, *JHEP* **10** (2008) 091 [arXiv:0806.1218].

[22] V. Balasubramanian, A. Buchel, S.R. Green, L. Lehner and S.L. Liebling, *Holographic Thermalization, Stability of Anti–de Sitter Space, and the Fermi-Pasta-Ulam Paradox*, *Phys. Rev. Lett.* **113** (2014) 071601 [arXiv:1403.6471].

[23] R. Masachs and B. Way, *New islands of stability with double-trace deformations*, *Phys. Rev. D* **100** (2019) 106017 [arXiv:1908.02296].

[24] M. Maliborski, *Dynamics of nonlinear waves on bounded domains*, Ph.D. thesis, Jagiellonian U., 2014. arXiv:1603.00935.

[25] A. Buchel, L. Lehner and S.L. Liebling, *Scalar Collapse in AdS*, *Phys. Rev. D* **86** (2012) 123011 [arXiv:1210.0890].

[26] A. Buchel, S.R. Green, L. Lehner and S.L. Liebling, *Conserved quantities and dual turbulent cascades in anti–de Sitter spacetime*, *Phys. Rev. D* **91** (2015) 064026 [arXiv:1412.4761].

[27] P. Bizoń, M. Maliborski and A. Rostworowski, *Resonant Dynamics and the Instability of Anti–de Sitter Spacetime*, *Phys. Rev. Lett.* **115** (2015) 081103 [arXiv:1506.03519].

[28] P. Carracedo, J. Mas, D. Musso and A. Serantes, *Adiabatic pumping solutions in global AdS*, *JHEP* **05** (2017) 141 [arXiv:1612.07701].

[29] M. Rangamani, M. Rozali and A. Wong, *Driven holographic CFTs*, *JHEP* **04** (2015) 093 [arXiv:1502.05726].

[30] R. Auzzi, S. Elitzur, S.B. Gudnason and E. Rabinovici, *On periodically driven AdS/CFT*, *JHEP* **11** (2013) 016 [arXiv:1308.2132].

[31] O.J.C. Dias, G.T. Horowitz, D. Marolf and J.E. Santos, *On the Nonlinear Stability of Asymptotically Anti-de Sitter Solutions*, *Class. Quant. Grav.* **29** (2012) 235019 [arXiv:1208.5772].

[32] P. Bizoń, D. Hunik-Kostyra and M. Maliborski, *AdS Robin solitons and their stability*, *Class. Quant. Grav.* **37** (2020) 105010 [arXiv:2001.03980].

[33] F. Ficek and M. Maliborski, *Dynamics of nonlinear scalar field with Robin boundary condition on the Schwarzschild–anti–de Sitter background*, *Phys. Rev. D* **109** (2024) 044015 [arXiv:2312.02760].

[34] S.K. Lam, A. Pitrou and S. Seibert, *Numba: a LLVM-based Python JIT compiler*, in *Proceedings of the Second Workshop on the LLVM Compiler Infrastructure in HPC* (2015) Article 7.

[35] Message Passing Interface Forum, *MPI: A Message-Passing Interface Standard*, Version 4.0, 2021. https://www.mpi-forum.org/docs/mpi-4.0/mpi40-report.pdf.

[36] NVIDIA, *CUDA Toolkit*, Version 11.5.0, 2021. https://docs.nvidia.com/cuda/.

[37] Wolfram Research, Inc., *Mathematica*. Champaign, IL. https://www.wolfram.com/mathematica.

[38] J.B. Griffiths and J. Podolsky, *Exact Space-Times in Einstein's General Relativity*, Cambridge Monographs on Mathematical Physics, Cambridge University Press, Cambridge (2009), 10.1017/CBO9780511635397.

[39] O. Aharony, S.S. Gubser, J.M. Maldacena, H. Ooguri and Y. Oz, *Large N field theories, string theory and gravity*, *Phys. Rept.* **323** (2000) 183 [arXiv:hep-th/9905111].

[40] A.V. Ramallo, *Introduction to the AdS/CFT correspondence*, *Springer Proc. Phys.* **161** (2015) 411 [arXiv:1310.4319].

[41] G. 't Hooft, *Dimensional reduction in quantum gravity*, *Conf. Proc. C* **930308** (1993) 284 [arXiv:gr-qc/9310026].

[42] L. Susskind, *The World as a hologram*, *J. Math. Phys.* **36** (1995) 6377 [arXiv:hep-th/9409089].

[43] G. 't Hooft, *A Planar Diagram Theory for Strong Interactions*, *Nucl. Phys. B* **72** (1974) 461.

[44] D. Christodoulou and S. Klainerman, *The global nonlinear stability of the minkowski space*, *Séminaire Équations aux dérivées partielles (Polytechnique)* (1989-1990) 1.

[45] H. Friedrich, *On the existence of n-geodesically complete or future complete solutions of Einstein's field equations with smooth asymptotic structure*, *Commun. Math. Phys.* **107** (1986) 587.

[46] B. Craps, O. Evnin and J. Vanhoof, *Renormalization group, secular term resummation and AdS (in)stability*, *JHEP* **10** (2014) 048 [arXiv:1407.6273].

[47] B. Craps, O. Evnin and J. Vanhoof, *Renormalization, averaging, conservation laws and AdS (in)stability*, *JHEP* **01** (2015) 108 [arXiv:1412.3249].

[48] V. Balasubramanian, P. Kraus and A.E. Lawrence, *Bulk versus boundary dynamics in anti-de Sitter space-time*, *Phys. Rev. D* **59** (1999) 046003 [arXiv:hep-th/9805171].

[49] I.R. Klebanov and E. Witten, *AdS / CFT correspondence and symmetry breaking*, *Nucl. Phys. B* **556** (1999) 89 [arXiv:hep-th/9905104].

[50] T. Hertog and K. Maeda, *Black holes with scalar hair and asymptotics in N = 8 supergravity*, *JHEP* **07** (2004) 051 [arXiv:hep-th/0404261].

[51] M. Henneaux, C. Martinez, R. Troncoso and J. Zanelli, *Asymptotically anti-de Sitter spacetimes and scalar fields with a logarithmic branch*, *Phys. Rev. D* **70** (2004) 044034 [arXiv:hep-th/0404236].

[52] C. Fefferman and C.R. Graham, *Conformal invariants*, in *Élie Cartan et les mathématiques d'aujourd'hui*, Astérisque, pp. 95–116 (1985).

[53] S. de Haro, S.N. Solodukhin and K. Skenderis, *Holographic reconstruction of space-time and renormalization in the AdS / CFT correspondence*, *Commun. Math. Phys.* **217** (2001) 595 [arXiv:hep-th/0002230].

[54] D. Poletti and C. Kollath, *Slow quench dynamics of periodically driven quantum gases*, *Phys. Rev. A* **84** (2011) 013615 [arXiv:1105.0686].

[55] C. Heinisch and M. Holthaus, *Adiabatic preparation of Floquet condensates*, *J. Mod. Opt.* **63** (2016) 1768 [arXiv:1605.08199].

[56] P. Weinberg, M. Bukov, L. D'Alessio, A. Polkovnikov, S. Vajna and M. Kolodrubetz, *Adiabatic perturbation theory and geometry of periodically-driven systems*, *Phys. Rep.* **688** (2017) 1 [arXiv:1606.02229].

[57] P. Breitenlohner and D.Z. Freedman, *Positive Energy in anti-De Sitter Backgrounds and Gauged Extended Supergravity*, *Phys. Lett. B* **115** (1982) 197.

[58] P. Breitenlohner and D.Z. Freedman, *Stability in Gauged Extended Supergravity*, *Annals Phys.* **144** (1982) 249.

[59] T. Hertog and G.T. Horowitz, *Designer gravity and field theory effective potentials*, *Phys. Rev. Lett.* **94** (2005) 221301 [arXiv:hep-th/0412169].

[60] T. Regge and C. Teitelboim, *Role of Surface Integrals in the Hamiltonian Formulation of General Relativity*, *Annals Phys.* **88** (1974) 286.

[61] M. Henneaux and C. Teitelboim, *Asymptotically anti-De Sitter Spaces*, *Commun. Math. Phys.* **98** (1985) 391.

[62] M. Henneaux, C. Martinez, R. Troncoso and J. Zanelli, *Asymptotic behavior and Hamiltonian analysis of anti-de Sitter gravity coupled to scalar fields*, *Annals Phys.* **322** (2007) 824 [arXiv:hep-th/0603185].

[63] B. Carter, *Hamilton-Jacobi and Schrodinger separable solutions of Einstein's equations*, *Commun. Math. Phys.* **10** (1968) 280.

[64] M. Cvetic, M.J. Duff, P. Hoxha, J.T. Liu, H. Lu, J.X. Lu et al., *Embedding AdS black holes in ten-dimensions and eleven-dimensions*, *Nucl. Phys. B* **558** (1999) 96 [arXiv:hep-th/9903214].

[65] M.S. Costa, L. Greenspan, J. Penedones and J.E. Santos, *Polarised Black Holes in ABJM*, *JHEP* **06** (2017) 024 [arXiv:1702.04353].

[66] F. Wilczek, *Quantum Time Crystals*, *Phys. Rev. Lett.* **109** (2012) 160401 [arXiv:1202.2539].

[67] T. Ishii, Y. Kaku and K. Murata, *Energy extraction from AdS black holes via superradiance*, *JHEP* **10** (2022) 024 [arXiv:2207.03123].

[68] M.W. Choptuik, J.E. Santos and B. Way, *Charting islands of stability with multioscillators in anti–de Sitter space*, *Phys. Rev. Lett.* **121** (2018) 021103 [arXiv:1803.02830].

[69] M. Choptuik, R. Masachs and B. Way, *Multioscillating boson stars*, *Phys. Rev. Lett.* **123** (2019) 131101 [arXiv:1904.02168].

[70] B. Cownden, *Examining instabilities due to driven scalars in AdS*, *JHEP* **12** (2020) 013 [arXiv:1912.07143].

[71] F.V. Dimitrakopoulos, B. Freivogel and J.F. Pedraza, *Fast and slow coherent cascades in anti-de Sitter spacetime*, *Class. Quant. Grav.* **35** (2018) 125008 [arXiv:1612.04758].

[72] A.A. Clerk, M.H. Devoret, S.M. Girvin, F. Marquardt and R.J. Schoelkopf, *Introduction to quantum noise, measurement, and amplification*, *Rev. Mod. Phys.* **82** (2010) 1155 [arXiv:0810.4729].

[73] A. Anabalon, D. Astefanesei, D. Choque and C. Martinez, *Trace Anomaly and Counterterms in Designer Gravity*, *JHEP* **03** (2016) 117 [arXiv:1511.08759].

[74] H.-O. Kreiss, *Methods for the approximate solution of time dependent problems*, (1973) .

[75] M. Maliborski and A. Rostworowski, *Lecture Notes on Turbulent Instability of Anti-de Sitter Spacetime*, *Int. J. Mod. Phys. A* **28** (2013) 1340020 [arXiv:1308.1235].

This thesis investigates the dynamics of Einstein gravity coupled to a scalar field in anti-de Sitter (AdS) spacetime, focusing on the implications of different time-dependent boundary conditions. In one model, a massless field is subjected to time-periodic boundary conditions, particularly in regions near resonant frequencies. A second model considers a scalar field with mass within the so-called dual quantization window, allowing for mixed boundary conditions that are dual to multi-trace deformations in the boundary CFT. The nonlinear stability of the system is then explored under relevant, marginal and irrelevant deformations.